

PRESSURE SENSING AND CONTROL OF AN AIRCRAFT PASSENGER SEAT

by

Gabriel H. Campos
Bachelor of Engineering, Ryerson University (2014)

A thesis

presented to Ryerson University

in partial fulfillment of the

requirements for the degree of

Master of Applied Science

in the Program of

Aerospace Engineering

Toronto, Ontario, Canada, 2017

©Gabriel H. Campos, 2017

Author's Declaration

I hereby declare that I am the sole author of this thesis. This is a true copy of the thesis, including any required final revisions, as accepted by my examiners.

I authorize Ryerson University to lend this thesis to other institutions or individuals for the purpose of scholarly research.

I further authorize Ryerson University to reproduce this thesis by photocopying or by other means, in total or in part, at the request of other institutions or individuals for the purpose of scholarly research. I understand that my thesis may be made electronically available to the public

Abstract

PRESSURE SENSING AND CONTROL OF AN AIRCRAFT PASSENGER SEAT

Gabriel H. Campos, B.Eng.
Master of Applied Science, 2017
Department of Aerospace Engineering
Ryerson University

The premise of this work is to address aircraft seat comfort. This thesis presents the development of an automatic morphing backrest used to reduce pressure experienced by the passenger from the seat. Uncomfortable, high surface pressure zones on the backrest can be alleviated by decentralizing the occupant's weight. The improved pressure distribution is intended to decrease discomfort during flight while taking different comfort/discomfort models into consideration.

Pressure distribution data from the embedded sensor mat is used to compute the seat's cushion deflection and corresponding backrest contour caused by the passenger's weight. The surfaces of interest - the passenger's back and the seat, are modelled and discretized. The discretized surface contact pressure is integrated into the hyperelastic contact model to determine the loading profile. From this, the current pressure distribution and the cushion's surface change are computed and used in the control system to create the corresponding actuation of the surface.

Acknowledgments

I would like to express my sincere gratitude to my thesis supervisor, Dr. Jeff Xi for the great opportunity to be part of his research team, continuous guidance and valuable support during my research. His patience, advice and encouragement made this work possible.

I would also like to thank my colleagues and friends that made this research an enjoyable and unforgettable experience. Mr. Jasper Liu, Dr. Yun Lin and Mr. Peter Bradley for sharing with me their technical expertise and valuable academic advice. Dr. Pedro Goldman for his unconditional and enthusiastic support during my graduate studies.

Last but not least, I would like to thank my family for their support, motivation and love during my academic life.

Gabriel H. Campos

December, 2016

Table of Contents

<i>Author's Declaration</i>	<i>ii</i>
<i>Abstract</i>	<i>iii</i>
<i>Acknowledgments</i>	<i>iv</i>
<i>List of Tables</i>	<i>viii</i>
<i>List of Figures</i>	<i>ix</i>
<i>Acronyms</i>	<i>xii</i>
<i>Nomenclature</i>	<i>xiii</i>
CHAPTER 1 Introduction	1
1.1 Overview.....	3
1.2 Problem Statement and Objective.....	5
1.3 Thesis Outline.....	6
CHAPTER 2 Literature Review	9
2.1 What is Comfort? - Current State of Seat Comfort Research.....	9
2.2 Methods for Body Pressure Sensing and Mapping.....	11
2.2.1 Body Pressure Sensing and Mapping.....	12
2.2.2 Existing Methods for Body Pressure Measurements.....	16
2.2.3 Alternative Quantitative Measurements of Sitting Discomfort.....	18
2.2.4 Methods for Calibration of Pressure Sensors.....	18
2.3 Methods for Material Contact Modeling and Simulation.....	23
2.4 Methods for Modeling and Measuring the Stiffness of Materials.....	26
2.5 Summary of the Literature Review.....	30
CHAPTER 3 Seat Modelling and Analysis	31
3.1 Seat and Sitting Models.....	32
3.1.1 Human-Seat Contact Model.....	43
3.1.2 Recline Angle and Recline Mechanism.....	45
3.1.3 Pressure Distribution Parameter.....	50
3.2 Seat Pressure Measuring.....	51
3.3 Mathematical Deformation and Deflection Models.....	54
3.3.1 Hyperelastic Modeling.....	54
CHAPTER 4 Seat Sensing Development	58

4.1	Design Approach.....	58
4.1.1	Requirements	58
4.2	Development of Surface Pressure Mat.....	60
4.2.1	Preconditioning and Normalization of the Sensor Mat	62
4.2.2	Calibration Procedure.....	67
4.2.3	Pressure Mat Board Setup.....	76
4.3	Development of Pneumatic Actuation System	78
4.3.1	Actuator Board Setup	80
CHAPTER 5	<i>Seat Control System.....</i>	83
5.1	Plant.....	84
5.1.1	Actuator (Air-Spring) Deflection.....	85
5.2	Feedback	86
5.2.1	Hyperelastic Curve Fitting	87
5.2.2	Set-Point	90
5.2.3	Control Method.....	91
CHAPTER 6	<i>Testing and Results.....</i>	94
6.1	Pressure Mat.....	95
6.2	Pneumatic Actuator.....	98
6.3	Performance	99
6.3.1	Safety Features	103
CHAPTER 7	<i>Conclusion.....</i>	105
7.1	Contributions	105
7.2	Future Work	106
Appendices.....	<i>.....</i>	108
A.	Software	108
B.	Calibration, Normalization and Sensor Response	112
1.	FSR sensor.....	112
2.	Absolute, Integrated Pressure Sensor (MPXZ6130A).....	114
C.	Mooney-Rivlin Hyperelastic Model	116
D.	Figures of Interest.....	117
E.	Overview of Surface Force/Pressure Sensing Theory.....	120
F.	Raw Data and Calculations.....	123

<i>Bibliography</i>	127
<i>Glossary</i>	132

List of Tables

Table 2-1: Hyperelastic and Elastic Constants of the Human Body and Cushion Material [39].	25
Table 3-1: Coefficients for backrest regions.	40
Table 3-2: Area percentage for the backrest regions.	43
Table 3-3: Distance of cg to joint calculated from anthropometric data.	48
Table 3-4: Weight force per body segment.	49
Table 4-1: FSR 402 Characteristics [26].	61
Table 4-2: Solid Static Calibration Coefficients.	70
Table 4-3: Hyperelastic Calibration Coefficients for PU Core.	74
Table 4-4: Hyperelastic Calibration Coefficients for PU Core and Ballistic Gel.	75
Table 4-5: Corresponding Calibration Curves, F_i , for Each Sensor.	76
Table 4-6: Sensor ID with their relative location in the pressure mat.	76
Table 4-7: Control Inputs/Outputs for Air-spring(s).	79
Table 5-1: Experimental Ogden Model Parameters.	90
Table 6-1: Seat prototypes comparison.	95
Table 6-2: Test Results.	103
Table A-0-1: Normalization Gains for $F_1=1.57$ [N].	112
Table A-0-2: Static Properties of the FlexiForce and FSR Sensors [36].	118
Table A-0-3: Total Backrest Area.	123
Table A-0-4: Percentage are per region in the backrest.	123
Table A-0-5: Mass of Body Segments for the American Male [45].	123
Table A-0-6: Weight force per body segment.	124
Table A-0-7: Compression Test Results.	124

List of Figures

Figure 1-1: The discomfort pyramid [2].	2
Figure 1-2: Sitting comfort and discomfort transition [3].	3
Figure 1-3: Ideal pressure distributions for backrest [5].	5
Figure 2-1: XSensor [®] system setup [23].	14
Figure 2-2: a) External input and trigger synch box setup [24], b) BPMS pressure mat [24]	14
Figure 2-3: FlexiForce [®] model HT201 sensor [59].	15
Figure 2-4: FSR [®] model 402 single zone [26].	16
Figure 2-5: Relation of back angle and subjective comfort (90° -120°) [18].	18
Figure 2-6: Diagram of epoxy resin dome covering the sensor's active area (Modified) [33].	20
Figure 2-7: Suggested electrical interface (force-to-voltage) for FSR with R _M values [26].	21
Figure 2-8: Static conductance per unit surface (dots) and fitted curve (line) vs pressure [35].	23
Figure 2-9: Foam deformation under axial compression at different compression % [42].	27
Figure 2-10: Typical strain deformation for PU foam [42].	28
Figure 3-1: a) Coordinate system on the cushion, b) Sensor Location.	33
Figure 3-2: Discretized seat surface.	35
Figure 3-3: Backrest divided into 4 regions.	39
Figure 3-4: Locations of FSR elements on the backrest PU core for ALAS configuration.	44
Figure 3-5: Neutral Body Posture[45].	46
Figure 3-6: Link diagram for the shear and force on the XZ plane.	47
Figure 4-1: Backrest regions for Ideal pressure dispersion ratio a) optimal b) actual.	59
Figure 4-2: FSR's voltage divider circuitry.	61
Figure 4-3: a) Normalization gains b) Normalization gains piecewise function (SensorID:33).	64
Figure 4-4: Normalization result on the mat under F=100g.	65
Figure 4-5: Deviation Percentage before (right) and after (left) normalization.	66
Figure 4-6: FSR mat percentage deviation after normalization.	66
Figure 4-7: FSR output - Force vs Resistance for sample Sensor.	67
Figure 4-9: FSR output - Force vs Conductance for sample sensor.	69
Figure 4-8: Set-up used to apply a load to the FSR for solid calibration.	69
Figure 4-10: Hyperelastic calibration apparatus.	70
Figure 4-11: Hyperelastic calibration setup.	71

Figure 4-12: FSR output - Force vs Conductance for sample sensor.....	73
Figure 4-13: FSR output - Force vs Conductance for sample sensor with ballistic gel.....	74
Figure 4-14: Pressure mat diagram for a single section containing 9 FSR elements.....	77
Figure 4-15: Serial analog multiplexing connection block.	78
Figure 4-16: Sensor and actuator positions on the seat's cushion.	79
Figure 4-17: Hardware communication flowchart.....	80
Figure 4-18: Air Pressure Regulation Circuitry for Lumbar Air Spring.....	81
Figure 4-19: Air-Spring Valve System. a) Backside b) Top side, c) Pneumatic Sensor.	82
Figure 5-1: Graphic User Interface.	84
Figure 5-2: Location of the air-springs on the PU foam core.....	86
Figure 5-3: ALAS set-point algorithm.	87
Figure 5-4: PU foam stress-strain compression test.....	88
Figure 5-5: PU foam-ballistic gel stress-strain compression test.....	89
Figure 5-6: Seat system.....	90
Figure 5-8: Simplified control system overview.	91
Figure 5-9: Control points on a spline section.	92
Figure 5-10: Simulink control system method (real plant).....	93
Figure 6-1: Experimental setup of seat prototypes.....	94
Figure 6-2: Front schematic of morphing seat.	95
Figure 6-3: Pressure distribution from Synchrotilt a) Upright position b) Reclined position.	96
Figure 6-4: Pressure distribution from Synchrotilt a) upright position b) reclined position.	97
Figure 6-5: Visualisation of the actual pressure distribution superposed on a passenger animation.	98
Figure 6-6: Response of air-spring during pressurization.	99
Figure 6-7: Bombardier's Global 5000 seat.....	100
Figure 6-8: Load control points on the seat.....	101
Figure 6-9: ALAS Experimental Results a) Before a) After Lumbar Support.....	102
Figure A-0-1: Static calibration for sensor ID 0R.....	113
Figure A-0-2: MPXHZ6130A sensor A)Top view, B)Cross-section view C) Signal output [60]... ..	114
Figure A-0-3: AAP sensor decoupling circuitry.	115
Figure A-0-4: Tekscan® (BPMS) Body Pressure Measurement System [61].	117
Figure A-0-5: Step responses of the Nano17, FSR, and FlexiForce sensors. [36].	117
Figure A-0-6: FSR sensor output response for different R_M values [26].	117

Figure A-0-7: Pressure mat and hardware.....	118
Figure A-0-8: Early version of the GUI.....	119
Figure A-0-9: Schematic of capacitive sensor [23].....	120
Figure A-0-10: FSR® Construction by Interlink Electronics [26].....	121
Figure A-0-11: Response characteristic of FSR® [26].	122
Figure A-0-12: Body segments [45].....	124

Acronyms

Acronym	Definition
%BRP	Percentage Backrest pressure per region
ALAS	Automatic Lumbar Adjustment System
BDR%	Backrest Distribution Percentage
BFSL	Best Fit Straight Line
BPMS	Body Pressure Measurement System
EMG	Electromyography
FEM	Finite Element Method
FFT	Fourier Transform (Analysis)
FSR	Force Sensitive Resistor
ICP	Internal control points
MIMO	Multiple-Input and Multiple-Output
NIRS	Near-infrared Spectroscopy
PBR	Percentage per Body Region
PCB	Printed Circuit Board
PU	Polyurethane
QORS	Quadratic Optimal Regulator System
SCA	Surface Contact Area
SPD%	Seat Pan Distribution Percentage
SSL	Standard Sea Level (Conditions)
VAS	Visual Analogue Scale

Nomenclature

Symbol	Definition
(a, b)	Saturation coefficients for FSR sensor
(a, b, c)	Semi-axis lengths of the approximated shape of the air-spring
(a _i , b _i)	Hyperelastic coefficients
(α , μ)	Hyperelastic material parameters for Ogden's model
\widetilde{F}_M	3D discretized force distribution
\widetilde{P}_M	3D discretized pressure distribution
A	Cross-sectional area
A _a	Active area of sensor element
A _b	Total backrest area
A _c	Surface contact area
A _e	Sensor Area
e _a	Number of active FSR element sensors
e _i	Position of FSR sensor element on the i th row
e _{i,j}	Position of FSR sensor element on the i th row and j th column
e _{i,j,k}	Position of FSR sensor element on the i th row and j th column and k th
F	3D applied load
F _{ft}	Horizontal force on the ischial tuberosities
F _h	Hyperelastic calibration curve
F _{hf}	Horizontal force on the feet
f _{ij}	Point load applied at point x _{ij} (more precisely at sensor e _{i,j})
F _M	Force mat output
F _{max}	Maximum load for FSR sensor
F _{n,cr}	Normal force on the crista iliaca
F _{n,th}	Normal force on the thorax
F _{vf}	Vertical force on the feet
F _{vt}	Vertical force on the ischial tuberosities
G	Electrical conductance of the FSR sensor (1/ Ω)
G _s	Saturation of the FSR sensor due to pressure loading
H	Hysteresis effect of the FSR sensor

h_b	Human tissue analogue height
h_e	Vertical distance between adjacent sensors (from element's centre)
i	Sensor row in the mat
j	Sensor column in the mat
k_c	Cushion's (backrest) stiffness
k_s	Air-spring's stiffness
l_e	Horizontal distance between adjacent sensors (from element's centre)
m	Mass of the gas (kg)
M	Molecular weight of the gas (g/mol)
n	Control points
$N_{i,j}$	Normalization gain for sensor $e_{i,j}$
P	3D pressure distribution on the backrest
p	Absolute pressure of the gas (Pa)
P_a	Actuated surface pressure on the lumbar support
P_b	Surface pressure of the backrest
p_c	Cabin pressure
p_i	Ideal pressure
p_j	2D pressure distribution on the XZ plane
P_M	Pressure mat output
p_s	Internal gas pressure of the air-spring
p_k	P control gain
r	Number of sample points for the normalization
R_e	Resistance of the FSR sensor $e_{i,j}$
R_M	Measuring resistance ($k\Omega$)
S	3D surface curvature of the seat's backrest
$s(x,y)$	Surface (foam) height at point (x,y)
S^0	Ground state of the foam core
s_j	2D cross-section curvature of the seat's backrest on the XZ plane
T	Gas temperature (K)
t_s	Membrane thickness of the air-spring
V_{ext}	External Voltage
V_s	Volume of the air-spring

V^+	Voltage input (microcontroller)
α	Angle between the feet and the ground
β	Seat pan recline angle
γ	Recline angle of the pelvis
δ	Backrest Recline angle
Δz_s	Deflection of the air-spring
λ_i	Principal stretches
ν	Poisson's ratio
ρ	Density
ρ_s	Sensor density of the mat
χ	Point (on the j column) on the YX plane
Ψ	Strain-energy function
q_i	i^{th} coefficient of the backrest region

CHAPTER 1 Introduction

Air travel presents challenges that directly affect the comfort of the passengers. Boarding an airplane is not a pleasurable experience for most. The passenger has to arrive with sufficient time to check in, clear security, find the proper gate and at the end the passenger is confined in a small space for the entire duration of the flight. Once in the seat, the passenger's environment combined with the previous experience of boarding influence their perceived level of comfort. Leg room in particular is not always sufficient for most passengers. There are limited adjustments to the seat and reclining the seat is highly limited. All these space restrictions have been more prominent as airlines try to stay competitive in the commercial transportation industry. Therefore, it is not unusual for most passengers to encounter a form of discomfort at one point or another during their air-travel experience. This should be somehow an obvious realization since air travel has progressively become a popular choice of travel and thus comfort has been slowly being exchanged for competitive fare prices. In spite of that, innovations in aircraft design and comfort research have increased the overall level of passenger satisfaction in the last decades.

As discussed in [1] and [2], the role of comfort in airline tickets sales follows a clear pattern. For frequent flyer programs, comfort, service and airline's reputation are the prevalent factors that increase passenger revenue. For short distance flights, on-time service is more relevant than comfort but for long-haul flights, comfort becomes a priority. Thus, additionally to the academic incentive to better understand the phenomena of human comfort and discomfort, there is as well an economic incentive to study and improve passenger comfort. The main focus of aircraft cabin comfort research as of 2016 has been in the areas of sound/noise, air quality, and thermal comfort. Limited research

has been done on the sitting comfort of passengers. The lack of research in sitting comfort is an additional motivation for this thesis. Vink and Brauer [2], suggest that a possible reason for the lack of research in this area is that most of this research is conducted by the manufacturers and they are reluctant to share this knowledge. Also, sitting comfort is considered as the least influencing aspect in comfort. As seen in Figure 1-1, smell, light and noise are the dominant factors that affect the comfort state of the passenger. Only if all these dominant aspects of the pyramid are satisfied, sitting comfort will play a role in comfort.

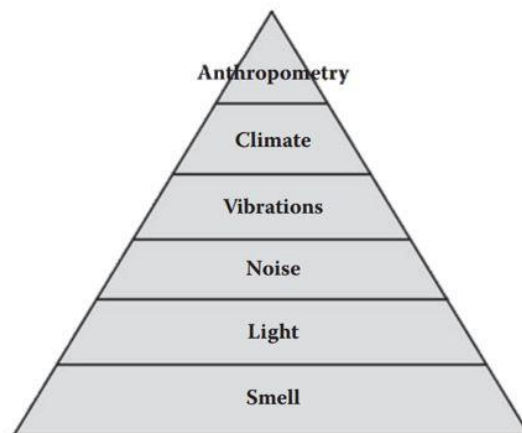


Figure 1-1: The discomfort pyramid [2].

Nonetheless, sitting comfort is an interesting area of research that requires further study. As such, the research in this work will focus on the area of sitting comfort. Specially in the effectiveness of backrest support and its influence on comfort. This topic was chosen since improper lumbar support has been the most reported aspect of discomfort directly related to seat design in aircraft travel [2]. Additionally, given the fact that aircraft passengers spend the majority of the time sitting and that the main interface between the aircraft and the passenger is the seat, it is important to have a good understanding of sitting comfort. This knowledge is essential to increase passenger satisfaction during air-travel.

1.1 Overview

In order to increase passenger comfort, it is important to first have a clear definition of comfort and discomfort. Even though there is some debate in the literature about the exact scientific definition of comfort and discomfort, the most agreed upon definitions will be used in this work. These definitions were developed based on subjective and objective reports from different researchers and were first used in [3] and they are as follows: Comfort is related to luxury, aesthetics, feeling refreshed, and is highly influenced by expectations, pre-flight and previous flight experiences. Conversely, discomfort deals with muscular fatigue factors, pressure points on the body and stiffness. Fundamentally, comfort and discomfort are separate entities, and unlike common believe, they are not opposites of each other. Moreover, comfort is not necessary present in the absence of discomfort. A visual representation of this concept can be observed in Figure 1-2.

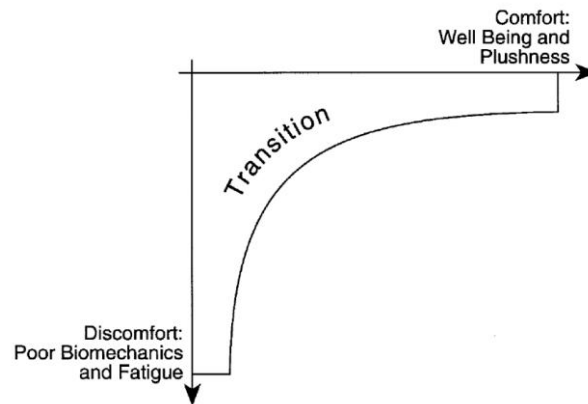


Figure 1-2: Sitting comfort and discomfort transition [3].

Comfort has been studied significantly more than discomfort. Particularly, the subjective aspects of air-travel comfort has been explored to a good degree such as in [4]. In that study, the subjective aspects in relation to aircraft interior comfort experience were gathered via questionnaires and interviews, during and after the flight experience. The data gathering process, analysis and results of the subjective method(s) are time consuming, often unreliable and impractical to apply to an active comfort seat design. Thus, this thesis focuses on the methods needed to reduce discomfort rather

than to create comfort. Psychological and subjective aspect (i.e. passengers' perception) of comfort will not be used to determine discomfort. This is because unlike comfort, discomfort can be objectively measured (i.e. via pressure readings, oxygen level in muscles, muscle activity, movement etc.) and it is related to biomechanical, ergonomic and physiological factors across all healthy individuals. These factors include joint angles, tissue pressure, muscle contractions, blood pooling and circulation blockage [3].

The effectiveness of lumbar support in a seat's backrest can be diminished by dimensional mismatch between the user and the seat design. The traditional approach to designing a "comfortable" seat is to use anthropometry data along with surface scanning of the whole-body with the purpose of improving the "*static*" seat design, such as in [5], [6] and [7]. However, efforts to parametrize the human body contour have been unsuccessful in developing new methodologies that can implement such anthropometry data in static designs of seats in a manner that can accommodate the majority of the passengers [8]. This can alternatively be accomplished by designing a morphing seat contour that aims to adapt to the human body automatically, by constantly taking into consideration anthropometry, seating position and loading profile of the passenger's weight. The investigation presented here focuses only on the lumbar morphing part of the seat. This concept can be expanded to the rest of the body as discussed in §4.1.1. The theory of pressure distribution and anthropometric data is used in this research to develop such automatic adjustment system.

For the development of the automatic lumbar adjustment support (ALAS) system, a reference value set to determine discomfort (the set-point), an input from the seat and an actuation mechanism must be developed in order to provide a better backrest support and thus a "comfortable" (less uncomfortable) sitting position. From the theory of the ideal pressure distribution, reference values will be extracted and used as the discomfort reference set. Surface pressure sensing between the human

body and the seat's surface is by far the most common and most reliable objective measurement for determine passengers discomfort. Thus, pressure reading will be used as the main input. As proposed in [9], the ideal sitting load percentage distribution per region in the human body (referred in this work as the ideal pressure distribution) should be as shown in Figure 1-3. Additionally, surface pressure sensing is a non-invasive procedure that can be easily used to test large population samples due to its convenience and good repeatability (after calibration). This seating comfort/discomfort method has been tested in several studies such as in [10], [11] and [12]. Lastly, the actuation mechanism will come from two air-springs that deform depending on their internal air pressure. Their gauge air pressure is monitored and used as an extra input for the system.

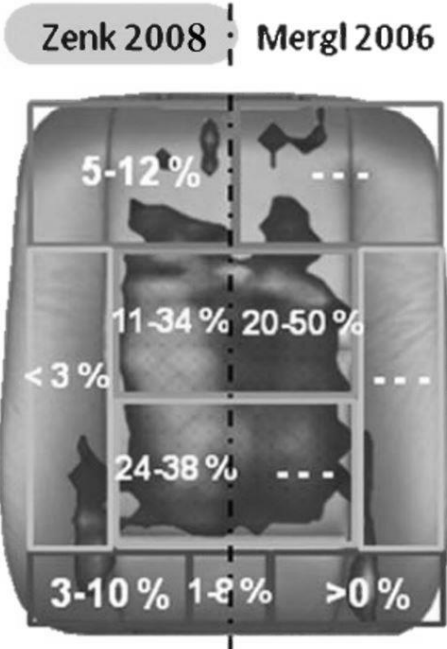


Figure 1-3: Ideal pressure distributions for backrest [5].

1.2 Problem Statement and Objective

Many factors influence the design of aircraft seats which in turn directly affect their comfort rating. These factors are design requirements such as light weight (limiting the amount of structural design), thin design (thus reducing the amount of cushioning), and mandatory safety aviation regulations [2]. The objective of this thesis is to develop an automatic lumbar adjustment support

(ALAS) system for an passenger aircraft seat. The automatic adjustment is intended to decrease passenger discomfort due to centralized loading on the backrest. The decentralization of the load can be achieved by increasing the contact area between the passenger and the seat via surface morphing. However, as will be discussed in CHAPTER 2, the change in the contact area must result in the ideal pressure distribution. The pressure distribution will be evaluated as well as the concept of Seat Pressure Distribution Percentage (SPD%) adapted to the backrest (BRD%). Ultimately, the pressure distribution will be the sole measurement to evaluate discomfort.

This investigation explores the mechanical properties and interactions of materials used to manufacture aircraft seats when in contact with the human body, in particularly, the resultant pressure distribution between these two surfaces. The purpose of this thesis is to expand on the theoretical knowledge of the ideal pressure distribution, previously proposed by Mergl [13], Zenk [12] and Hartung [10]. The theoretical knowledge of the ideal pressure distribution has been limited to be used only in the seat design itself. This is particularly true in the design aspects such as seat contour and material selection based on optimization methods.

However, a practical application of this knowledge has not been applied on real time for morphing the shape of the seat to approach the discomfort problem. The pressure distribution resulting from this interaction and from biomechanical models will be investigated. The theoretical basis of these elements and their respective relevance to this research are further discussed in CHAPTER 2 of this thesis.

1.3 Thesis Outline

This section provides a general outline for the organization of this thesis and the contribution of each chapter to this research. The design process consists of five phases:

- 1) Literature research.
- 2) Seat and contact model development.
- 3) Sensor development and integration.
- 4) Control method.
- 5) Experiments and performance evaluation.

This thesis begins with a literature review in CHAPTER 2. This chapter covers the current state of research of seat comfort/discomfort theory and discusses the methods of body pressure sensing and mapping. The two prominent sensor technologies for this application are reviewed with emphasis on thin surface pressure sensor. This is followed by a survey of the existing and commercial methods for body pressure sensing and mapping. Additionally, the methods for sensor calibration are explored and discussed. Finally, the last two sections cover the methods for material and contact modeling needed for the analysis in §3.3.

In CHAPTER 3, the seat's morphing surface model is introduced. The morphing model aims to achieve the ideal pressure distribution by changing the curvature of the seat. This chapter lays down the fundamentals for the necessary derivations for the surface adaptability to decentralized the load from the human body. Surface deflection and the factors that influence the pressure distribution on the seat's surface are also presented in this chapter.

CHAPTER 4 presents the design approach and requirements needed to develop the ALAS system. Each of the basic components of the system are discussed with particular emphasis on the calibration of the surface pressure sensors. The electronic component design is also discussed. Location and density of the sensors of the pressure mat are discussed along with their relevance for the estimation of the contact area.

CHAPTER 5 defines the closed-loop feedback and control method needed to attain the ideal pressure distribution via air-spring actuation. The inputs and their relevance to the control system such as the pressure mat and gauge pressure from the air-spring are stated. In the next section, the control algorithm is discussed. The chapter ends with an explanation of how the system integrates with software to run the control algorithm in the seat hardware and how this model can be expanded to control other surfaces of the seat.

CHAPTER 6 shows the experimental setups constructed to test the theory in this thesis. The results of the testing and experiments are compared and discussed in the section. The final performance of the system will be discussed and a summary of the findings will be provided.

Lastly, CHAPTER 7 concludes this thesis. The contributions and their relevance to the field are highlighted. The methods for improvement and future work are discussed in the last section for future research.

CHAPTER 2 Literature Review

A literature review was conducted to gain a good understanding of the current state of research for seat design, comfort/discomfort models and theories. The relationship between human characteristics and associated interface pressure with a seat are researched along with the tools required to measure such interactions. The corresponding methods and concepts needed for the development of such aircraft seat with ALAS are explored. The existing methods for these systems were researched and thoroughly analyzed and the findings are summarized in this chapter. The scope of this literature review is limited to a total of 43 scholarly articles and other professional and academic works relevant to this topic that met the following criteria:

- 1) Articles published in or after 1990 (except for Ogden's early work on hyperelastic materials, 1973, due to its academic relevance in this field).
- 2) Articles related to comfort/discomfort research for healthy subjects and with no known existing medical conditions.

2.1 What is Comfort? - Current State of Seat Comfort Research

Research conducted by Zhang et al. [14] suggests that comfort in (automobile) seat designs is subjective and highly influenced by aesthetic bias, whereas discomfort tends to be objective and in response to biomechanical and physiological responses. This highlights the need for the research and develop of a method to quantify the biomechanical and physiological response of the subjects. Vink's and Brauer's research [2] emphasises the difference between comfort and discomfort in aircraft passengers during both short and long term seating. The authors argue that passengers experience discomfort due to the pressure distribution and stiffness of the seat, rather than experiencing comfort. This is an important remark since this provides a guideline that can be used to approach the problem

of passenger sitting well-being. The concept that discomfort should be eliminated rather than to create comfort allow us to propose a quantitative measurement for the development of our model. Discomfort should be the main factor analyzed in order to design the seat rather than comfort. Discomfort measurements can be obtained from measured data via pressure sensors and cushion stiffness measurements.

Research in the area of comfort/discomfort has been used in recent decades to approach the seat design problem from an objective perspective. Most of the current research focuses on load distribution on the contact surface between the seat and the passenger as well as the resultant stress inside the human tissue(s). Models for discomfort in static seat designs have been explored and tested mostly for the automotive industry; yet little research has been conducted on *dynamic* seat designs. For most of the static designs, the approach seems to be similar between the industry and academia. The design is based on pressure readings, ergonomics, anthropometry, etc., of a sample population along with subjective reports from the participants of the study. Then the final design and material are selected, in hopes that they will fit the entire population (or at least a large portion of the population). This methodology is associated with high cost and long development time.

For static seat designs once the design has been selected, a change in the seat's geometry and/or stiffness is often not possible. Recently, stiffness/geometry changes to the seat's surface have been introduced via pneumatic lifting elements (air-springs) along with previous seat settings (recline angle, height, etc.) [15]. These manual adjustments tend to overcomplicate the operation of the seat leading to a paradox – with too many manual adjustments the discomfort level cannot be improved. As the number of seat adjustments increases in a given design, the possible combinations of settings increases in a factorial manner. For example, the automotive multifunction seat of a BMW760i (model 2006) is very difficult to operate manually. The seat is comprised of 20 individually adjustable

parameters. Due to the combinational results of the adjustments, the seat can have up to 200 million possible settings. This issue was first explored in an early work of Zenk (2008) and later improved [12], where the problem of determining an optimal comfortable setting for a given driver was introduced. This research was followed with medical validation via *in vivo* intervertebral disc pressure measurements of the ideal pressure distribution introduced by Mergl [13]. Additionally, a control algorithm for the optimal settings was developed to reduce the complexity of finding the appropriate settings manually. These and other similar seat comfort models accompanied with human tissue models such as in [16] and [17] have been used to generate computer simulations of the expected discomfort level of seat designs. These models eliminate the need of subject testing thus, accelerating the development of seat designs.

For the purpose mentioned above, and in order for the ideal pressure distribution to have a practical application, the need to measure the surface pressure distribution between the passenger and the seat arises. This pressure distribution can be used as an objective parameter to determine discomfort and used as a feedback signal for a dynamics seat model. This will be introduced in CHAPTER 5 with the ideal pressure distribution as a reference parameter.

2.2 Methods for Body Pressure Sensing and Mapping

The seating design process has been a focus of study from both the industry and literature in order to better understand discomfort from a scientific approach. Previous research methods have been focused on understanding discomfort from a qualitative prospective from subjective reports rather than from quantitative and objective measurements. Quantitative and objective measurements of the musculoskeletal stress and lower limb numbness can be explored from various disciplines and techniques such as posture analysis, electro diagnostic testing, *anthropometry* (body measurements), body pressure distribution, intradiscal pressure analysis, behaviour analysis, biomechanical analysis and

physiological testing [18]. From these quantitative methods, body pressure distribution is the method of choice for the majority of seat discomfort research since it offers the best correlation with other quantitative and qualitative results.

Body pressure distribution also provides a non-invasive measurement of musculoskeletal stress and can easily be used in a large sample of subjects. The focus of this section will be to critically review previous research on the body pressure sensing and pressure mapping often used to evaluate discomfort while sitting.

2.2.1 Body Pressure Sensing and Mapping

Sitting is one of the most common daily routines that may exceed the critical pressure levels that the human tissues can endure. Exceeding this critical pressure may induce discomfort and over time may lead to musculoskeletal pain [19]. According to T. Bryant et al. [20] moderate discomfort can be reported by 90% of subjects under study when the average surface pressure on the skin exceeds 20 kPa. However, in some cases, discomfort has been observed on passengers at only 16 kPa, which is the known value at which the blood flow decreases to zero in human tissue due to contact pressure (the actual pressure inside the tissue that closes the capillaries is 4.3 kPa). However, for prolonged sitting, the discomfort average value can be reported to be as low as 6.4 kPa [21]. Thus, pressure distribution on the body surface can be used as an indicator for the maximum load on the body before discomfort is reported.

Even though there exist a large selection of technologies that are capable of measuring surface force and/or pressure, some sensors are fundamentally impractical due to physical design limitations or economic reasons. Therefore, these types of sensors are not discussed in this thesis. The most important parameters used to evaluate the sensors include the range of load, dynamic range, over force, sensitivity, span, linear error, repeatability, operational temperature range, hysteresis, element's

size, and resolution [22]. Also, the sensors must be able to comply with human curvature and accommodate the appropriate range of expected deformation of the surface with loading, have a low sensor drifting, remain accurate and produce consistent results with a reasonable calibration procedure.

There are currently two technologies used to map the body pressure distribution when in contact with a surface that meet these requirements – capacitive and resistive sensors. These sensors can be used in a wide range of applications due to their thin and flexible design that conforms with both rigid and highly elastic surfaces. The methods discussed in this section used one of the following two sensor systems to evaluate the pressure between the subject and the surface under study (for a detailed description of each technology please refer to Appendix E).

2.2.1.1 Capacitive Sensors

The XSensor[®] pressure sensor (XSENSOR[®] Technology Corporation, Calgary, AB, Canada) shown in Figure 2-1, is the most common capacitive pressure imaging system available commercially. The XSensor[®] consist of a thin and flexible matrix film integrated with capacitive sensor elements. This film is placed between the two contact surfaces and connected to a computer. When a force is applied to the film's surface a change in the capacitance in the sensing element(s) occurs. Their change in capacitance correlates to a change in surface pressure. The pressure distribution data is displayed graphically in real time in the computer's screen or in a handheld screen. In order for this sensor to work properly, non-linearity, hysteresis, and creep must be compensated for in the accompanying software [23]. Disadvantages of the XSensor system are poor system integration and its high cost (approximately \$29,000 USD as of mid 2016).

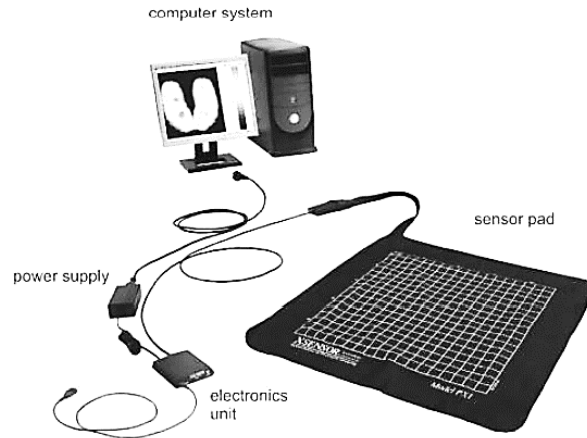


Figure 2-1: XSensor[®] system setup [23].

2.2.1.2 Piezoresistive Sensors

The main manufacturer of piezoresistive force sensors is Tekscan (Tekscan, Inc., South Boston, MA, United States). Tekscan produces a large variety of sensors and systems that are intended for pressure measurement. Their application ranges from medical devices such as MatScan[®] (for foot pressure measurements), industrial and agricultural pressure measuring systems (Figure 2-2 a) to automotive ergonomic applications such as the Body Pressure Measurement System - BPMS[®] (Figure 2-2 b).

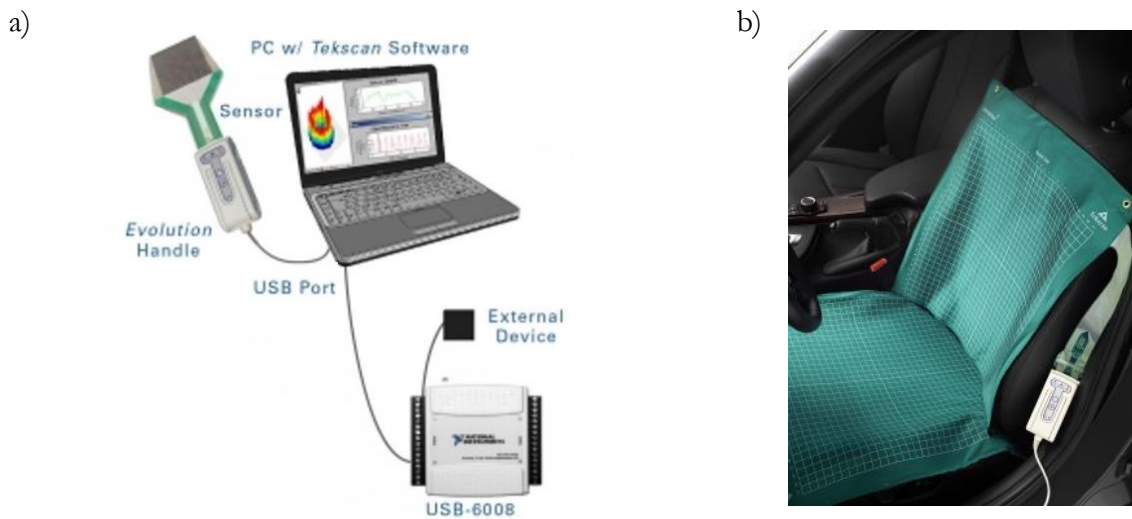


Figure 2-2: a) External input and trigger synch box setup [24], b) BPMS pressure mat [24]

Alternatively, single point sensors can be used together to create a custom and economical solution to surface body pressure measuring. The FlexiForce[®] shown in Figure 2-3 is Tekscan's single point foil sensor element. It is user-friendly and highly customizable. The sensor element can be adjusted for wired or wireless (WIFI or Bluetooth) operation, along with customizable sampling rate (up to 200 Hz). This sensor is designed to measure force loads, however, it can be adjusted to convert the measurements into “rough” discretized pressure measurements (as point cloud). However, the calibration and normalization process when used in a cluster fashion tends to be quite involved and time consuming [24], [25].



Figure 2-3: FlexiForce[®] model HT201 sensor [59].

Interlink Electronics offers Force-Sensitive Resistors, FSR[®], (Figure 2-4) which are highly customizable and provide the best cost-efficient option to measure load forces on surfaces. FSR come in different force ranges, sizes and shapes to accommodate design needs. FSR as its counterpart, FlexiForce[®] sensors, are intended to measure force loads, but can also be adapted to measure pressure. When a force is applied to the surface of the sensor, the resistance decreases in a nonlinear fashion. However, in some applications it is better to measure the inverse of resistance (conductance). FSR have a low accuracy (± 5 to ± 25 %) depending on test condition and calibration, but a good resolution of about $\pm 0.5\%$ of max load. It is important to mention that proper calibration of these sensors is difficult. FRS tend to have a saturation limit (around 10 kg) due to compressive force, and a switch-like response or “break force” at low force [26]. Other suppliers of piezoresistive sensors include LuSense, and Sensitron.



Figure 2-4: FSR[®] model 402 single zone [26].

2.2.2 Existing Methods for Body Pressure Measurements

The majority of the surface pressure mapping and imaging research in the literature has been conducted using the aforementioned XSensor, mostly due to their diverse selection of sensors and the ability to customize both the software and hardware. The research conducted by Chen et al. [27] made use of the XSensor 40" x 60" pad to develop a method to approach rigid surface seat design. The pressure data collected was a point cloud map and it was used to form an organic surface with CAD software RHINO (Rhinoceros 3D McNeel, Seattle, WA, USA). The researchers repeated the experiment to ensure reliability of the data, and recorded basic anthropometry of the subjects. The resultant curvature that mathematically combined the pressure distribution from the subjects was later used to create an inflexible static seat design. The expectation of the study was to increase the surface area of the rigid seat design in order to reduce localized pressure and stress on the hip and ischia area by dispersing the pressure throughout the human body buttocks. The results showed that only 10% of the tested subjects found no discomfort, 40% noted no difference in discomfort and 50% reported more discomfort compared to the flat seat. From this study it is clear that design of static (rigid) seat and pressure distribution data alone it is not sufficient to create a good seat design.

The Seat Pan Distribution Percentage, SPD% for short, was the first objective metric developed to measure discomfort. It was formulated by Ahmadian et al. [28] in 2002 to serve as a reference when body pressure distribution measurements were taken in order to evaluate discomfort. Along with pressure point percentage and oscillation defined as pressure points greater than 6.4 kPa (in both pan and back) and the number postural shifts when pressure reached 6.4 kPa during a 2-hour

period, respectively. Le et al. [21] first made use of the SPD% metric with the XSensor Pro X3 pressure measuring mat with promising results. This objective metric will be explored further in §3.1.2.

Looze, Evers, and Dieen [29] studied a variety of methods to determine more significant indicator of sitting comfort. Their study showed that pressure measurements combined with subjective evaluation was the most reliable indicator. Later studies on pressure mapping adapted these findings and established the three best attributes that provide efficient pressure distribution - low average interface pressure, low peak/maximum interface pressure and highest skin contact area between the passenger and seat [18], [30]. These properties can be easily computed in the software for the XSensor, Tekscan and single point element clusters sensors.

Chen et al. [18] researched the relationship between the pressure distribution and the influence of back angle on office chairs. They conducted the experiment using the XSensor Pro V6 in order to evaluate the optimal back angle for comfort. The researchers used the peak/max pressure, mean pressure, contact area and back pressure curvature to obtain the most comfortable back angle. Their experiment showed that at 105° (upright position + 15° recline) the subjects reported the highest level of comfort (lowest level of discomfort) as shown in Figure 2-5. This result was clearly consistent with their pressure measurements (back pressure value was the lowest at this angle). However, their sample size was small, and limited anthropometry data from the subject was collected. Also, the research failed to mention the calibration process used, if any, and only a single test was conduct per individual.

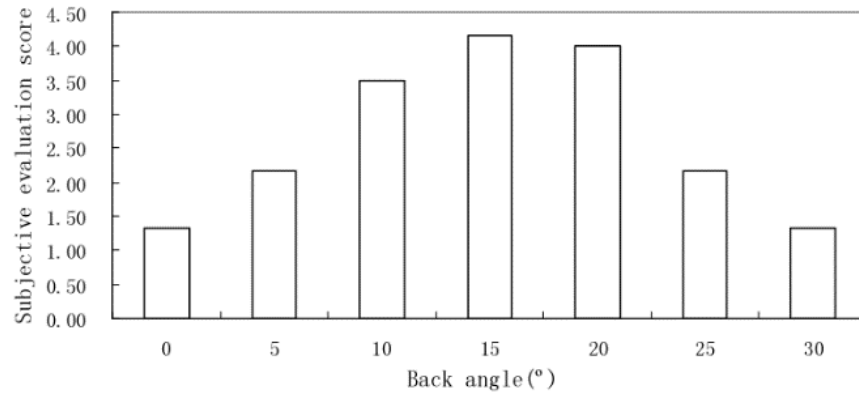


Figure 2-5: Relation of back angle and subjective comfort (90° -120°) [18].

2.2.3 Alternative Quantitative Measurements of Sitting Discomfort

Le et al. [21] also implemented two additional physiological measurements, local muscle oxygenation, monitored via near-infrared spectroscopy (NIRS) at a sampling rate of 50 Hz, and muscle activity via electromyography (EMG) at a 1000 Hz sampling rate (notch filtered to 60 Hz). Both, the oxygenation and activity levels of 16 different muscles were used to classify physiological discomfort. The dichotomous classification between comfort and discomfort determined whether the muscle oxygenation or activity values fell below the threshold during the 2-hour long experiment. These measurements were combined with subjective self-reported discomfort from the subjects and the previously mentioned pressure mapping using the XSensor Pro X3 in order to best define quantifiably seating discomfort. The model can be defined as sufficiently robust since it was repeated 10 times and the mean was used for each cross-validation trial. However, the muscle oxygenation and activity data from the research did not support this claim. This suggest that comfort thresholds for these two attributes are highly individualized and driven by the subjects' anatomy and possibly fitness level.

2.2.4 Methods for Calibration of Pressure Sensors

Little is known about the validity and reliability of pressure sensing on the human body. The challenge lies mainly on the complexity of the human anatomy and the difficulty to control external

variables which might impact the performance of the sensors [19]. Also, piezoresistive sensors have a highly nonlinear characteristic, so that a nonlinear force-to-voltage relationship must be calculated for each sensor [31]. Since the reliable use of the sensors depends highly on proper calibration methods and data handling method it is important to examine them carefully and apply the proper calibration methodology [32].

This section will be dedicated to examine the existing methods for calibration of piezoelectric sensor, with emphasis on FSRs and FlexiForce sensors. This is because these types of sensors provided the most cost-effective option for body pressure measurement. Also the static and dynamic calibration will be explored as it often encountered during the normal operation of these sensors.

2.2.4.1 Linearization and Calibration of Piezoresistive Sensor Measurements

Piezoresistive pressure sensors are highly durable and thin. They tend to be a good option for body pressure measurements since they are intrinsically pressure sensors and do not need to be highly modified to measure contact pressure [33]. The theoretical operation of the piezoelectric FSR describes the sensor's electrical resistance to be approximately linear in a log-log plot (Figure A-0-11, App. E) with an applied force [26]. However, during actual applications, this is not always the case, hence it is important to follow a proper calibration process and statistical analysis.

Another important factor to take into consideration is the saturation limit of the sensor. Since the compressibility of the polymer in foil piezoresistive sensors is finite, the conductance of such sensors often exhibits saturation. The saturation limit ($> \sim 10$ kg) is more a function of pressure (> 689 kPa to 1.4 MPa) than force. Thus, special care is needed for inelastic force measurements, as the pressure might not be properly distributed across the sensor's active area. As suggested by the manufacturer [26], this can be easily fixed by spreading the force over the entire active area and hence allowing to keep dynamic response in the sensor.

As first explored in 1991 by Jensen, Radwin, and Webster [33] this can be accomplished by adding a coating of epoxy resin to the active area of the sensor (Figure 2-6). Even though their research used a primitive calibration process for piezoresistive sensors (via strain gage dynamometer with data fit using a second-order polynomial equation using linear regression), their technique for distributing the loading over the sensor's active area provided a great improvement over the pressure saturation problem, and was later used in both inelastic and elastic cases by other researchers. The setup was for a force range of 1 – 45 N ($R_M = 6.2 \text{ k}\Omega$) at 40 Hz sampling rate for 2 s intervals. Their research also investigated the temperature and shear effects of the FSRs and concluded that deviation of -0.5% of full scale occurred per degree Celsius, and no systematic relationship between shear force and sensor response (with error $\leq 1 \text{ N}$) were observed.

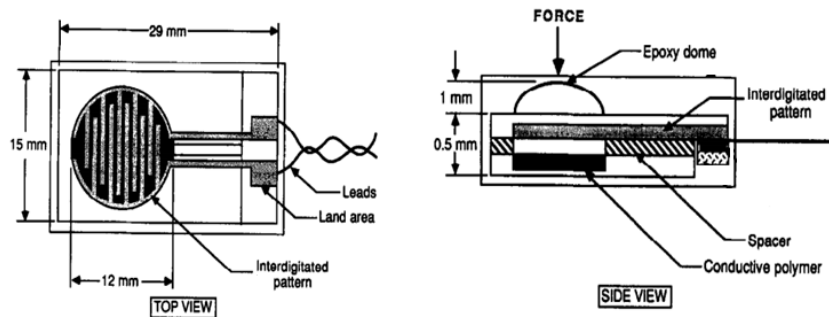


Figure 2-6: Diagram of epoxy resin dome covering the sensor's active area (Modified) [33].

Before the linearization method of FSR measurements was developed, weighting factors were used by Ferenczm, Jin and Chrizeck [31]. These weighting factors were found from the nonlinear least squares minimization of the prediction error with a brief inaccurate on-line calibration. The method for linearization and calibration of the piezoresistive sensors (FSR) on rigid surfaces was developed in 1997 by Zehr, et al. [34] in order to measure the forces occurring under the subjects' feet during locomotion on the grounds and treadmills. Even though the linearization was done assuming solid surfaces, the results were an improvement over the previous methods for this type of force measurements.

Another important contribution to the calibration methodology for FSRs (Interlink Electronics Model 402 FSR) was done by Florez and Velasquez [32]. The researchers refined the calibration procedure by compensating for the unwanted behaviours common in the static and dynamic operation of FSRs, including creep and hysteresis when a time constant and variable force, was applied, respectively. Their methodology also used the circuitry recommended by the manufacturer shown in Figure 2-7. The value for R_M was selected to optimize the sensitivity of their working range (0 kPa – 13.33 kPa using $R_M = 2.2 \text{ k}\Omega$).

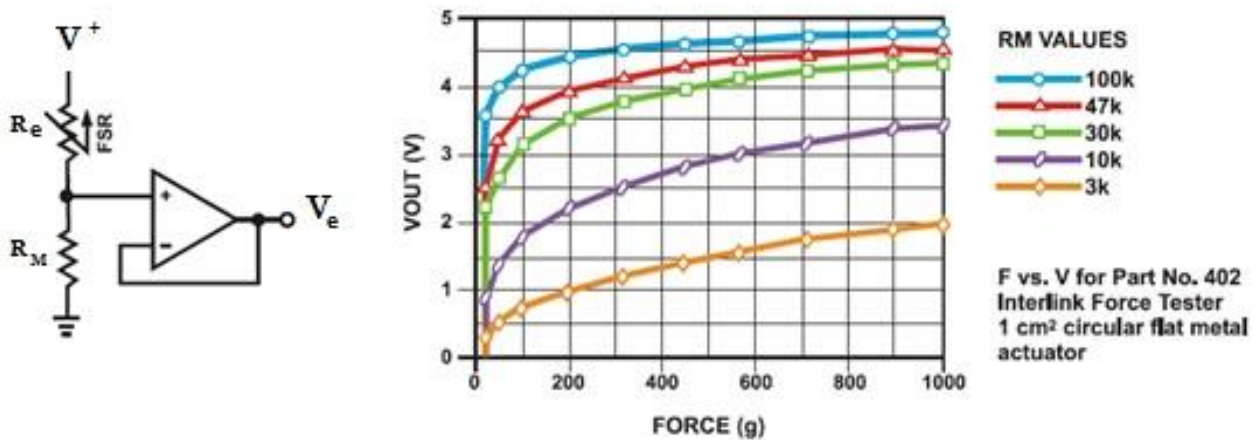


Figure 2-7: Suggested electrical interface (force-to-voltage) for FSR with R_M values [26].

2.2.4.2 Elastic & hyperelastic Calibration of Piezoelectric Sensor Measurements

For most applications a simple linear calibration on a rigid surface is sufficient. However, for measuring loads on materials with great deflection a different type of calibration is needed. Hyperelastic materials tend to deform significantly with small loads, this deflection creates a different response on the pressure sensor, and it must be taken into account. Most human tissue (such as fat, muscle and skin) and some polymer foam (often used in the seat cushions, i.e. polyurethane) can be model as hyperelastic material, while bone tissue and high density urethane foam can be modeled as elastic material [16]. Thus, it is important to calibrate the piezoresistive sensors accordingly to

accurately measure the contact pressure distribution between the human body and the seat's foam cushion.

As previously mentioned, the poor properties of piezoresistive sensor (non-linearity, low repeatability, time drift, creep and hysteresis) make them adequate for qualitative rather than quantitative measurements, but for some applications they seem to be adequate. This is especially true if a proper calibration is performed on the individual sensor elements, in particular for non-linear mechanic applications [35], [36].

Krkljes, Nagy and Babkovic [35] investigated the force dependence on the contact area of FSRs. They used a dome-shape rubber elastomer, best described by the hyperelastic Aruda-Boyce model to excite the FSR. The elastomer stiffness and shape plays an important factor on the linearity of the sensor. The researchers suggested a power-law function, based on the analytical study of the mechanical and electrical behaviour of the system. The results of this hyperelastic calibration (seen in Figure 2-8, below) shows a strong agreement between the power-law and the experimental data for values below 1.4 MPa, and diverting at higher pressures. This could suggest that possibly a piecewise calibration with power-law could provide better results in compensation for the saturation observed after 1.4 MPa.

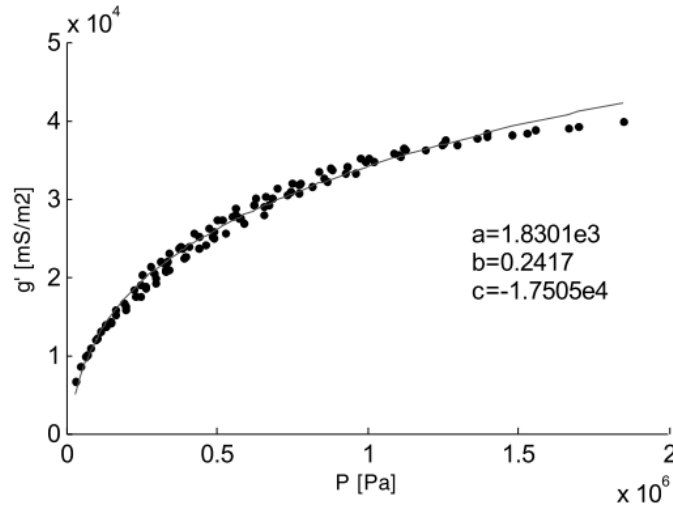


Figure 2-8: Static conductance per unit surface (dots) and fitted curve (line) vs pressure [35].

Wettenschwiler et al. [19] suggested a similar calibration process as [35] with the Tekscan 9801 piezoresistive sensor in real life applications. Their goal was to try to find the loads on the human body due to carriage systems (i.e. military ballistic vest, load bearing vest, etc.). In their approach, the sensor mat was first placed directly on the human body and a base measurement was taken (reference values). The reference values were later subtracted from the experimental values. Equalization and normalization of the array were also conducted. Their findings, however, showed a poor intra-subject, test-retest reliability (55% error for average pressure and 91% error for peak pressure). Even though their research looked at the most important external factors that often affect the performance of the sensors (humidity, temperature and contact material) the mounting of the sensors on the skin was not exactly precise. The large errors could suggest some unaccounted movement of the sensors as the subject performed the experiment or the difference the mechanics of their tissue. It is important to note the difference in the error between [35] and [19], which was a real application.

2.3 Methods for Material Contact Modeling and Simulation

Originally classified as “rubberlike” materials, now recognized as hyperelastic materials are considered to be isotropic and are practically incompressible, relative to its undistorted state (ground

state). Such materials are nearly perfectly elastic for large quasi-static deformations. For this reason, it is convenient to treat these materials as perfectly elastic in order to postulate a strain-energy function that describes their mechanical properties under deformation at constant temperature. Ogden [37] originally postulated in 1971 such formulation of a strain-energy function which inheritably describes the isotropic elasticity properties of the “rubberlike” materials.

Non-linear hyperelastic materials deform easily by small forces, and their deformation is out of proportion to the applied force, and tends to break with higher forces than elastic material. Previous theories tended to overcomplicate the mathematical description of the observed experimental evidence of such materials. The derivation of the Ogden hyperelastic material model describes the non-linear stress-strain behaviour of complex materials, such as rubbers, polymers and some biological tissues is quite involved and will be excluded from the present work (but it can be found in [37], and will partially be discussed in CHAPTER 3).

In order to develop an ergonomic product (i.e. chair cushion) based on pressure distribution comfort, numerous body pressure measurements on different prototypes must be tested with different people. This is both, a time consuming and expensive task. Current research on non-linear FEM of hyperelastic material present an alternative to inexpensively and efficiently model and estimate the pressure distribution on the human body. In contrast, the stress and strain analysis for elastic materials (performed by FEM) required the material’s properties such as its Young’s modulus, E , which shows the stress and strain relation, and its Poisson’s ratio, ν , which describes the negative ratio of transverse to axial strain.

In 2010, Gras, et al. [38] attempted to model the sternocleidomastoid muscle (bone-muscle-bone) behaviour under loading conditions. They compared the muscle behaviour under tension (of 10 sternocleidomastoid muscles dissected from 5 female subjects) to their theoretical model of a

hyperelastic law based on Ogden’s hyperelastic equation with inclusion of Poisson’s ratio, since muscle is essentially incompressible. The researches simplified the geometry of the muscle and considered the muscle’s cross section to be an ellipse.

The researchers compared the data from the tension test and the theoretical simulation and it proved to give good results since the R^2 ranged from 0.9967 to 0.9999, but their theoretical shear moduli did not fit the observed data, and suggested to further research on Ogden’s equation using FEM.

Ishihara, Ishihara and Nagamachi [39] researched the finite element model of the human body to visualize the pressure, stress and displacement using hyperelastic FEM. Using the anthropometry data from a national database (AIST, 1992) along with anatomical and MRI images of the human body, the researches modeled the skin, fat, muscle and other soft tissue as a non-linear hyperelastic material (via Ogden’s formulation). While bone tissue was model as non-linear elastic material. The material properties shown in Table 2-1 were used in [39] and obtained from their references [10, 11].

Table 2-1: Hyperelastic and Elastic Constants of the Human Body and Cushion Material [39].

Hyperelastic Materials	μ (MPa)	α	ρ (kg/m³)
Fat	0.1	30	1200
Muscle	0.003	5	1056
Skin	0.008	10	1053
Elastic Materials	E	ν	ρ (kg/m³)
Bone	2×10^4	0.3	800
Esophagus & Trachea	0.047	0.49	1056
HD urethane	0.025	0	48

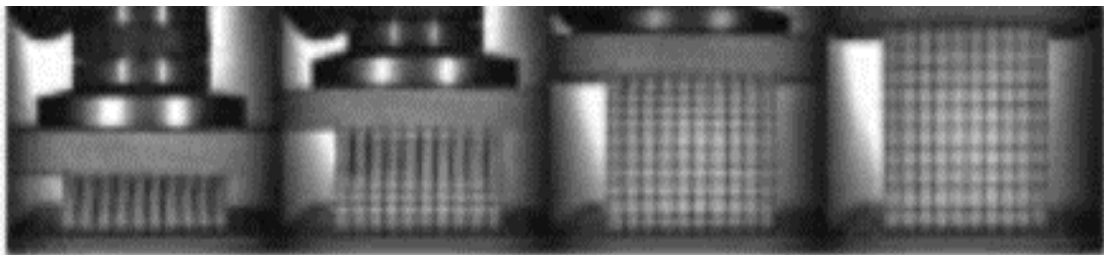
Their contact analysis was done between an elastic surface (mattress composed mostly of HD urethane) and the hyperelastic model of the human body (weight of 60 kg), using a friction coefficient of 0.5 to avoid sliding between the surfaces. The FEM analysis used ANSYS® (ANSYS, Inc., Canonsburg, PA, USA) with tetragon mesh. The undersurface of the mattress was fixed. Their results showed an average pressure around the sacrum of 4.27 kPa (with peak value of 5.2 kPa), while the actual average pressure (measured from a 63 kg male subject, using an FSA pressure system (with unspecified performance characteristics) by Vista Medical, Winnipeg, MB, Canada) was 4.17 kPa. Simulations for the upper shoulder were also performed and the simulated average pressure of 1.32 kPa was determined (with peak pressure of 3.83 kPa), compared to the actual average pressure of 1.12 kPa. The difference from the actual values and the simulated values (2.39% and 17.86 %, respectively) could be due to the pressure measuring system used in the experiment as it is only accurate to ± 20 % of full load, and the calibration process (if any) was not mentioned. Also, imperfection/variations on the actual materials (i.e. of the mattress and the human body) could have led to different values compared to the model, which assumes isotropic incompressible elastic and hyperelastic material, respectively.

2.4 Methods for Modeling and Measuring the Stiffness of Materials

The selection of the mathematical model for hyperelasticity depends on its ability to accurately match the strain energy under a large range of deformation. Selecting the appropriate model for the material combination is a difficult task, especially for biological materials such as human tissue. The most relevant models for hyperelastic non-linear materials include Mooney-Rivlin, Ogden, Yeoh, Neo-Hookean, Gent, Polynomial and Aruda-Boyce model. The latest research seem to suggest that, at least, for human tissue modeling, the Ogden and Neo-Hookean model are more suitable as shown by experimental results [40].

The hyperelastic model can help in the design process of the cushion material that it is comfortable to humans. The first step in trying to fix the challenge of uncomfortable seats design can be the in-depth analysis of the human-seat system. In particular, the analysis of the mechanical properties of the cushioning material. It is often common for the seat cushion material to be a polymer foam, polyurethane being a popular choice due its characteristic high-resistance to wear and ease of manufacturing. Polyurethane (PU for short) foams are network-forming cell materials with low stiffness, low Poisson ratio, low density and the ability to absorb strain energy and slow recovery rate. They are two main types of PU foams, open and closed cell, depending on the form and connectivity of the cells within the material. Unfortunately, PU mechanical behaviours is poorly understood [41]. Figure 2-9 demonstrates a typical PU foam strain-deformation diagram. The diagram consists of three distinctive phases with different moduli of linear elasticity E_1 , E_2 , E_3 . The first stage occurs (below 5% of the complete deformation) due to the bending of the foam's cells. In the second stage, larger deformation is encountered due to the loss in stability of the cell structure of the foam. The last stage is characterized for a substantial increase in rigidity of the foam due to the compression of the deformed cell structure.

PU Foam: T4060



a) 70 % b) 50% c) 25 % d) 0 %

Figure 2-9: Foam deformation under axial compression at different compression % [42].

Smardzewski, Grgac and Prekrat [42], approached this very problem by developing a numerical model for such complex layer system (human-foam system). The researchers used the basics of the non-linear Mooney-Rivlin model (refer to App C) to conduct a numerical analysis of the contact mechanics in the seat material. As the selected materials, they used 4 types of PU foams: T2516, T2838, T3530 and T4060. Compressive testing on the foam samples were conducted (Figure 2-10) and the rigidity moduli curves were obtained. The researchers used the experimental data to establish the constants C_{10} , C_{01} from the Mooney-Rivlin model (assuming two coefficient of frictions $f_{model1} = 0.8$ and $f_{model2} = 0.4$ between the human body and the foam).

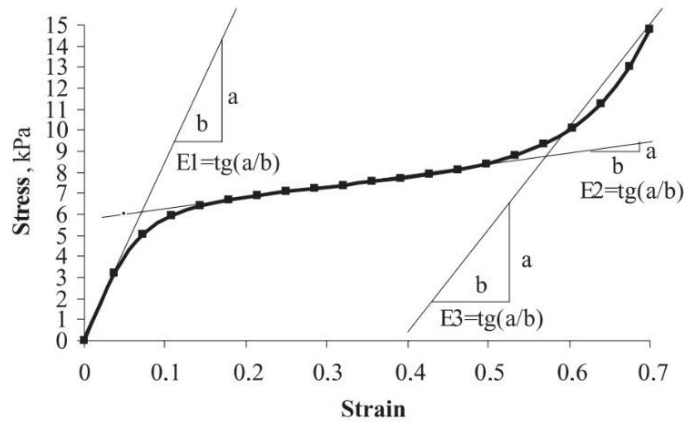


Figure 2-10: Typical strain deformation for PU foam [42].

The numerical hyperelastic PU foam-human body system model was developed in ABAQUS® (Dassault Systemes, Waltham, MA, USA) software in order to calculate the strain and deformation of the foam. The numerical analysis showed strong correlation to the experimental data, and was later used for modeling the contact mechanics of the system. The researchers found that foams T2838 and T4060 have a better pressure distribution compared to the T2516 and T3530 foams. It is important to mention that the researchers performed the tests using solid plates to compress the PU foam, which might affect its true behaviour of non-linear mechanics.

In order to model the stiffness of the pressure controlled surface of the seat (air-spring) we first must examine the contact mechanics of an inflated non-linear hyperelastic membrane pressed between two surfaces. The surface under consideration consist of the cushion foam and the human body, both hyperelastic materials. The goal of the stiffness control via the pressure bag is to evenly distribute the pressure between the human body and the cushion. To account for the change in the stiffness of the pressure bag, we need to understand the mechanics of deformation of hyperelastic inflated membranes with contact. However, in the current literature, while the free inflation of hyperelastic membranes has been thoroughly studied, the contact problem with non-linear contact mechanics has not been explored properly. Kumar and DasGupta [43] investigated a simplified version of such mechanics. In their work, the symmetry of the inflated membrane was kept simple (spherical membrane) under symmetrical rigid plates. The researchers used the Mooney-Rivlin strain energy function for the membrane deformation and the potential energy of the inflating gas under isothermal conditions. The researchers also looked at this problem from a frictionless, no-slip and stick-slip contact conditions. This research can be used to simulate the expansion and thus the change in stiffness of the hyperelastic membrane (air-spring) that will be used to control the pressure distribution of the morphing seat. This model is particularly important since the stretches and contraction for the non-slip contact with initial pressure and volume, can be determined from this from the initial radius (uninflated), the radius of the sphere and the thickness of the membrane.

However, the model was only developed for spherical hyperelastic membranes in contact with solid plates, but it can be considered a good start to apply it to the actual membrane geometry and contact mechanics for the air-spring in the morphing seat design.

2.5 Summary of the Literature Review

In summary, most current studies on the comfort/discomfort topic do not show a definitive relationship between the seat parameters and the passengers' anthropometry features. However, most of the current comfort/discomfort research demonstrates a stronger correlation between the pressure distribution and the cushion's geometrical properties (shape, dimensions and recline angles) than its material properties (i.e. stiffness). From this, it can be concluded that 1) proper calibration of the pressure sensors must be done for the specific seat geometry and 2) the seat geometry is more important to comfort/discomfort predictions than its material properties. Thus, creating a seat with morphing geometric features is more advantageous to comfort/discomfort research than other seat design aspects. The approach in the following chapters will use this knowledge and comfort/discomfort models, specially the ones related to pressure distribution. This is yet another reason to further explore the challenge to accurately predict comfort/discomfort for a given design.

Furthermore, this literature review discussed the theoretical and technological requirements needed to develop a morphing seat capable of surface pressure adjustment with the goal of increasing passenger sitting comfort (more accurately, decrease passenger's sitting discomfort). Moreover, the existing methods for body pressure sensing and mapping, along with existing technologies and calibration methods were presented. And lastly, the contact mechanics and stiffness measurements along with their respective simulation techniques for elastic and hyperelastic materials were discussed in order to approach the challenge of creating a model to better understand comfort/discomfort from the aspect of material's property.

CHAPTER 3 Seat Modelling and Analysis

In this chapter, the design of the seat curvature can be derived from the ideal pressure distribution and ergonomics in order to match the curvature of the human body in the most comfortable (more precisely, least uncomfortable) sitting posture. In other words, a comfortable (least uncomfortable) seat design must provide a matching curvature to the physiological curvature of the human body. And such interaction should produce an optimal pressure distribution. As discussed in CHAPTER 2, the seat's cushion *ground state* design and its recline angle affect the seat's comfort (discomfort) rating more than its material properties. Thus, it is better to focus on the seat's contour curvature more than its material properties.

This is difficult to achieve in a conventional static seat design because passenger's weight and anthropometry is significantly different between the population. Alternatively, a seat design can be created to adjust its surface curvature with the purpose of decentralizing the pressure distribution. In turn, this adjustment of the surface curvature in real time can create a more comfortable (less uncomfortable) seat contour that is specific to each passenger.

Furthermore, the problem can be subdivided into developing a surface contour model with a reference value that can be used as a feedback. The reference value (or value set) must work for any reclined configuration. The required actuation must correspond to the difference between the deformed surface contour (caused by the applied load of the passenger's weight over the ground state of the seat cushion) and the 'ideal' contour of the seat's surface based on the ideal pressure distribution. The end goal should be to produce a change in the backrest surface so that such change in contour creates a pressure distribution closely resembling the reference value, while keeping the BRD% as the parameter used to evaluate the effectiveness of the adjustment.

During the derivation of the mathematical model in this chapter, the following assumptions have been made to simplify the analysis presented in this chapter:

- 1) The sensor layer, which is mostly made out of vinyl, thin copper tape and silicon does not contribute significantly to the contact mechanic model. And thus, it can be neglected.
- 2) Clothes' mechanical behaviour is negligible to the contact model.
- 3) The only atmospheric pressure change affecting the model comes from the pressurization of the cabin during flight (from $P_{SSL} = 101.325$ kPa to $P_{cruise} \sim = 77.9$ kPa)

Also, to model the material deflection, Ogden's hyperelastic strain-energy function had been selected for this study for its two advantages over similar model: 1) Accurate representation of mechanical response, 2) Its mathematical simplicity relative to alternative contact models. However, tabulated data from the experiment is preferred over the model to reduced computational time.

3.1 Seat and Sitting Models

The reaction forces on the seat's backrest surface must be fully understood and derived before developing the hyperelastic deflection model and the corresponding control method. Once the surface pressure is related to the sensor measurement and the foam deflection, the control system can be developed. The control system's task will be to adjust the centralized load distribution across the human back while sitting.

Firstly, as seen in Figure 3-1, the origin of the coordinate system used throughout this work is located to coincide with the position of sensor $e_{1,1}$. The pressure distribution, P , on the seat's initial geometry (known as the ground state), S^0 , are both defined on the *coronal plane* (YZ plane). Moreover, the reaction force can be divided into perpendicular and parallel components referred to as the normal force and shear force.

The reaction force is dictated by the ground state of the backrest cushion, S^0 , the cushion stiffness, k_c , the recline angle, δ , and the load profile on the seat from the passenger's body weight, known as the pressure distribution, P . The assumption is that the load on the seat is produced only as a result of the passenger's gravitational force on contact with the supporting surface. In other words, no load is generated from muscle or ligament tension. Furthermore, the recline angle is the main factor that affects the load distribution (for a given sitting position) since the normal force and shear force are functions of the recline angle.

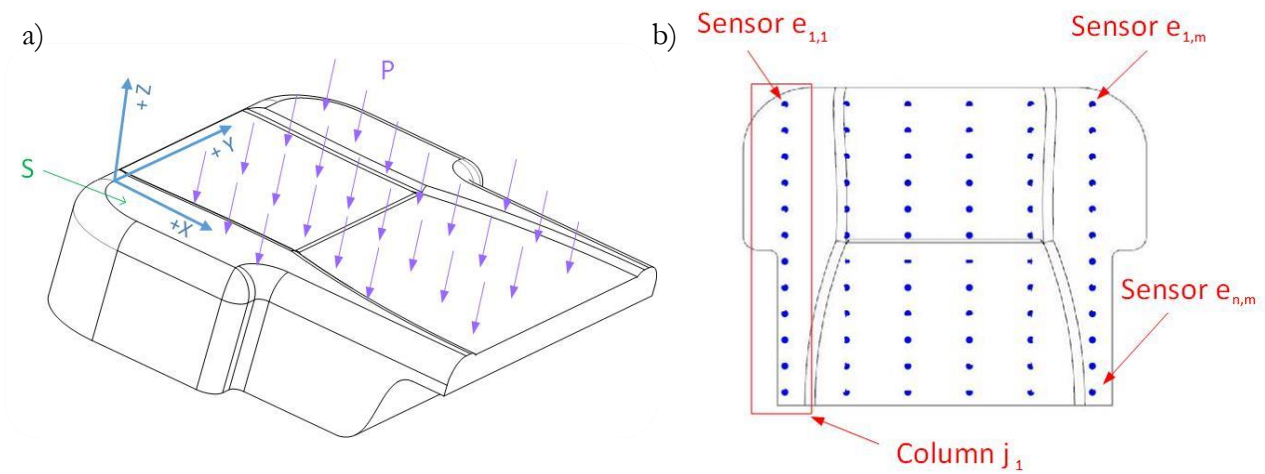


Figure 3-1: a) Coordinate system on the cushion, b) Sensor Location.

The majority of the ergonomic research for seat design based on biomechanical models uses high-order polynomials to describe the seat cushion's ground state, the resultant pressure distribution and the deflection of the cushion under the load. This is mostly because polynomial fit is a convenient and simple mathematical model to approximate the shape and reaction force on the seat. However, polynomial fit works for these types of models because the seat design is considered to be both passive and static. Such case can be seen in [44], where a biomechanical model is used based on the most comfortable cushion curve and can be expressed as a 11-order polynomial. And it is accompanied with the resultant pressure distribution as result from the load, which is also expressed as a high-order polynomial.

However, this method of representing curvatures and pressure distributions is ineffective for automatic adjusting seat designs - seat designs such as the one presented in this work. This is because quartic or higher-order polynomial tend to have instabilities. Cubic splines on the other hand, tend to preserve the shape and smoothness while providing a simple representation. Thus, splines in this particular case can overcome these limitations.

Before proceeding to the derivation of the reaction force components, the cushion's ground state curvature must be obtained for the specific seat design. This can be trivially done by measuring its foam cushion height, $s(x,y)$, at defined intervals (the control points) across its surface and modeling it as a group of cubic natural splines. The surface is approximated with a series of cubic natural splines since this model works best in this scenario. This is due to the fact that the deflection at the actuated control points changes significantly during operation and a high order polynomial fit can be ill-conditioned when a change in curvature occurs.

The seat's exact surface curvature at its ground state is presented in CHAPTER 6. For this chapter, only its general representation as a spline approximation is used to derive the model and the requirements for the control method and mechanism.

Firstly, the seat's ground state curvature as a 3D surface (Figure 3-1) can be defined as:

$$S^0 = f(x, y, z) \quad \text{Eq. 3-1}$$

where the upper indices are not exponents but instead indicate the state of the seat's surface (i.e. the upper index 0 denotes the ground (unloaded) state of the cushion).

Both the seat's curvature and pressure distribution are continuous inside the contact area. However, the sensors can only measure discrete points on the surface of the backrest. For this reason, it is necessary to discretize the surface to make use of the sensor data. Apart from discretizing the surface, it is also necessary to define a method to interpolate between data points that can be of use

with the controller. The entire surface can be discretized into m cross-sectional (m being the total number of control points in the y axis) curves on the XZ plane as seen in Figure 3-2. Each cross-sectional curve can be approximated by a cubic natural spline that has the form:

$$s_j = \begin{cases} s_{j,1} = a_{j,1} + b_{j,1}(x - x_{j,1}) + c_{j,1}(x - x_{j,1})^2 + d_{j,1}(x - x_{j,1})^3, x \in [e_1, e_2] \\ \vdots \\ s_{j,n-1} = a_{j,n-1} + b_{j,n-1}(x - x_{j,n-1}) + c_{j,n-1}(x - x_{j,n-1})^2 + \\ d_{j,n-1}(x - x_{j,n-1})^3, x \in [e_{n-2}, e_{n-1}] \end{cases} \quad \text{Eq. 3-2}$$

$j \in \{1, m\}$

where a_j , b_j , c_j and d_j are the cubic polynomial coefficients for each j^{th} curve, e_i is the sensor's location on the seat surface and m is the number of control points on each sensor row. For n control points (on the x axis), there are $n-1$ interval in each s_j spline. Each interval requires a cubic polynomial to approximate the curvature between two adjacent control points ($x_{i,j}$ and $x_{i+1,j+1}$). Since n must equal to the number of sensors, it is important to keep in mind the cost of the sensors (approximately \$9 USD per FSR sensor) when selecting the size of n . The magnitude of $s_j(x)$ can be approximated via spline interpolation at any point, x , to obtain the cushion thickness, $s(x,y)$. The traditional approach can be used to solve the spline system for an individual s_j curve (a column curve), with coefficients a_j , b_j , c_j

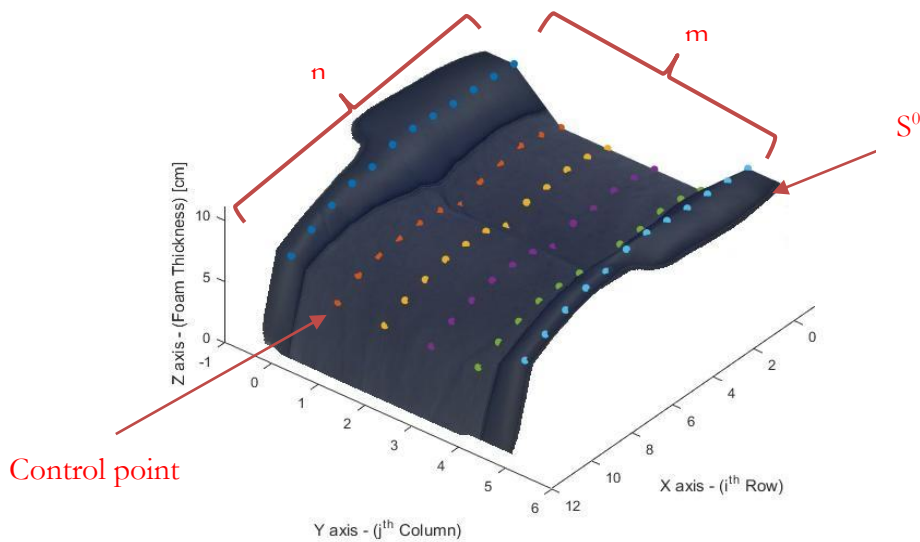


Figure 3-2: Discretized seat surface.

and d_j . Note that the location of each spline control point must coincide with one of the FSR sensor elements' location to be of practical use.

Furthermore, it is important to distinguish between the two different types of control points that exist in this design - the passive and actuated control points. The passive control points are only affected by the applied point load, $f_{i,j}$, at $x_{i,j}$, and the seat cushion's stiffness, k_c . While the actuated control points are affected by the applied point load, $f_{i,j}$, at $x_{i,j}$, the seat cushion's stiffness, k_c , and the internal pressure of the air-spring(s), p_s , – which is the control variable and provides the air-spring stiffness k_c .

Following this methodology, it is possible to define a related pressure distribution (continuous on the contact area) on the backrest caused by the applied load F on the seat's surface, S , as:

$$P = g(x, y, z) \quad \text{Eq. 3-3}$$

and by definition, at the ground state:

$$P^0 = 0, \quad \text{at } S^0 \quad \text{Eq. 3-4}$$

In a similar manner as with the backrest curvature, the pressure distribution can be approximated (via interpolation) by a group of m cubic natural splines from the discrete data as:

$$p_j(x) = \begin{cases} p_{j,1} = \widetilde{a}_{j,1} + \widetilde{b}_{j,1}(x - x_{j,1}) + \widetilde{c}_{j,1}(x - x_{j,1})^2 + \widetilde{d}_{j,1}(x - x_{j,1})^3, x \in [e_1, e_2] \\ \vdots \\ p_{j,n-1} = \widetilde{a}_{j,n-1} + \widetilde{b}_{j,n-1}(x - x_{j,n-1}) + \widetilde{c}_{j,n-1}(x - x_{j,11})^2 + \\ \quad \widetilde{d}_{j,n-1}(x - x_{j,n-1})^3, x \in [e_{n-2}, e_{n-1}] \\ j \in \{1, m\} \end{cases} \quad \text{Eq. 3-5}$$

where $\widetilde{a}_j, \widetilde{b}_j, \widetilde{c}_j, \widetilde{d}_j$ are the coefficients for the internal cubic polynomials connecting two adjacent control points of the pressure distribution. The coefficients a, b, c, d are related hyperelastically to the coefficients $\check{a}, \check{b}, \check{c}, \check{d}$ for the $f_{i,j}$ and p_s parameters.

Additionally, in order to fully describe the approximate curvature of the cushion at any state, all of the available column and rows cross-section curves (for an evenly distribution pressure mat) must be determined. It is also possible to have a discretized interpolation expression for the overall 3D surface of the seat's backrest and its related pressure distribution. These 3D surfaces can be approximated by multidimensionally interpolating the splines from $j=1$ to $j=m$, respectively and denoted as:

$$\tilde{S} = \langle s_j \rangle, \quad j \in \{1, m\} \quad \text{Eq. 3-6}$$

and

$$\tilde{P} = \langle p_j \rangle, \quad j \in \{1, m\} \quad \text{Eq. 3-7}$$

where tilde denotes the multidimensional interpolation approximation (from the discrete control points) of the surface. The interpolation method for Eq. 3-6 and Eq. 3-7 is also done via cubic natural splines for consistency of the method and to avoid instabilities. Thus, the approximate foam thickness, $s(x,y)$, and pressure distribution at any point $p(x,y)$ at any point $\chi=(x,y)$ can be done by interpolating from \tilde{S} and \tilde{P} , respectively.

After defining the approximation for the backrest surface and pressure distribution, it is now possible to relate those function to the actual discrete data gathered from the pressure mat. Let P_M be the resultant measured pressure distribution from the applied measured force, F_M , which is a function of recline angle, δ , seat cushion stiffness, k_c , the air-spring stiffness, k_s , the internal gauge pressure of the air-spring(s), p_s , and human anthropometry and positions (biomechanics), ζ .

$$P_M = f(F_M) \quad \text{Eq. 3-8}$$

more specifically,

$$F_M = f(\delta, S^0, k_c, k_s, p_s, \zeta) \quad \text{Eq. 3-9}$$

both, P_M and F_M are continuous over the contact area.

However, only the discrete force distribution \widetilde{F}_M can be obtained as point forces from each of the FSR sensing elements in the pressure mat. That is, given an evenly distributed set of data from the pressure mat, arranged in a $n \times m$ matrix, the point force for the mat can be expressed as:

$$\widetilde{F}_M = \begin{bmatrix} f_{1,1} & \cdots & f_{1,m} \\ \vdots & \ddots & \vdots \\ f_{n,1} & \cdots & f_{n,m} \end{bmatrix} \quad \text{Eq. 3-10}$$

where $f_{i,j}$ is the output in Newton (processed output will be explained in CHAPTER 4) from sensor element $e_{i,j}$. Naturally, the pressure distribution can be discretized as well:

$$\widetilde{P}_M = f(\widetilde{F}_M, A_a) \quad \text{Eq. 3-11}$$

where A_a is the active area of the sensor's element. This is possible only if the force acts in a small finite area. It can be concluded that this is generally a good assumption for this case since the FSR active area, A_a , is significantly smaller than the overall force distribution area of the seat's backrest. Consequently, it can be assumed that the force acting on the FSR element is constant over its entire A_a , lowering the possibilities of pressure concentrations over the active area. Additionally, since the surfaces are not rigid, uneven distributions are not likely to be encountered. Lastly, recalling that the FSR sensors are inherently pressure sensors and have a finite active area, it is adequate to assume Eq. 3-11 holds for this application

Thus, from the measurement of force, the corresponding pressure can be approximated. This approximation is improved as the active area of the sensing decreases. The change from force to pressure is simply given by:

$$P_M \approx \frac{F_M}{A_a} \quad \text{Eq. 3-12}$$

Using the matrix form of the pressure mat data, the discrete pressure distribution can be expressed as:

$$\widetilde{P}_M \approx \frac{1}{A_a} \begin{bmatrix} f_{1,1} & \cdots & f_{1,m} \\ \vdots & \ddots & \vdots \\ f_{n,1} & \cdots & f_{n,m} \end{bmatrix} \quad \text{Eq. 3-13}$$

Subsequently, an ideal or target pressure must be defined. Such target pressure, P_i , must result in the most comfortable pressure distribution. Recalling the ideal pressure distribution (as proposed by [12], [13]) P_i can be used as a starting reference target pressure. To do so, the target pressure distribution must be represented in percentage per body region (PBR for short), $\%P_i$. For simplicity, the backrest is limited to 4 main regions, in this study (Figure 3-3) where A_2 and A_3 are nearly identical.

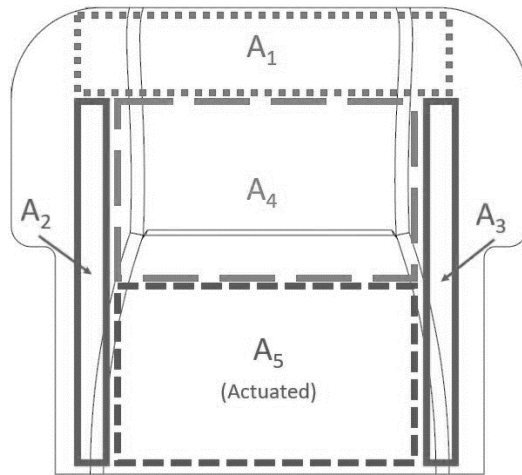


Figure 3-3: Backrest divided into 4 regions.

Since the analysis is done in the XZ plane, k_2 is assumed to be symmetric to k_3 and relatively small ($< 3\%$). Also, the values of the pressure coefficient of each area from Figure 3-3 can be found in Table 3-1.

Table 3-1: Coefficients for backrest regions.

Zenk (2008)	Mergl (2006)
$0.05 \leq k_1 \leq 0.12$	$0.05 \leq k_1 \leq 0.12$
$0.11 \leq k_4 \leq 0.34$	$0.20 \leq k_4 \leq 0.50$
$0.24 \leq k_5 \leq 0.38$	$0.24 \leq k_5 \leq 0.38$
$k_2 < 0.03$	$k_2 < 0.03$
$k_2 = k_2 < 0.03$	$k_2 = k_2 < 0.03$

The control problem, as will be discussed in CHAPTER 5 is simply a set point regulator that will use the pressure PBR, $\%P_i$, as the reference with the BRD% as an evaluation of discomfort. $\%P_i$ is derived from the ideal pressure distribution theory. That is, the reference pressure is defined as:

$$\%P_i = k_1 F + \dots + k_w F, \quad \forall \delta, \kappa_c, \kappa_s, \zeta \quad \text{Eq. 3-14}$$

where w is the number of regions in the backrest (w=5 for this case) and has the property of:

$$\sum_i^w k_i = 1 \quad \text{Eq. 3-15}$$

and the measured pressure distribution in PBR must approach the reference as:

$$\%P_M \rightarrow \%P_i \quad \text{Eq. 3-16}$$

in a finite time and with the control variable, P_s , which is the pressure curve that results from the change in geometry of the air-spring(s). Such distribution is a function of:

$$P_a = h(p_s, F(\delta, S^0, k_c, k_s, \zeta)) \quad \text{Eq. 3-17}$$

which is part of the resultant pressure due to the passenger's weight, F. k_c and k_s are the stiffness of backrest cushion and the air-spring, respectively. Overall, the measured pressure distribution (from

the force applied from the passenger's body weight) can be seen as the combined pressure of the static and actuated surface of the seat, that is:

$$P_M = P_b + P_s \quad \text{Eq. 3-18}$$

Or

$$P_M = f(\delta, S^0, k_c, k_s, \zeta) + g(p_s, \delta, S^0, k_c, k_s, \zeta)$$

where P_b , is the resultant pressure distribution when the load F is applied and before the actuation of the air-spring(s). However, there is no need to compute the function P_b and P_s for the parameter δ, S^0, k_c, k_s since F_M and p_s are directly measured. Thus Eq. 3-18 can be simplified as:

$$P_M = P_{b_M} + P_{s_M} + f(p_s) \quad \text{Eq. 3-19}$$

where p_s is the internal gauge pressure from the air-spring(s) that in turn exerts a pressure on the lumbar support area due to a change in geometry and stiffness.

In order to keep or achieve $\%P_M = \%P_0$, the actuator (air-spring) must deflect the surface of interest – the lumbar area. For the controller to know the desired deflection, two relationships (models) must be known:

- 1) The deformation of the foam core, ΔS^F , when the load F is applied. (F being the force due to the human body weight).
- 2) The deformation of the air-spring(s) as a function of internal pneumatic gauge pressure and the load, F . Or the current pressure distribution.

Furthermore, F is divided into m force distributions, f_j on the XZ plane. Each f_j is a 2D curve represented by a spline (similar to Eq. 3-5) and when the curves are multidimensionally interpolated using Eq. 3-20, the 3D surface, F , is approximated as \tilde{F} . This approximation increases in accuracy as the sensor density, ρ_{sensor} , increases.

The interpolation can be improved by knowing the biomechanical model along with the anthropometry model (or actual body measurements of the passenger that can be known by either having image recognition or proximity sensors in the seat) for a more precise interpolation between curves. After obtaining f_j from all the sensor elements from all columns, \tilde{F} can be written as a 3D surface in the form of:

$$\tilde{F} = \langle f_j \rangle = \langle e_{i,j} \rangle, \quad j \in \{1, m\} \quad \text{Eq. 3-20}$$

$$i \in \{1, n\}$$

For \tilde{F} , the pressure distribution can be inferred from the individual force measurements, $e_{i,j}$. The measured pressure distribution as $\%P_M$ region can be obtained from the pressure sensor data as:

$$\%P_M = \frac{\%F_M}{A_a} = \frac{1}{A_a} (q_{1,m}f_1 + \dots + q_{w,m}f_m), \quad \text{Eq. 3-21}$$

$$\sum_i^w q_i = 1$$

where $q_{i,m}$, is the backrest region coefficient for the measured pressure distribution as $\%P_M$.

The values ranges for q_i are good estimates for determining the ideal pressure distribution. However, the downside of having a range of values instead of an unique value for each q_i is that the controller complexity increases. To simplify the controller design, it is recommended to find a unique solution, if it exist. To do so, a biomechanical model can be combined with P_i to reduce the range of q_i or possibly find the unique solution. It is equally likely that for some passengers' anthropometry and/or position, no solution exists that satisfy both models. Thus, for those cases, parameters of the biomechanical model can be *relaxed* to find a possible solution for the ideal pressure distribution, P_i , that serves as the set point reference. A simple biomechanical model can integrate the joint angles that are found to be the least uncomfortable whilst sitting. These joint angles and their curves are obtained in a similar manner as in [44] which will be discussed in §5.2.2.

3.1.1 Human-Seat Contact Model

In order to model the mechanical properties of human tissue, it is important to consider carefully the important components that make the tissue. These include the mechanical properties of tissues involved (i.e. skin, muscle, adipose tissue, etc.), the dimensions and anthropometry of the human back (for backrest) and lastly, the expected load profile and magnitude that is often encountered in realistic cases.

Firstly, the area of each of the 4 different region on the backrest can be given as a percentage of total area (Table 3-2). The surface contact area A_c between the seat and the passenger has to be determined to be included in the contact model. A_c can be roughly approximated from the pressure mat by identifying the active FSR elements. The accuracy of A_c is determined by the FSR element density in the mat and its accuracy is proportional to the sensor density:

$$\rho_s = \frac{mn}{A_b} \quad \text{Eq. 3-22}$$

where A_b is the total backrest area.

Table 3-2: Area percentage for the backrest regions.

Backrest Region	Area %
A_1	12.78
A_2	8.73
A_3	8.73
A_4	24.73
A_5 (Actuated)	24.73
A_N (no sensors)	20.30

For an evenly spaced pressure mat (which is the case for all commercially available pressure mats and including the custom-made pressure mat for this experiment) A_c can be calculated as:

$$A_c = e_a A_e \quad \text{Eq. 3-23}$$

where e_a is the number of active sensor elements in the mat and A_e is the area of the sensor's element. Ideally, the area of the sensor should be equal its active area ($A_e = A_a$). Since the sensors are not continuous point elements, there exist some spacing between them. The configuration for the sensor distribution in the pressure mat used for the controller in the ALAS system can be seen in Figure 3-4. The sensor location is marked on the PU foam core. For any sensor mat with discrete sensors, the contact area must be approximated based on the area of the sensor, given by:

$$A_e \approx l_e h_e \quad \text{Eq. 3-24}$$

where l_e is the horizontal distance between the centre of the a FSR element to the adjacent one and h_e is the vertical distance between the centre of the FSR element to an adjacent sensor. (For this specific mat, $l_e = 4$ cm and $h_e = 2l_e$). However, for the outermost FSR sensors elements, the approximate A_e is only approximated for the inner area.

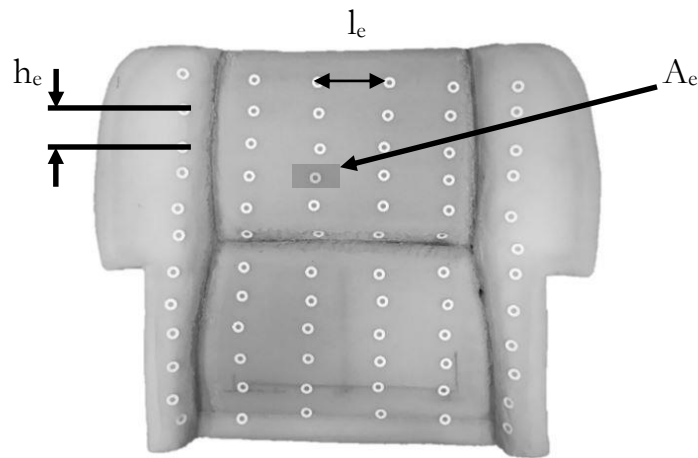


Figure 3-4: Locations of FSR elements on the backrest PU core for ALAS configuration.

3.1.2 Recline Angle and Recline Mechanism

The recline angle for the backrest is studied in this thesis for three reasons. The main reason is to investigate the relationship between recline angle and comfort/discomfort. Secondly, it is necessary to understand the influence of the recline angle on the resultant pressure distribution – since the load is dependent on it. Finally, it is important to define the preferred angle for the specific tasks done while seating (i.e. reading, watching a screen, sleeping, etc.).

A lot of research has been conducted on the relationship between comfort and recline angle. The research on this topic extends from NASA's study on the neutral body position (occasionally referred to as the zero-gravity position) [45] to relationships between shear force and optimal backrest recline angle in relation to seat pan recline angle [46]. Other studies focused on specific seating activities and their corresponding optimal backrest recline angle and the importance of lumbar support with recline angle.

In terms of comfort, NASA developed a configuration of joint angles that lead to the least stress acting on the human body while sitting [45]. This configuration is called zero-gravity position as it is the position that astronaut's body assume when fully relaxed in a microgravity environment (weightless). This position is also used by astronauts during lift off to best distribute the stresses on their bodies due to acceleration. This joint configuration, as seen in Figure 3-5 will become relevant when designing the lower limit for the recline angle.

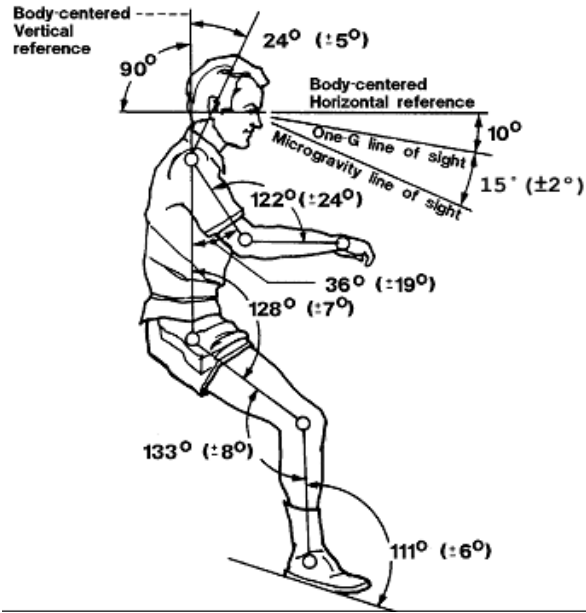


Figure 3-5: Neutral Body Posture[45].

The force of the human body as result of the contact with the seat surface was previously stated to have two components, the normal force and the shear force. This resultant force can be further studied to give an insight into the expected force encountered while seating. The shear force on the backrest is assumed to be zero to keep the model statically determined. The only shear force present on the body is on the seat pan and it is directly influenced by the backrest recline angle and the seat pan recline angle. A link model on the XZ plane can be seen in Figure 3-6 with the force components due to shear and weight on the human body and the reaction forces from the seat at key points. The zero shear force as derived by [46] on the backrest condition is given by:

$$0 = -F_{ht} \cos \beta - F_{vt} \sin \beta \quad \text{Eq. 3-25}$$

where β is the recline angle of the seat pan and the horizontal, F_{ht} , and vertical forces, F_{vt} , at joint 3 are given from the equation of equilibrium. As in [46], the equilibrium equations can be expressed in terms on the gravitational force as a percentage of body weight and these forces can be transferred to the each link's centre of gravity.

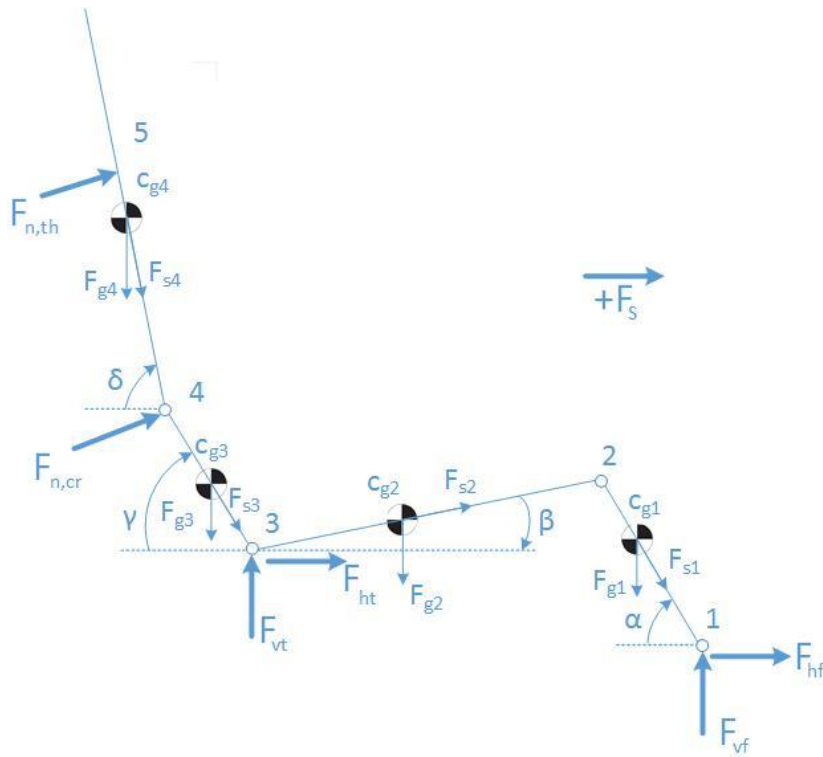


Figure 3-6: Link diagram for the shear and force on the XZ plane.

The actual locations of the centre of gravity for each link (Table 3-3) are calculated in App F from anthropometric data obtained from the study in [45]. The joint equations derived in [46] are as follows:

joint 1:

$$F_{vf} = cg_1 F_{g1} + F_{s1} \sin \alpha \quad \text{Eq. 3-26}$$

$$-F_{hf} = F_{s1} \cos \alpha \quad \text{Eq. 3-27}$$

where F_{g_i} and F_{s_i} are the weight and the shear force respectively at the centre of gravity, cg_i , of link i^{th} and α is the angle between the feet and the ground.

joint 2:

$$0 = F_{s1} \cos \alpha - F_{s2} \cos \beta \quad \text{Eq. 3-28}$$

$$F_{s1}\sin\alpha + F_{s2}\sin\beta = (1 - c_{g1})F_{g1} + c_{g2}F_{g2} \quad \text{Eq. 3-29}$$

joint 3:

$$F_{vt} = F_{s2}\sin\beta + (1 - c_{g2})F_{g2} + (1 - c_{g3})F_{g3} + F_{s3}\sin\gamma \quad \text{Eq. 3-30}$$

$$F_{ht} = F_{s2}\cos\beta - F_{s3}\cos\gamma \quad \text{Eq. 3-31}$$

where γ , is the recline angle of the pelvis.

joint 4:

$$F_{n,cr} = c_{g4}F_{g4}\cos\delta + c_{g3}F_{g3}\cos\delta + F_{s3}\cos(90 - \delta + \gamma) \quad \text{Eq. 3-32}$$

$$0 = F_{g4}\sin\delta + c_{g3}F_{g3}\sin\delta - F_{s3}\cos(90 - \delta + \gamma) \quad \text{Eq. 3-33}$$

where $F_{n,cr}$ is the normal force at the crista iliaca and δ , is the backrest recline angle.

joint 5:

$$F_{n,th} = (1 - c_{g4})F_{g4}\cos\delta \quad \text{Eq. 3-34}$$

where $F_{n,th}$ is the normal force at the thorax. The forces due to each body segment can be calculated from statistical data as in Table 3-4 for the 95th percentile of American men (App F). Alternatively, the force per body segment can actually be measured as discussed in CHAPTER 4 from the mat.

Table 3-3: Distance of cg to joint calculated from anthropometric data.

Link	Joint #	Link length (cm)	cg distance from the lower link (%)
Upper back	2	39.4	39.8
Lumbar	3	29.7	43.4
Thigh	4	65.8	65.8
Leg	5	60.9	17.0*

*Measured value non available. Theoretical value from [46] used instead.

Using the set of equations for equilibrium, along with the assumption that when $\gamma = 0^\circ$ leads to $\delta = 0^\circ$, there exist a linear relationship for the angles as discussed in [46], such that:

$$\gamma = \frac{17}{18} \delta \quad \text{Eq. 3-35}$$

Table 3-4: Weight force per body segment.

Load	Body weight (%)
F_{g1}	11.67
F_{g2}	24.16
F_{g3}	22.36
F_{g4}	41.91

Using Eq. 3-35 into the equation for static equilibrium for F_{vt} and F_{ht} with the zero shear condition, Eq. 3-25, it is possible to find the forces in terms of angles that produce no shear. And as first introduced by [46], the relationship between the recline angles can be expressed as:

$$\beta = -0.61\delta + 57.1^\circ \quad \text{Eq. 3-36}$$

This relationship leads to no shear force (in theory) on the seat pan and is often used in recline mechanism in seat design. This relationship is commonly referred to as Synchronilt, which is a reclining mechanism used to avoid shear on the seat pan and involves reclining the backrest and seat pan at a 1.64:1 ratio. This ratio is often defined as 2:1 in other studies for simplicity, and to make sure there is absolutely no shear on the seat pan as shear forces on the seat surface lead to high level of discomfort and a feeling of sliding out of the seat [2].

Therefore, when the backrest is being reclined, the seat pan should be reclined at a rate of at least 0.82° per degree of backrest recline. In this work, the inclination of the seat should start at the full upright position (during take off and landing) $\gamma = 90^\circ = \delta$ and be able to recline backwards until at least $\alpha = 111^\circ$ - which is the neutral body position.

The activities done while seating also have an effect on the best recline angle. However, most of these angles for each specific task are highly subjective depending on the individual passenger's age and overall health. For example, for watching a screen in an aircraft, the most common backrest recline angle is 100° – 110° and the backrest recline angle for least amount of muscle activity is 120° for most passengers. And for sleeping, a flat surface is preferred. However, some passengers find a flat seat surfaces uncomfortable [2]. Thus, a curvature can be added for the sleeping position to avoid the feeling of sliding out of the seat. This is also possible via the seat surface morphing mechanism presented in this work.

3.1.3 Pressure Distribution Parameter

An additional parameter often used to evaluate sitting comfort is the seat pan distribution percentage given by:

$$BRD\% = \frac{\sum_{i=1}^{e_a} (p_{i,j} - \overline{p_{e_a}})^2}{4e_a(\overline{p_{e_a}})^2} \times 100\% \quad \text{Eq. 3-37}$$

where e_a , is the number of active elements, $p_{i,j}$, is the pressure in the $e_{i,j}$ element, and $\overline{p_{e_a}}$ is the mean of the active elements (SPD was originally defined by Ahmadian et al. [28]). This 'comfort' evaluation parameter is often used combined with peak and average seat pressure.

A similar pressure percentage parameter (backrest distribution percentage) BRD% can be applied to the backrest. The BRD% has the same form of Eq. 3-37 and will be used along with the ideal pressure distribution and biomechanical model in the control method to evaluate the target pressure distribution.

3.2 Seat Pressure Measuring

During operation, the measurement from the pressure mat comes with certain error even after calibration. These errors originate mainly from drift, saturation and hysteresis. The pressure, $p_{i,j}$ for sensor $e_{i,j}$ is given by:

$$p_{i,j} = \frac{f_{i,j}}{A_a} \quad \text{Eq. 3-38}$$

However, each discrete measurement $f_{i,j}$ comes with certain static and dynamic errors. Thus, $p_{i,j}$ can be modified such that the error is accounted for in each sampling reading, such as:

$$p_{i,j} = \frac{f_{i,j}}{A_a} + \Delta p_{i,j} \quad \text{Eq. 3-39}$$

where $\Delta p_{i,j}$ is the error from sensor $e_{i,j}$ composed of the dynamic behaviours only. Firstly, the undesired static behaviour of the sensor (known as drift) which is a result of creep must be compensated for. As in [32], the first derivative of voltage output with time can be used to correct for drift. The following criterion is used to determine if the change in the sensor's resistance is either due to creep or due to an actual change in applied load with time, t :

$$p_{i,j} = \frac{f_{i,j}(t)}{A_a} + \Delta p_{i,j}(t), \quad \text{for } \frac{dV(t)}{dt} \geq 0.2 \text{ V/s} \quad \text{Eq. 3-40 a}$$

and

$$p_{i,j} = \frac{f_{i,j}(t-1)}{A_a} + \Delta p_{i,j}(t-1), \quad \text{for } \frac{dV(t)}{dt} \leq 0.2 \text{ V/s} \quad \text{Eq. 3-41 b}$$

That is to say that for values less than 0.2 V/s, the signal change corresponds to creep behaviour and thus the previous value of p is kept (that is the value of p at time $t-1$). After the static error compensation of the sensor is done, the dynamic error, $\Delta p_{i,j}$, still contains two dynamic

components, saturation and hysteresis. The dynamic factors contributing to the error can be further expanded into its two components:

$$\Delta p_{i,j} = f(G_s(V, I), H_h(V, I)) \quad \text{Eq. 3-42}$$

where G_s , is the saturation of the sensor due to pressure loading and H_h , is the hysteresis effect due to loading history.

Since the compressibility of the polymer in the foil piezoresistive sensors is finite, the conductance of such sensors often exhibits saturation. The typical form of saturation is described by:

$$G_s = \frac{aF}{(b + F)} \quad \text{Eq. 3-43}$$

where a and b are the saturation coefficient of the FSR sensor. However, as discussed before, the voltage output for sensor $e_{i,j}$ is given by:

$$V_e = \frac{V^+}{\left(1 + \frac{R_e}{R_M}\right)} \quad \text{or} \quad V_e = \frac{R_M \cdot V^+}{\left(R_M + \frac{1}{G_s}\right)} \quad \text{Eq. 3-44}$$

where V^+ , is the positive supply voltage, R_M , is the measuring resistor value (Ω), and R_e , is the current electrical resistance value of the FSR sensor $e_{i,j}$. Substituting Eq. 3-44 into Eq. 3-43 gives:

$$V_e = \frac{a \cdot (R_M \cdot V^+ \cdot F)}{(b + F(a \cdot R_M + 1))} \quad \text{Eq. 3-45}$$

The previous equation can only be linear if $F \ll b/(aR_M + 1)$. By inspecting of Eq. 3-45, clearly the larger the resistance of R_M , the smaller the linear range will be. Thus, in order to achieve a linearized form of Eq. 3-45, we should have a negative resistance ($R_M = -1/a$), but this is impractical. If instead an op-amp circuitry with a resistor R_f as the feedback loop is constructed, then it is possible to write:

$$V_e = \frac{R_f \cdot V_s}{\frac{1}{G_s}} = \frac{R_f \cdot V_s \cdot a \cdot F}{(b + F)} \quad \text{Eq. 3-46}$$

or rearranging Eq. 3-46 it can be express in series form as:

$$F_s = c_1 V_i + c_2 V_i^2 + \dots \quad \text{Eq. 3-47}$$

Thus, it is possible to use linear least square method to determine the parameters of c_i , in Eq. 3-47 whereas nonlinear methods are needed to solve Eq. 3-46. For FSR, Zehr's et al. [34] determined the first two terms to be $c_1 = 71.1$ and $c_2 = 91.9$ and they proved to be sufficient. However, even with fitted and corrected data the sensor signal still has problems related to the hysteresis effect.

The magnitude of the error can further be improved by conducting a dynamics test to account for hysteresis. To compensate for hysteresis which considers the dependency of the voltage, V , and a moving integral, I (obtained by summing the products of the voltage output and a linearly increasing factor). By means of multiple regression, a 4th degree polynomial can be obtained in the form of

$$H_h(V, I) = a_0 + a_1 V + a_2 V^2 + a_3 V^3 + a_4 V^4 + a_5 I + a_6 I^2 + a_7 I^3 + a_8 I^4 \quad \text{Eq. 3-48}$$

where the hysteresis coefficients a_i are found experimentally. The researchers in [32] showed that it is possible to change the way the moving integral is calculated and making the force (output) to be a function only of the voltage.

$$H_h = b_0 + b_1 V + b_2 V^2 + b_3 V^3 + b_4 V^4 \quad \text{Eq. 3-49}$$

where b_i are the hysteresis coefficients. With this procedure (excluding the moving integral), the researchers in [32] found a resultant standard error of 1.385. The best performance for reducing hysteresis was found using 0.5 s with linear increasing regression (using Eq. 3-49). Finally, the dynamic error can be written as:

$$\Delta p_{i,j} = \frac{(F_s + H_h)}{A_a} - 2 \frac{f_{i,j}}{A_a} \quad \text{Eq. 3-50}$$

The presented methods of compensating for the sensor's signal will be used along with calibration to improve the response of the sensor, this will be discussed in the next chapter.

3.3 Mathematical Deformation and Deflection Models

The study of the physical interaction between two solid bodies in contact is of great importance for several practical applications. Presently, there exists no theory which can be called “the robust method” for all different types of contact simulations. This is especially true for problems with nonlinearities in their system. Even the simplest types of interactions deal with contact, friction and boundary value problems that make the study of such problems difficult to analyze.

For this study, the contact behaviour resulting from the interaction between the human body and the seat is of great importance to evaluate comfort objectively. The contact behaviour model must be understood to approximate the effect on the seat's curvature from the pressure distribution. The actuator deflection in the control system also necessitates the model to decentralize the weight of the passenger in order to decrease discomfort.

3.3.1 Hyperelastic Modeling

Materials such as rubbers, foams and most biological materials (such as muscle and skin) tend to exhibit nonlinear stress-strain behaviour when loaded. The accuracy of the theoretical foam deformation depends on the selection of the right hyperelastic material model. Materials such as PU that can achieve large deformations are best modeled with Ogden's large deformation isotropic elasticity model. The criterion to determine the fidelity of the model depends on the model's ability to best fit experimental data of the strain energy function. The Ogden hyperelastic material model, Eq. 3-51, describes the non-linear stress-strain behaviour of complex materials, such as rubbers, polymers and

some biological tissues. The derivation of the Ogden's equation is quite involved and thus it will be excluded from the present work but it can be found in [37].

$$\psi = \sum_{i=1}^N \frac{\mu_i}{\alpha_i} (\lambda_1^{\alpha_i} + \lambda_2^{\alpha_i} + \lambda_3^{\alpha_i} - 3) \quad \text{Eq. 3-51}$$

where ψ , is the strain-energy, λ , are the principal stretches used as independent variables (when the material is incompressible the constrain $\lambda_1 \lambda_2 \lambda_3 = 1$) and the pair (α, μ) are the material parameters obtained from experimental data. Principal stretches are relative to a given reference configuration, S^0 . If α has a value greater than 2, the material's stiffness will increase with increasing strain. And if α has a value less than 2, the material will soften with increasing strain.

For this reason, material tests must be carried out. For this work, simple uniaxial compression tests were carried out for each of the materials to determine their coefficients, and were fitted with Ogden's model. Pure shear tests were not carried out since as discussed in the previous section, the backrest experience negligible shear, and with Synchrotilt, both the backrest and seat pan are intended to have no shear. Lastly, the pressure sensors (FSRs) used to measure the pressure distribution do not respond to shear loads. Thus, it is not essential to know the shear behaviour of the material for this case. However, knowing the shear behaviour can indeed improve the model fitting.

As previously noted, PU foams in particular are network-forming cell materials with low stiffness, low poisson's ratio, low density and has the ability to absorb strain energy and slowly recover to their S^0 . PU foams typically have three distinct phases in the strain deformations:

- 1) Below 5% of their complete deformation, their deflection is caused due to bending of the foam's cells.
- 2) Large deformation is encounter during the second phase due to buckling of the cell wall structure of the foam.

- 3) In the last stage of deformation, the foam shows substantial increase in rigidity due to compression in the deformed cell structures.

Additionally, polymeric foams, such as PU have certain properties:

- 1) Their deformation is close to reversible and show little creep.
- 2) Unlike other hyperelastic materials, foams show compressibility.
- 3) Their behavior under load is complicated and their response in compression is significantly different to the one for tension due to their cell structure.
- 4) Foams with random cell structures are considered isotropic.

On the other hand, muscle, skin and adipose tissues are practically incompressible. Eq. 3-51 can be modified for compressible materials, such as PU foams.

For the seat cushion's material, PU foam, the "Ogden Compressible Foam model" such as in [41] could be used for the analysis if the previous model does not fit well the experimental data. For PU foams, the stress strain curve can be seen to have one inflection point. This model reliably accounts for materials that undergo large deformations (compression) and significant volume change with relatively low applied stress with inclusion of Poisson's ratio as well:

$$\psi = \frac{2\mu}{\alpha^2} \left(\lambda_1^\alpha + \lambda_2^\alpha + \lambda_3^\alpha - 3 + \frac{1}{\beta} (J^{-\alpha\beta} - 1) \right) \quad \text{Eq. 3-52}$$

where

$$\beta = \frac{\nu}{(1 - 2\nu)} \quad \text{Eq. 3-53}$$

and ν being the Poisson's ratio.

Ogden's model will be used in HyperFit[®] 2.101 software to identify the model parameters of the hyperelastic constitutive models based on nonlinear regression and optimization methods from the experimental data. The models for the strain energy density function will later be used in the control system to predict the deflection of the foam and the required actuation as discussed in the next section.

CHAPTER 4 Seat Sensing Development

4.1 Design Approach

The materials under study, except for bone tissue, fall under the classification of hyperelastic materials. As mentioned before, human tissues such as muscle, skin, adipose tissue and along with most biological materials are best modeled as hyperelastic materials [39], [47]. This is also true for the materials comprising the seat components that are in contact with the user. The core (cushioning) material in both the seat pan and the backrest are made out of a high resilience polyurethane (PU) foam. PU foam is an open-cell, flexible foam with higher random cell structure that adds support to its structure.

This study will utilize methodologies based on strain-energy function models and biomechanical body models to predict the shape of the back of the torso and lumbar spine flexion. This models will be used in conjunction with the contact mechanics for the PU foam to predict the deflection and force relationship.

4.1.1 Requirements

The requirement for the design are based on the following criteria:

I. Ideal pressure distribution according to the body map:

The contact pressure should be analyzed as pressure distributions instead of the individual pressure readings. The ideal pressure distribution for the backrest should be divided into distinct regions where the pressure dispersion ratio of the total back load on the seat is measured in percentage as suggested by the studies of Mergl [13], Zenk [12] and Hartung[10]. This ratio indicated by each zone shows the split load between individual body areas. This ideal model is shown in Figure 4-1 a).

Ideally, each section (marked with different colour and line pattern) should be controlled independently for best results. However, this results in a complex system with too many parameters to control. For our simplified model, only the main four regions of interest are analyzed (note that $A_3=A_4$), while only the lumbar region is actuated as seen in Figure 4-1b) and the side regions are monitored with the sole purpose of obtaining the full pressure distribution. This distribution ratio will be used as a target value to determine the optimal pressure distribution.

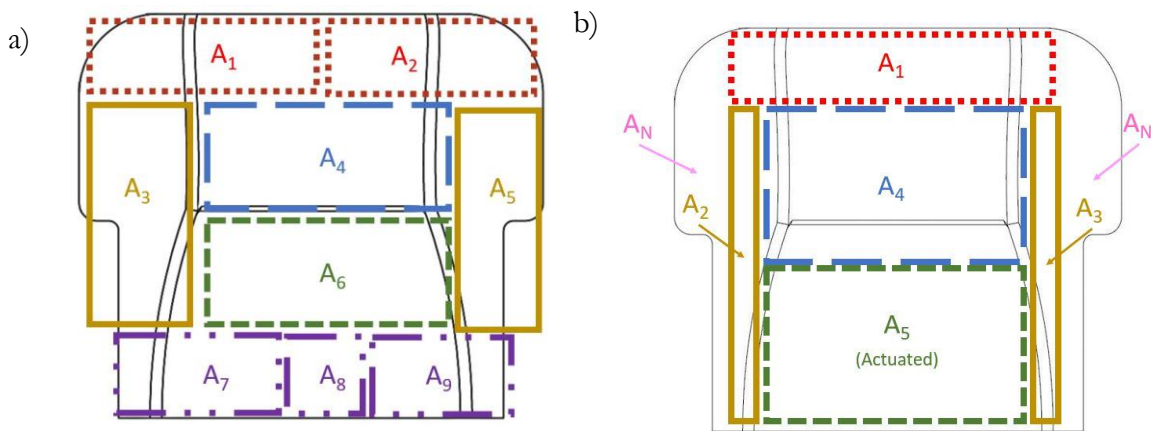


Figure 4-1: Backrest regions for Ideal pressure dispersion ratio a) optimal b) actual

II. Biomechanical Comfort:

A biomechanical model is needed in order to reduce the complexity of the controller when choosing the reference value for the ideal pressure distribution. The reference value from the first requirement can be further refined by including a biomechanical model. The biomechanical model should also consider the joint angles and resultant force.

III. Peak Pressure Elimination:

The main reason for physical discomfort experienced by seated individuals is caused by *ischemia*. Ischemia is the result of inadequate blood flow to the tissue when the pressure inside the tissue exceeds the opening pressure of the capillaries in that region. Closure of the capillaries causes pain due to accumulation of metabolites, mainly lactic acid which is a byproduct of anaerobic

metabolism. Other pain-inducing chemicals are also released from cells damaged by *hypoxia* (oxygen deficiency in a biotic environment). Ischemia occurs when a constant pressure is applied to the tissue exceeds 8.8 kPa. The actual pressure that closes the capillaries is 4.3 kPa. Tissue ischemia is also known to be produced by excess shear on the skin in addition to direct compression. Excessive shear on the skin is often caused by large deformation of the supporting foam material (“hammock” effect) [48]. Thus, it can be concluded that there exists a threshold value at which discomfort is not present. The contact analysis problem will use these pressures as a criterion for the design. Any pressure exceeding these values will be considered inadequate if present for a prolonged period of time (< 30 min) and 20 kPa for short term (> 30 min). Also, shear will be avoided by using the Synchronilt mechanism.

IV. Reducing the Backrest Distribution Percentage (BRD%):

The BRD%, which is the most popular statistical parameter used to define discomfort in seats will be used as another critical value for the analysis. The BRD% (SPD% for the seat pan) will be calculated in the initial contact state and will be observed as the system approaches the final contact state, %P. A reduction in BRD% must be achieved by changing the pressure in the lumbar support. However, it is possible to overshoot the optimal BRD% value which lies between the ideal pressure distribution range. In such case, the controller must use the optimal BRD% as the new target value.

4.2 Development of Surface Pressure Mat

For this study, a pressure mat was developed to allow real time surface pressure data gathering from the occupant when seated. The sensor element selected was the Interlink’s FSR Standard 402. As described in §2.2.4, an FSR works as an open circuit when no load is applied and when a load is applied to its active area ($A_a=1.69\times 10^{-4}$ m²), the substrate deforms causing a decrease in resistance. The change in resistance can be utilized to calculate the load applied to the FSR element. The typical configuration for this passive sensor is in a voltage divider as shown in Figure 4-2. The measuring

resistance, R_M , is selected to optimize the force sensitivity range for this application (Figure A-0-6, Appendix D). Taking into consideration the expected loads for the pressure mat, R_M should be set to 10 k Ω . This configuration creates an increase in the output voltage for each sensor element, V_e , if a load is applied, as given in the following formula:

$$V_e = \left(\frac{R_M}{R_M + R_e} \right) V^+ \quad \text{Eq. 4-1}$$

where R_e , is the resistance of the FSR element in Ω . And as discussed in §3.2, Eq. 3-46 can be used to linearize the response of the GSR.

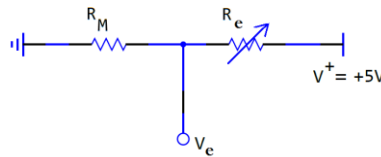


Figure 4-2: FSR's voltage divider circuitry.

Table 4-1 shows the basic characteristics of the selected FSR 402. The sensor mat contains a total of 72 sensing elements arranged in an evenly distributed pattern (6 by 12). The arrangement of the sensors focuses only on the 4 different areas of the backrest (areas: 1, 2 and 4, 6. See Figure 4-1)

Table 4-1: FSR 402 Characteristics [26].

Feature	Value	Units
Force Range	0.1 – 98.1	[N]
Pressure Range	0-1.2	[MPa]
Force Resolution	<0.5	% full scale
Saturation Pressure*	>0.689	[MPa]
Active Area	1.69×10^{-4}	[m ²]
Stand-off Resistance	>1	[M Ω]
Life Time	> 10^6	cycles
Response Time	1-2	[ms]
Max Current	1	mA/cm ²

*Saturation on the FSR402 is function of Pressure. Typically observed in the range 0.69-1.2 MPa.

4.2.1 Preconditioning and Normalization of the Sensor Mat

Ideally, before using the sensor mat, preconditioning of the FSR elements must be performed every single time. This increases the repeatability of the measurements and reduces drift and hysteresis. Preconditioning is done by loading the FSR sensing elements with a slightly higher load than the expected operational load, but below the maximum load, F_{\max} . During real operation (i.e. after the seat has been installed in the aircraft) it becomes impractical to precondition the sensor mat before every use. Thus, it is only recommended to perform the preconditioning as a maintenance procedure. For this reason, preconditioning will be used only before the initial calibration procedure in §4.2.2 and will be disregarded in this work in CHAPTER 6 with the purpose of obtaining more realistic values to those expected during real operation. However, since drift and hysteresis will be accounted for in the model as in §3.2, the influence of preconditioning can be considered negligible.

Before the calibration procedure and operation, the pressure mat must be normalized. Normalization must be done in order to compensate for the differences in sensitivity of each sensing element due to usage, manufacturing variations and material irregularities. Normalization is done by applying a uniform load, F_n , over the mat and determining an appropriate gain, $N_{i,j}$, for each of the FSR sensing elements, $e_{i,j}$. If the applied uniform load, F_n is known, then each of the gains can be calculated as:

$$N_{i,j} = \frac{f_{i,j}}{F_n} \quad \text{Eq. 4-2}$$

where $f_{i,j}$, is the FSR element load output for sensor element $e_{i,j}$. In most cases, specially if the normalization needs to be automatized, it is inconvenient to know the uniform load, F_n . As long as the applied normalizing load, $F_n < F_{\max}$, an alternative and more practical form to calculate the gain is given by:

$$N_{i,j} = \frac{f_{i,j}}{\bar{f}} \quad \text{Eq. 4-3}$$

where \bar{f} (Eq. 4-4), is the average output from the sensor mat applied to all the elements. This is done because the actual response is not known, and the average is taken as the true response, from which all sensor's responses are determined.

$$\bar{f} = \frac{\sum_{i=1}^n \sum_{j=1}^m f_{i,j}}{mn} \quad \text{Eq. 4-4}$$

As seen in Eq. 4-2 and Eq. 4-3, $N_{i,j}$ is proportional to the magnitude of each element output $f_{i,j}$, which is related to the sensitivity of the element. Using Eq. 4-3, the gains were calculated for all 72 sensors for a three-point normalization. The values range for $N_{i,j}$ are shown in Figure 4-3a.

After the gains for the respective data points are obtained, a modified *nearest neighbour* interpolation method [49] for approximation of the function of $N_{i,j}(F_n)$ at F_n is introduced. This interpolation method results in a series of plateaus, which can be thought of as zero-order polynomials. The modified method uses weighing coefficients to established the boundaries of the intermediate interpolating functions. The reallocation of the boundaries in turn provides a better fit to the data. This method can be expanded to r data points wich results in $r-1$ intermediate functions. With a larger number of data points, the accuracy can be significantly improved. The size of r is determined based on the expected load on the sensor and the discontinuities in the sensor's output. And the weighting coefficients can be obtained based on the obseved behaviour of the sensors. Assuming a full range of the sensor span is needed and with the data provided by the manufacturer, then $r \geq 10$ for optimal results. However, for $r \geq 10$ a piecewise cubic Hermite interpolation tends to be a better approximation than the modified nearest neigbout approximation. A piecewise cubic Hermite interpolation avoids overshooting the data points and has less oscilations as it can sometimes happen for simple cubic splines. A sample $N_{i,j}$ value set for the modified nearest neighbour interpolation

method is shown in Figure 4-3b). The selected sensor gain shown in the figure below was arbitrarily selected from sensor 33 for illustration purposes only.

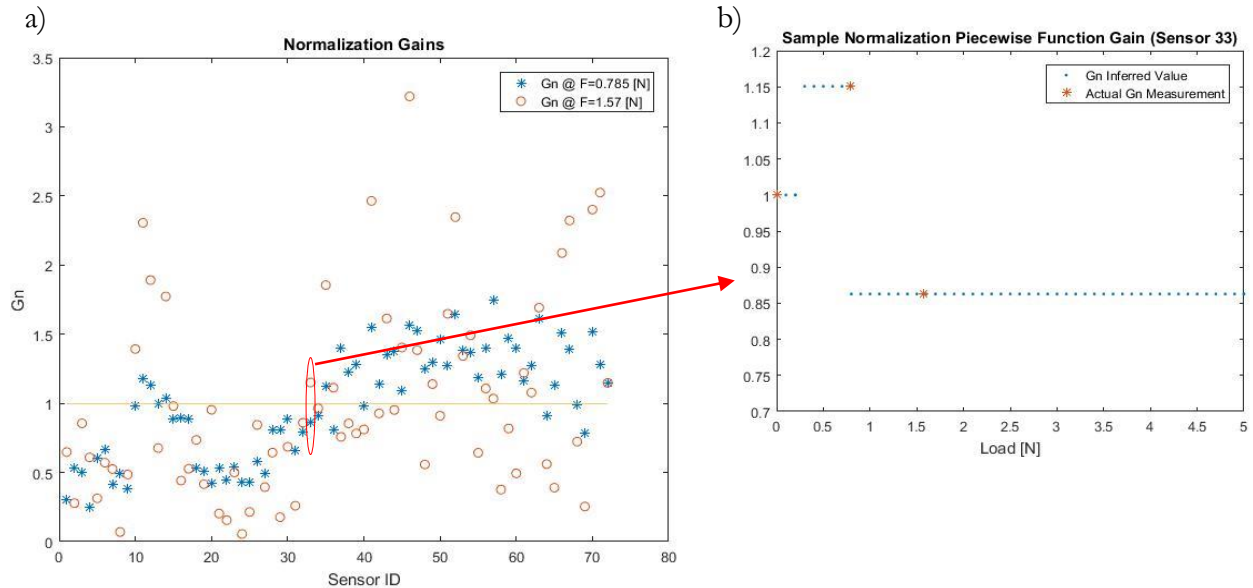


Figure 4-3: a) Normalization gains b) Normalization gains piecewise function (SensorID:33)

As seen in Figure 4-4, a 3-point normalization is applied to the sensor mat. The discrepancies between the sensors are significantly reduced and thus further improving the accuracy of the surface pressure data. If the number of normalization points is increased for the normalization the discrepancies between sensors decreases and approaches zero when the number of sample points equals the number of calibration points (or better, the continuous loading profile). Ultimately, the normalization procedure can be thought of as an efficient technique to compensate for the individual sensing element's sensitivity differences. Instead of calibrating all 72 sensors on the mat with 10 calibrations points and calibration loading profiles, only a small number of sample points are required.

Figure 4-5, shows the effectiveness of the normalization procedure to reduce the percentage deviation. From the figure, the ranges for the calibration curves are determined in order to keep the measurement error within the allowable limit.

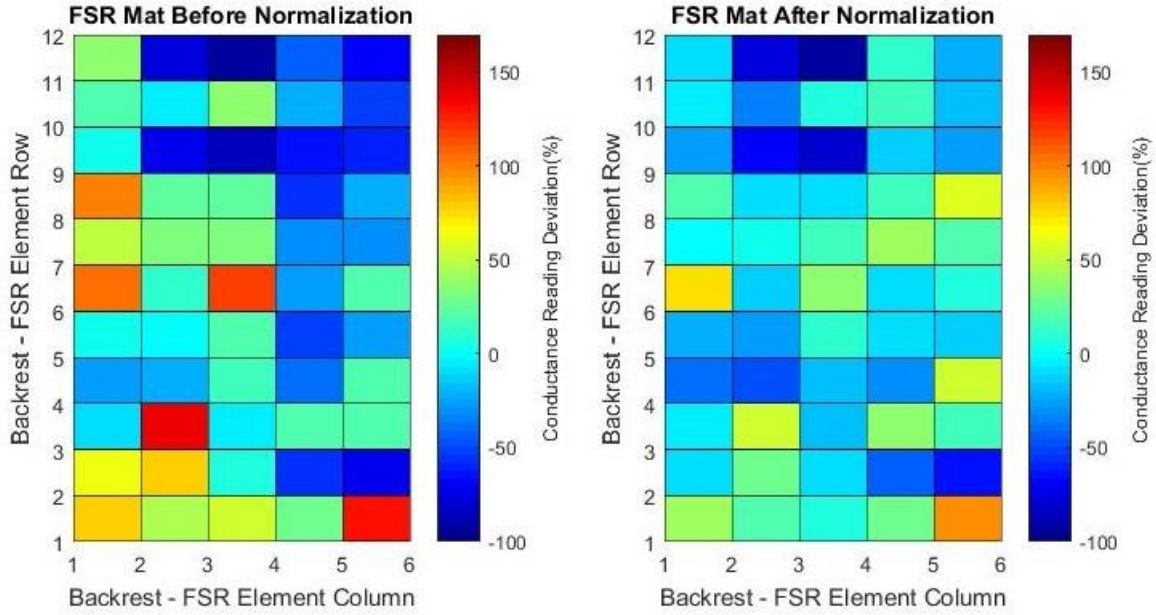


Figure 4-4: Normalization result on the mat under $F=100g$

By analyzing the normalized deviation percentage of the FSR mat, it is possible to observe that the calibration can not be the same for all FSR element even after normalization. At this point there are 2 possible options to improve the FSR output, 1) increase the number of normalization points or 2) create different calibration equations for the different ranges of the FSR elements. The latter option is the most efficient and less time consuming. For this reason, the FSR mat will be divided into 7 calibration sections.

By normalizing the pressure mat instead of calibrating the sensor individually significant effort is saved. For example, for a three-point normalization of a mat containing 72 sensors with 7 incremental calibration loads, ($r=3$, $mn=72$ and $q=7$) the number of calibrations needed, v_N , are only about half of those if full calibration is done on each sensor.

$$\frac{v_N}{v} = \frac{r(q + mn)}{q \cdot mn} = \frac{237}{504} = 0.47 \quad \text{Eq. 4-5}$$

Each section will have a corresponding calibration equation, F_1 to F_7 (Figure 4-6). The ranges are selected to keep a constant percentage deviation range for all sensors. The percentage deviation is

set to be $\leq \pm 12.5\%$, which is close to the error found in similar commercial pressure mats (approximately ± 5 to $\pm 20\%$). The calibration equations for each sensor is selected based on closest calibration curve of the percentage deviation of each sensor. The calibration curves, that will be discussed in the next section are assigned to each of the sensors.

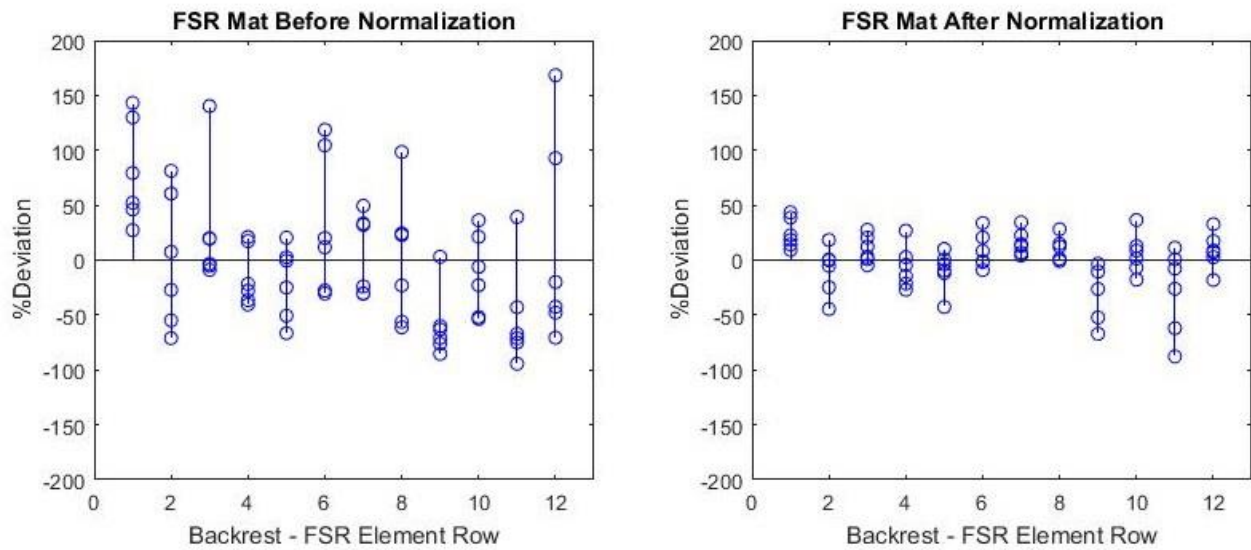


Figure 4-5: Deviation Percentage before (right) and after (left) normalization.

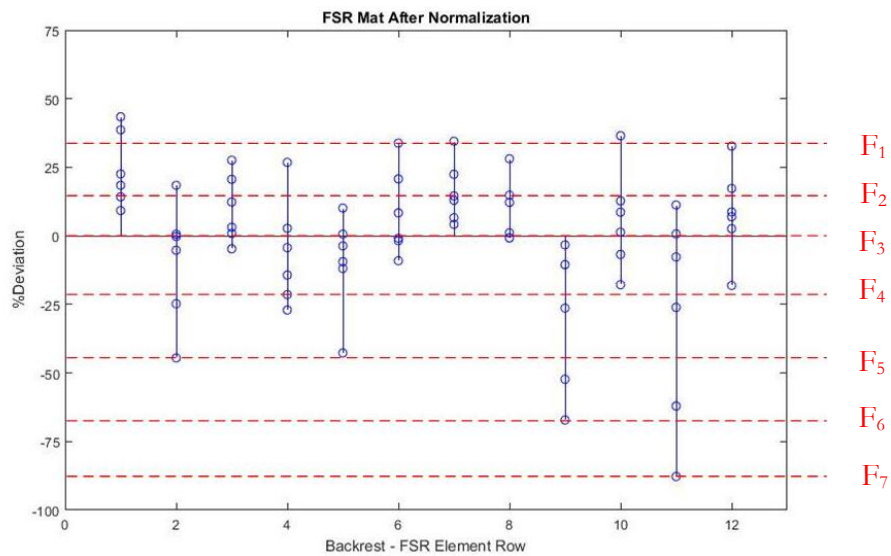


Figure 4-6: FSR mat percentage deviation after normalization.

4.2.2 Calibration Procedure

Part of the design process of a sensor system requires proper calibration and compensation. The initial part of this calibration process is intended to evaluate the basic response of the FSR sensors and observe the drift characteristics of the FSR sensor and repeatability. The calibration for the pressure mat was conducted in two different situations, 1) static load calibration on a solid surface using individual weights, and 2) dynamic calibration on a hyperplastic surface with a linear actuator with a specific loading profile with a reference FSR sensor (solid calibration).

4.2.2.1 Static Calibration

The static calibration was performed on a solid surface only. The method for the static calibration was performed by placing individual weights of increasing mass (10 g – 1.0 kg). The seven resultant calibration equations have the form of Eq. 4-6 and as shown for a sample sensor in Figure 4-7.

$$F = a \cdot R_e^b, \quad b < 0 \quad \text{Eq. 4-6}$$

where R_e is the resistance of the e_{ij} FSR element

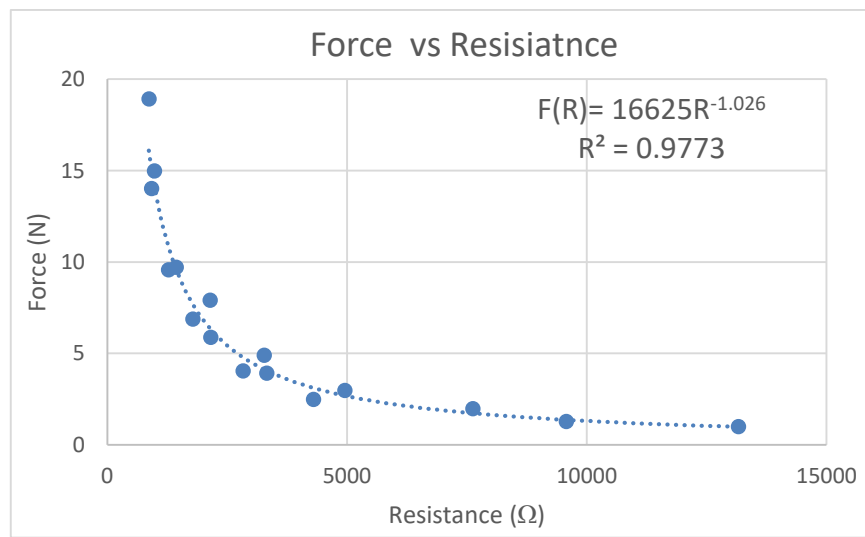


Figure 4-7: FSR output - Force vs Resistance for sample Sensor.

Note that the coefficient of determination, R^2 , is an indicator of how well the data fits the mathematical model chosen for the fit ($R^2 = 1$ signifies that the model explains 100% of the variability of the data).

Since the output of the FSR is a voltage (via voltage divider), V_e , that results from the change in resistance of the FSR, the output is a power function. However, the output can be linearized alternatively by realizing that instead of measuring the resistance it is possible to measure its inverse. In other words, by measuring the electrical conductance, G , ($1/\Omega$) of the FSR active area as a result of the load applied (force, F). The calibration equation can be simplified as:

$$F = a_s G \tag{Eq. 4-7}$$

where

$$G = \frac{1}{R_e} = \frac{1}{a \cdot F^b} \tag{Eq. 4-8}$$

Thus, the seven calibration equation can now be expressed as linear equations with zero set as the y-intercept. It is important to mention that the assumption of a linear response is only valid for loads below 12 N. This is because R_M was selected to be 10 k Ω , which results in an almost linear response for loads between 0 N to 12.5 N. For larger loads, the response will be non-linear due to saturation in the sensor. However, loads higher than 12.5 N (~98.4 kPa) will not be encountered for this specific operation. Note that, Eq. 3-47 and Eq. 3-48 should be used along with Eq. 4-8 to reduce saturation and hysteresis.

The simple set up can be seen in Figure 4-9 along with the data obtained in this calibration (Figure 4-8). The corresponding coefficients for the seven calibration linear equations were obtained via linear least square regression and shown in

Table 4-2. The limitation for this calibration process is the large increments between loads (in the form of mass) applied to the sensor and the extensive manual work needed to calibrate all the individual sensors under different loading conditions.

Furthermore, static calibration is virtually impractical in hyperelastic materials where the deformation is large enough to interfere with proper placement of the individual weights. The procedure and results of the solid surface calibration were compared to the manufacturer’s results in their datasheet [26] and to other research for the calibration of this type of sensors[50], [51]. Similar results were obtained from this experiment. Of more practical use, a calibration method for FSR sensors was developed in this thesis for hyperelastic materials as followed in the next section.

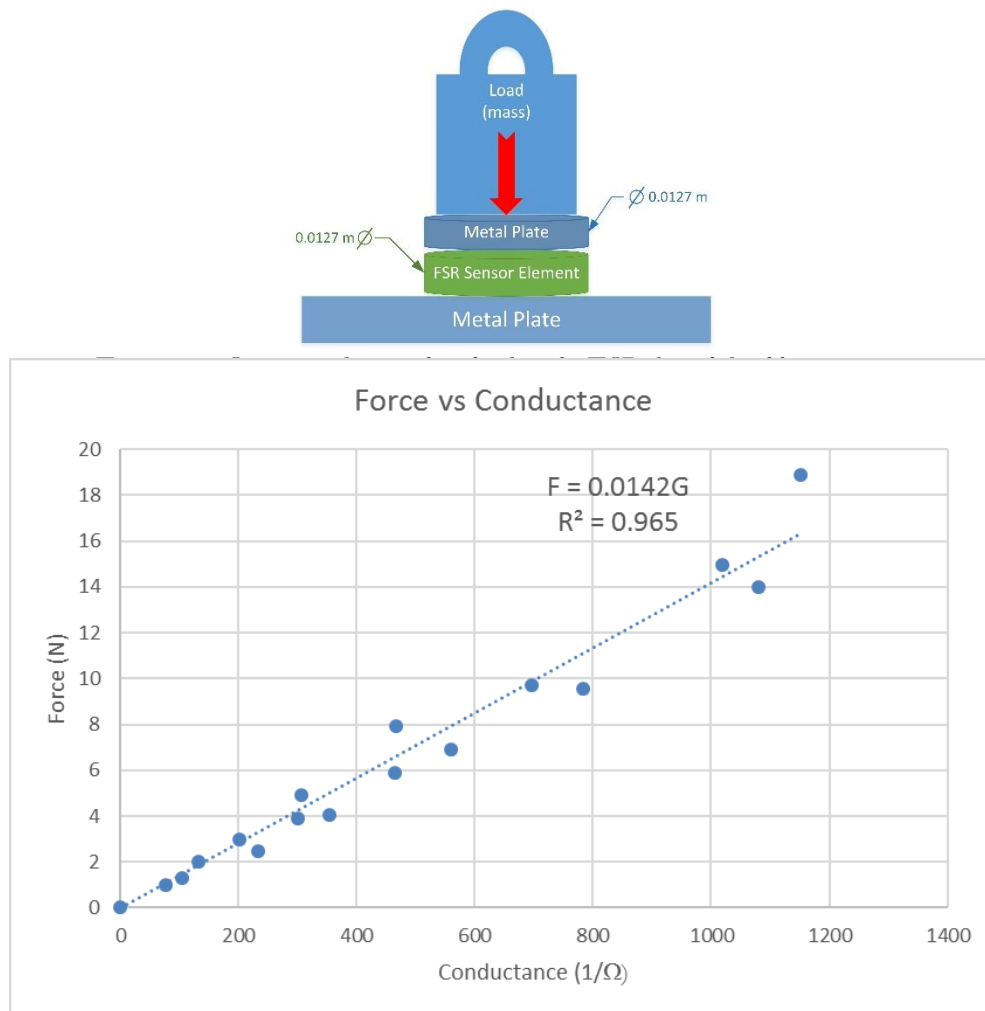


Figure 4-8: FSR output - Force vs Conductance for sample sensor.

Table 4-2: Solid Static Calibration Coefficients.

Calibration Curve	Sensor ID	Calibration Coefficient (a_s)	R^2
F ₁	61	0.0222	0.9556
F ₂	38	0.0340	0.964
F ₃	55	0.0198	0.9228
F ₄	58	0.0199	0.9871
F ₅	29	0.0193	0.9794
F ₆	65	0.0214	0.9657
F ₇	64	0.9315	0.9315

4.2.2.2 Dynamic Calibration

The second method of the calibration process required the construction of a more involved calibration set up as shown in Figure 4-10. This calibration was developed mainly to calibrate against hyperelastic materials such as the backrest foam core and the human tissue analogue. This is because it is impractical to statically calibrate hyperelastic surfaces due to their large deformation.

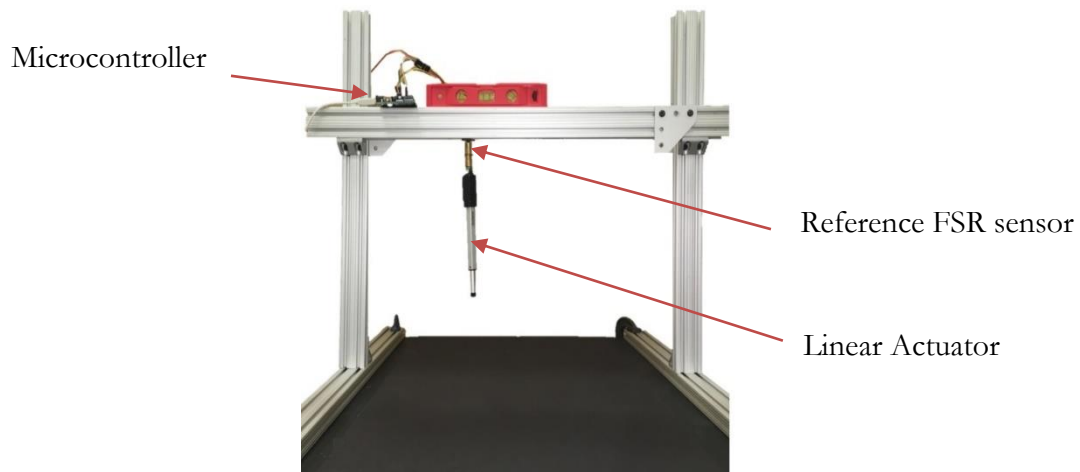


Figure 4-10: Hyperelastic calibration apparatus.

The backrest cushion system (containing the PU foam core, the lumbar air spring system, the sensor mat layer and the seat cover) was placed under the calibration apparatus as seen in Figure 4-11.

The linear actuator was aligned manually for each of the 7 calibration sensors (Sensors ID: 61, 38, 55, 58, 29, 65, 64). In between the backrest cushion system and the linear actuator, a synthetic tissue simulant (a standard 20% ballistic gel) was added. Adding the tissue simulant was done in order to accurately represent the force distribution applied on the seat when it comes into contact with the passenger. The standard 20% ballistic gel (250 Bloom) was made from 1 part of 290 Bloom (85% protein) gelatin powder dissolved in 5.8 parts of warm water. As recommended in [52], when dissolving the ballistic gel powder, the water was kept below 40° C in order to avoid weakening of the gel's strength and viscosity. The tissue analogue was chilled and it was used at 10° C to better represent the mechanical properties of human tissue. The tissue analogue had the same surface area as the sensor's active area and a height, h_b , of 0.5".

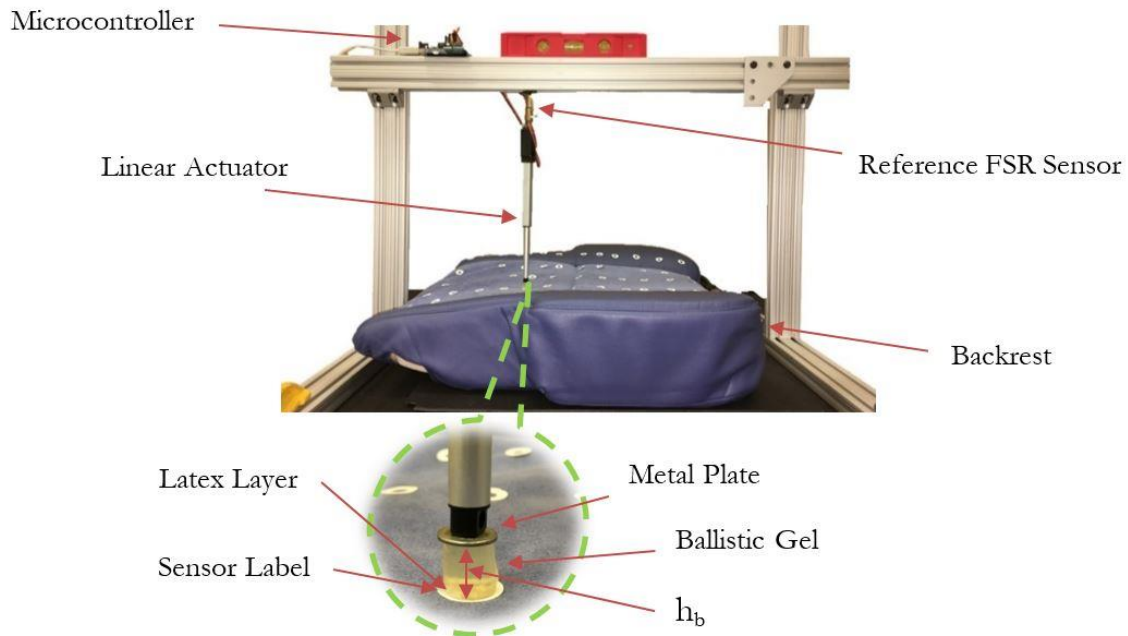


Figure 4-11: Hyperelastic calibration setup

Ballistic gel closely resembles the density and viscosity of human muscle tissue and has been extensively validated, specially for projectile retardation in muscle such as in [53]. It is important to note that a better human tissue simulant can be achieved by substituting the ballistic gel with an *in vitro* porcine tissue specimen. Porcine tissue is a better tissue analogue since it displays anatomical and

physiological similarities to human's tissue and it is readily available compared to synthetic alternatives (ballistic gel, etc.) [54]. The anatomical complexity of the human back can be best represented by the use of porcine tissue. Both organism have hairless bodies, a thick layer of subcutaneous adipose tissue and similar skin properties. And unlike the ballistic gel, the in vitro pork tissue can contain bone, skin and ligaments which mimics the actual repose better than ballistic gel. However, the use of animal tissue models comes with ethical implications [53] and thus it was avoided in this work.

During the hyperelastic calibration process, the location of each individual sensor element was temporally marked on the seat cover with white circular labels to facilitate finding the sensor. The test was performed semi-automatically with increasing continuous load from the linear actuator. The tissue analogue located on the end-effector of the linear actuator was separated with a layer of latex to prevent staining of the seat cover. The layer of latex should not affect the response significantly as it is also a hyperelastic material and only a very thin layer was used.

The load on the calibrated reference sensor was recorded along with the load on the cushion and position of the linear actuator's end effector. The load data was used for the calibration of the sensors and the displacement-force data was used in the hyperelastic model. Similar procedures were followed to test the displacement-force characteristic of the tissue analogue (the ballistic gel) and the foam by themselves.

The sample calibration curve for the hyperelastic case can be seen in Figure 4-12. Cubic polynomial regression was used to best fit the data and has the form of Eq. 4-9. The coefficients for the hyperelastic calibration curves are shown in

Table 4-3.

$$F_h = a_h + b_h x + c_h x^2 + d_h x^3 \quad \text{Eq. 4-9}$$

For the y intercept, a_h equals to zero. This calibration procedure was followed for both scenarios, with and without the ballistic gel. The results were compare to observe if there is an effect of applying the force with a solid disk and with a hyperelastic material resembling the mechanical properties of the human tissue. This important step has been generally ignored in all surface pressure measuring researches covered in CHAPTER 2.

When the same procedure for hyperelastic was conducted with the ballistic in place to simulate the contribution of the deflection of the human body, the resultant function significantly changed as seen in Figure 4-13. The higher non-linearity for the response in Figure 4-12 can be attributed to the larger deformation of the PU foam, which is typical of this material. For the ballistic gel and foam set-up, the contact area of the force stayed constant, as there was a slighter deformation of the ballistic gel on the contact surface.

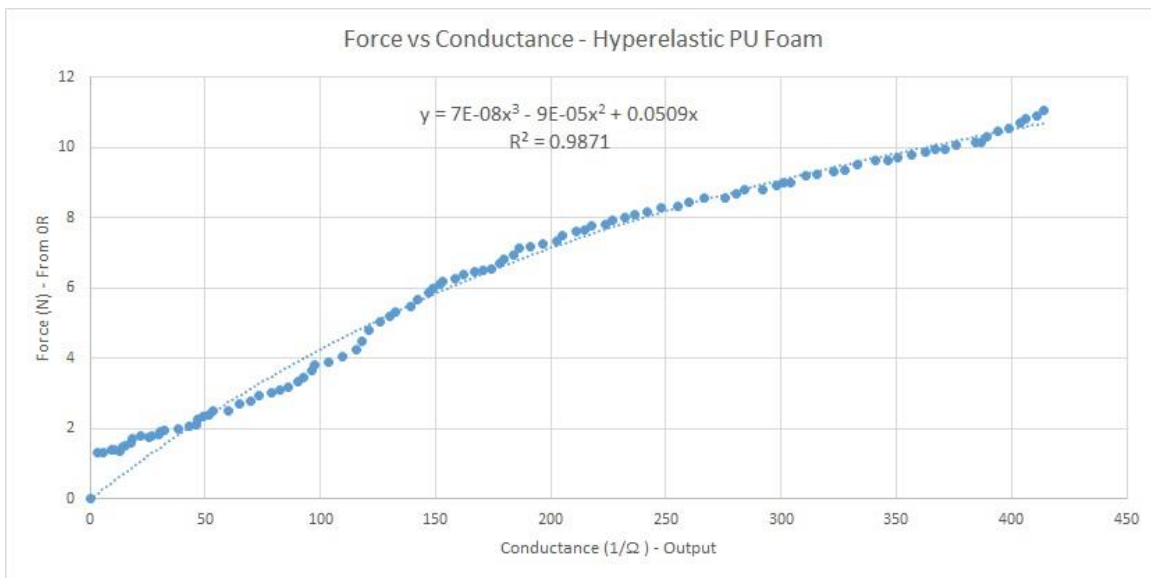


Figure 4-12: FSR output - Force vs Conductance for sample sensor.

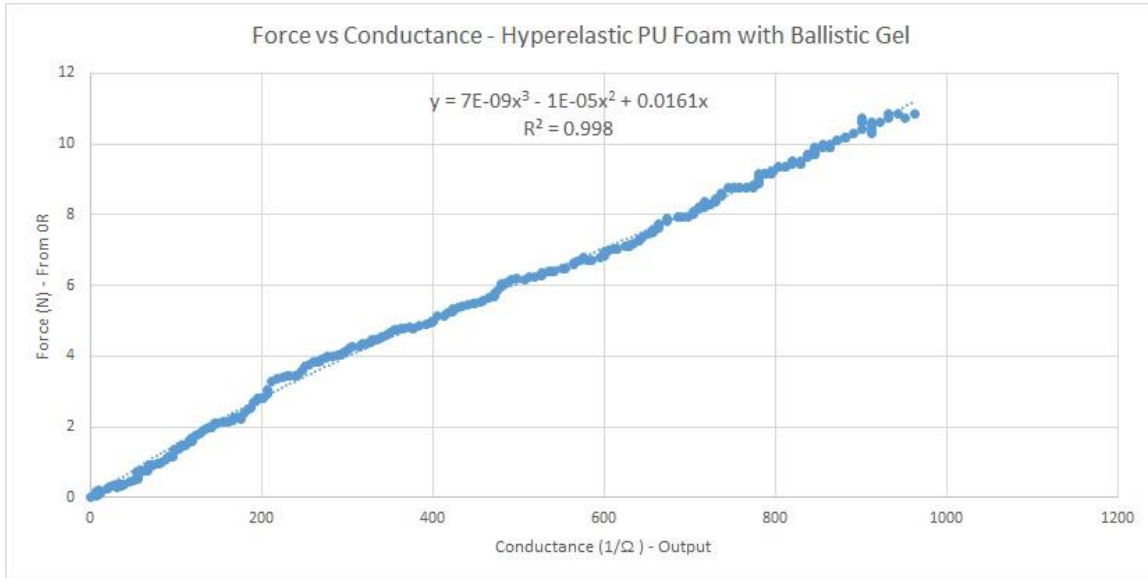


Figure 4-13: FSR output - Force vs Conductance for sample sensor with ballistic gel.

Table 4-3: Hyperelastic Calibration Coefficients for PU Core.

Calibration Curve	Sensor ID	Calibration Coefficient				R ²
		a _h	b _h	c _h	d _h	
F _{1,h}	61	0	2.73E-02	-4.91E-05	7.99E-08	0.997
F _{2,h}	38	0	5.07E-02	-9.79E-05	1.04E-07	0.9903
F _{3,h}	55	0	5.03E-02	-8.93E-05	7.57E-08	0.9970
F _{4,h}	58	0	4.27E-02	1.96E-05	-6.66E-08	0.9876
F _{5,h}	29	0	4.99E-02	-4.34E-06	-1.61E-08	0.9975
F _{6,h}	25	0	8.61E-02	-1.74E-04	1.62E-07	0.9649
F _{7,h}	64	0	4.53E-02	-9.68E-05	1.61E-07	0.9911

Table 4-4: Hyperelastic Calibration Coefficients for PU Core and Ballistic Gel.

Calibration Curve	Sensor ID	Calibration Coefficient				R ²
		a _{hb}	b _{hb}	c _{hb}	d _{hb}	
F _{1,hb}	61	0	3.14E-02	-6.79E-05	6.50E-08	0.9674
F _{2,hb}	38	0	1.62E-02	-4.29E-06	8.64E-09	0.9940
F _{3,hb}	55	0	2.36E-02	-1.57E-05	9.29E-09	0.9979
F _{4,hb}	58	0	2.48E-02	-3.37E-05	1.98E-08	0.9931
F _{5,hb}	29	0	3.38E-02	8.99E-06	-3.62E-08	0.9964
F _{6,hb}	25	0	5.83E-02	-1.24E-04	1.32E-07	0.9782
F _{7,hb}	64	0	3.71E-02	-7.58E-05	6.02E-08	0.9600

The hyperelastic calibration with the ballistic gel method will be used for all sensors on the seat's backrest since it represents a more accurate measurement for this specific application. Each sensor will use one of the seven calibration curves. The curve used for each sensor will be selected so that the sensors' percentage deviation (after normalization) is minimized, that is:

$$F_{i,h} = F_{j,h} \{j | \bigwedge_{j=1}^7 |D_i - D_j|\} \quad \text{Eq. 4-10}$$

The corresponding hyperelastic calibration curves for each sensor is summarized below in Table 4-5.

Table 4-6 shows the corresponding locations of the sensors in the pressure mat. Using the method discussed in this section along with normalization procedure, it is possible to obtain an average error of $\pm 3.92\%$ and a maximum error of $\pm 10.29\%$. The maximum error is fairly comparable to commercial pressure mats ($\pm 5\%$ to $\pm 20\%$, $\pm 10\%$ being the average). This improvement represents the efficiency of the methods used to compensate and calibrate the FSR sensor mat. Without the required accuracy and repeatability of the sensor mat, it is not possible to design a control system. This is the reason that special attention was paid to this section of this thesis.

Table 4-5: Corresponding Calibration Curves, F_b , for Each Sensor.

		<i>Sensor Row (m)</i>											
		I	II	III	IV	V	VI	VII	VIII	IX	X	XI	XII
<i>Sensor Column (n)</i>	VI	F2	F3	F3	F4	F3	F1	F3	F2	F3	F3	F3	F4
	V	F2	F2	F1	F4	F4	F3	F3	F3	F5	F4	F6	F2
	IV	F2	F3	F3	F3	F2	F2	F2	F3	F6	F2	F7	F1
	III	F2	F4	F2	F4	F3	F3	F2	F4	F3	F2	F2	F3
	II	F1	F5	F2	F1	F3	F2	F2	F1	F3	F3	F3	F2
	I	F1	F3	F3	F3	F5	F3	F1	F3	F4	F1	F4	F3

Table 4-6: Sensor ID with their relative location in the pressure mat

		<i>Sensor Row (m)</i>											
		I	II	III	IV	V	VI	VII	VIII	IX	X	XI	XII
<i>Sensor Column (n)</i>	VI	29	57	40	58	45	61	70	52	67	49	66	48
	V	38	56	41	59	44	62	71	53	68	50	65	76
	IV	37	55	42	60	45	63	72	54	69	51	64	76
	III	10	28	15	33	18	36	27	9	24	6	19	1
	II	11	29	14	32	17	35	26	8	23	5	20	2
	I	12	30	13	31	16	34	25	7	22	4	21	3

4.2.3 Pressure Mat Board Setup

The surface pressure mat's electric diagram for a single section can be seen in Figure 4-14. It consists of 8 sections, each containing 9 FSR elements. The data from the pressure sensors is sampled via serial analog multiplexing as shown in Figure 4-15. The data is gather for each element and pre-processed on the microcontroller and later sent to the computer for further processing and analysis. In the microcontroller the data is gathered (See Appendix A for script), formatted into a string per

sample, and compensated for hysteresis and drift. This pre-processed data is later used in the MATLAB® program and is calibrated according to the location of the sensor. If the sensor is located on top of the air spring, the calibration might depend on the gauge pressure of the air spring. The calibration data is then interpolated and applied to the measurement.

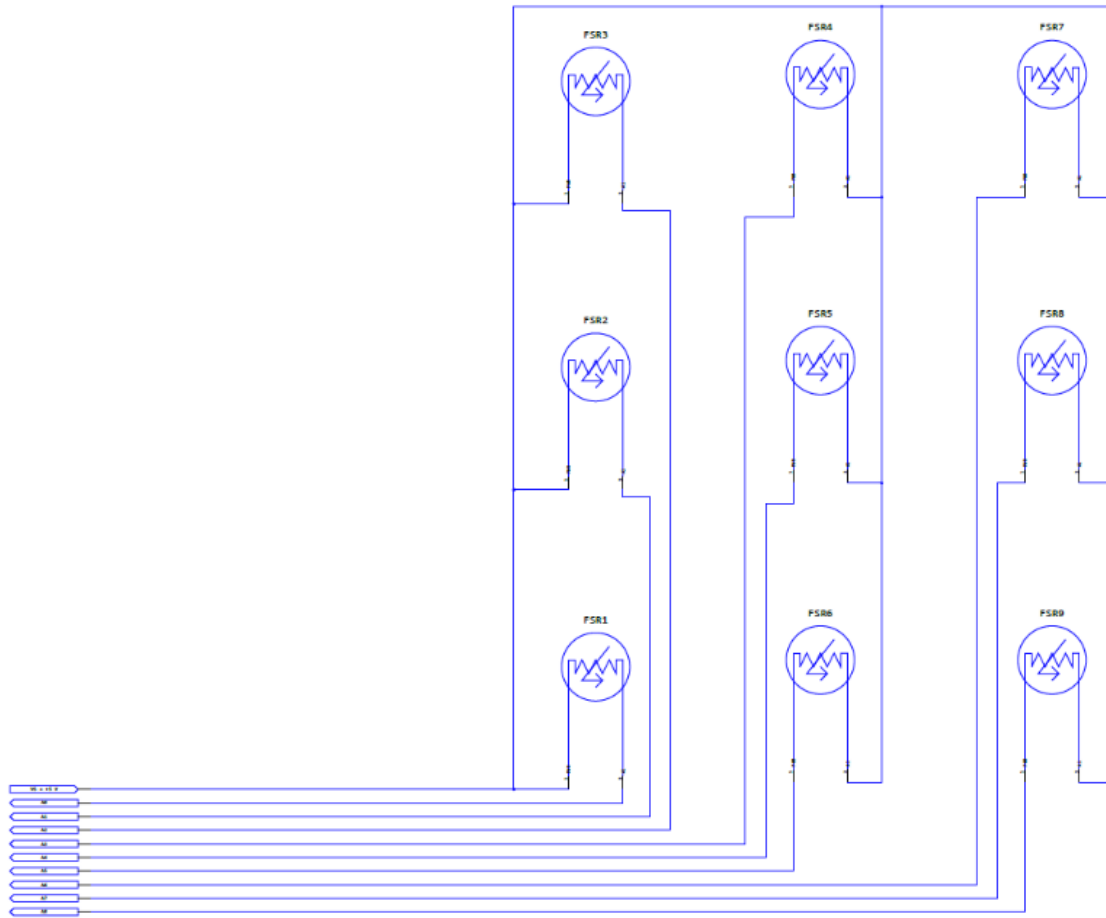


Figure 4-14: Pressure mat diagram for a single section containing 9 FSR elements.

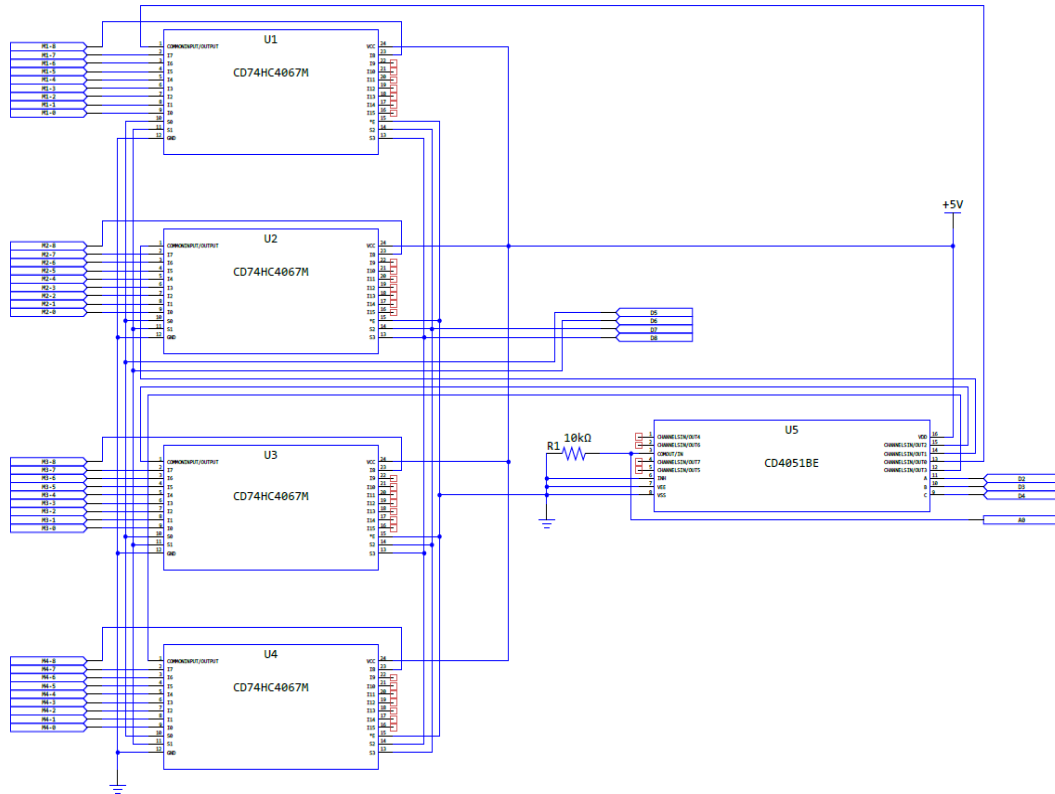


Figure 4-15: Serial analog multiplexing connection block.

4.3 Development of Pneumatic Actuation System

In order for the seat to have automatic lumbar control, pneumatic air-springs had to be installed on the seat. The design for the seat in this thesis has been equipped with 2 overlaid air-springs to account for the contour of the lumbar gap between the seat and the occupant. Both air-springs work together for most configurations. The lower air-spring can be configured to accommodate occupants with lower lumbar support needs (i.e. children).

The curvature of the air-spring is a function of the internal pressure (0 to > 6 kPa differential pressure). The pressure is constantly monitored via 4 absolute pressure sensors and the signal is used in the controller. The air is pressurized via a DC air compressor and the air is redirected and controlled with four 3-way and one 2-way normally closed solenoid valves. The air-springs are located between

the PU foam core and the FSR pressure mat as shown in Figure 4-16. The operation for system is done via a microcontroller (Arduino R3) referred as MC2, that can communicate to the pressure mat microcontroller referred as MC1, via digital input/analog output (Table 4-7 shows the truth table communications commands). The truth table consists of two digital signals that allow the system to attain one of the three states, close valves, deflate and inflate (Note that 'X' is a 'don't care' input).

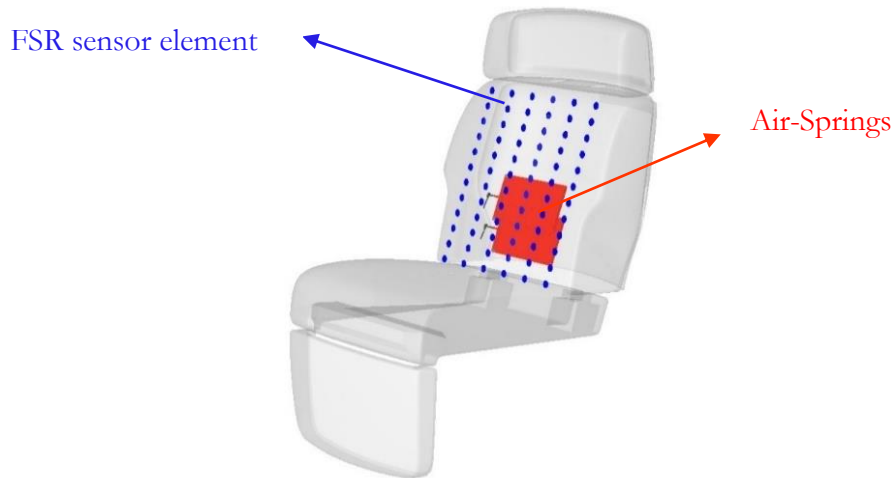


Figure 4-16: Sensor and actuator positions on the seat's cushion.

Table 4-7: Control Inputs/Outputs for Air-spring(s).

Action	MC1 (Inputs to MC2)		MC2 (Outputs)					
	D12	D11	D2	D3	D4	D5	D6	D7
Close Valves	0	0	0	0	0	0	0	0
Deflate	0	1	0	0	0	1	1	0
X	1	0	X	X	X	X	X	X
Inflate	1	1	1	1	1	0	0	1

The MC1 interfaces with the main computer via USB RS232 Serial communication as shown in Figure 4-17. The PC or controller box receives the pre-processed data (gain adjusted, semi-calibrated and properly formatted data) from MC1, completes the main calibration for the FSR data, calculates the pressure distribution and pressure characteristics (BRD%, max pressure, average pressure,

pressure loading and ideal pressure distribution), runs the controller algorithm and sends commands to MC1. MC1 collects FSR pressure data and pneumatic pressures (p_{atm} , p_1 , p_2 and inlet valve pressure p_v), and pre-process the data and relays commands from the controller to MC2. MC2 runs the control commands directly on the valves and air compressor, monitors the pneumatic pressures directly to avoid over pressurization of the air-springs due to pressure differences in the cabin or system failure.

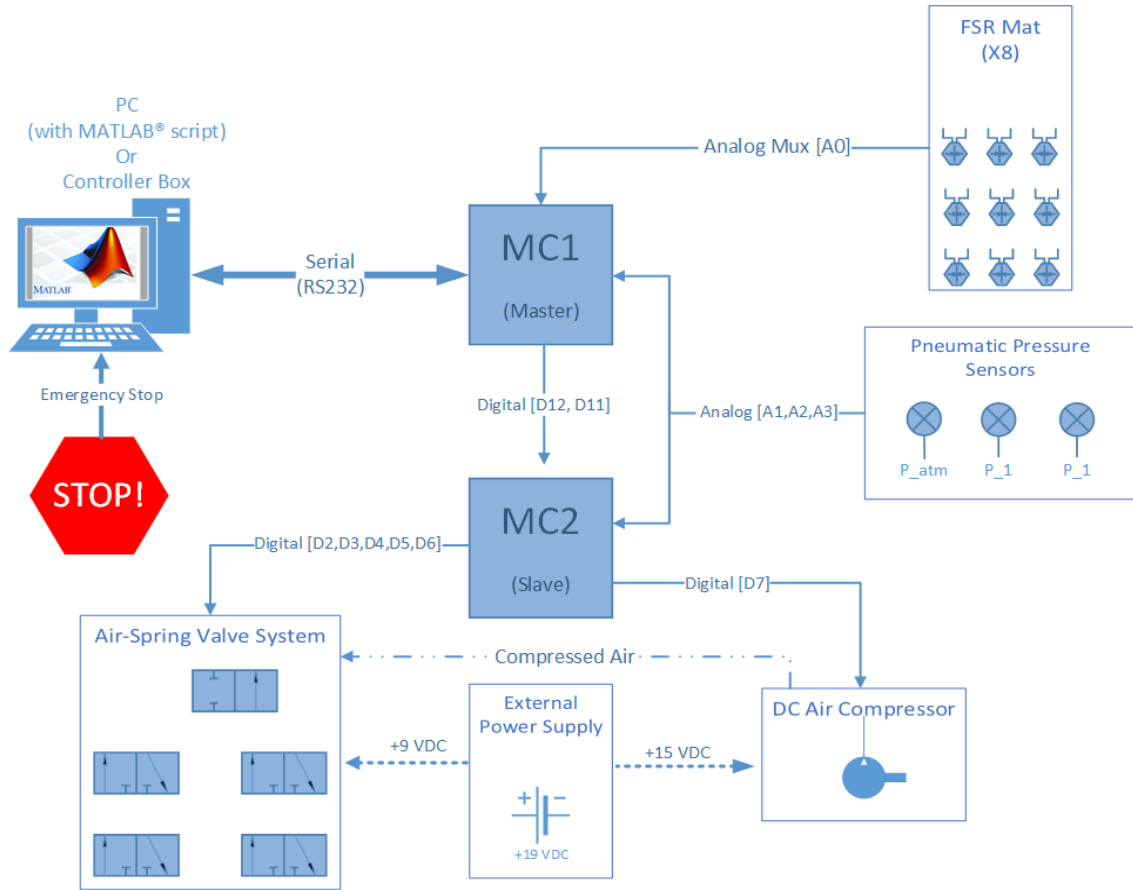


Figure 4-17: Hardware communication flowchart.

4.3.1 Actuator Board Setup

The PCB contains the circuitry and electric components for the pressure regulation for the lumbar air springs. The electric diagram is shown in Figure 4-18. As can be seen in the electric diagram, the atmospheric pressure is constantly monitored via (MPX4). This is done in order to compensate the gauge pressure in the air springs since the aircraft cabin pressure changes throughout the flight. In this figure, the power system can be seen to have 3 different voltages, +15 V (external) for the air

compressor, +9 V (external) for the solenoid valves and +5 V for the MPX pressure sensors. Two external voltages are used to avoid overheating of the solenoid valves and proper operation of the air compressor. The PCB holding the electronic components has the air-spring valve system, DC air compressor, absolute pneumatic pressure (APP, for short) sensors, and connection to the external power supply, FSR Pressure mat, microcontrollers and PC. The air-spring valve system (Figure 4-19) contains all 3 APP sensors with their port inserted into the valve connectors (Figure 4-19 c). The APP sensors are integrated piezoresistive transducers, with op-amp circuitry. A low pass filter is applied to the APP sensor analog signal and there was no need for calibration since the sensor is well conditioned, amplified and compensated for temperature and humidity (see App B2 for more details).

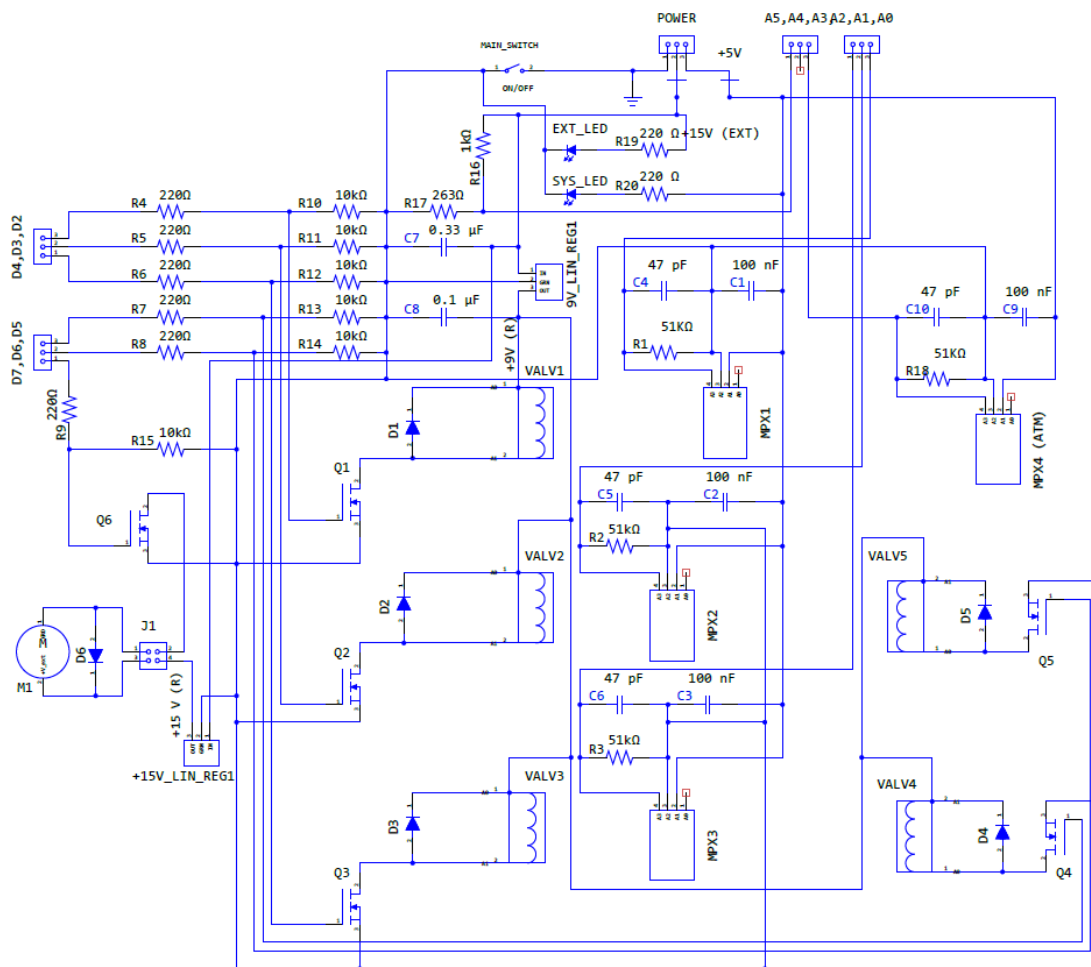


Figure 4-18: Air Pressure Regulation Circuitry for Lumbar Air Spring

The board is designed in such a way that three control states are available to the controller. The controller, discussed in the next chapter includes a control algorithm to achieve the required curvature and thus the required ideal pressure distribution. The feedback signals (pressure distribution and pneumatic and atmospheric pressure) are also provided from this board to the controller.

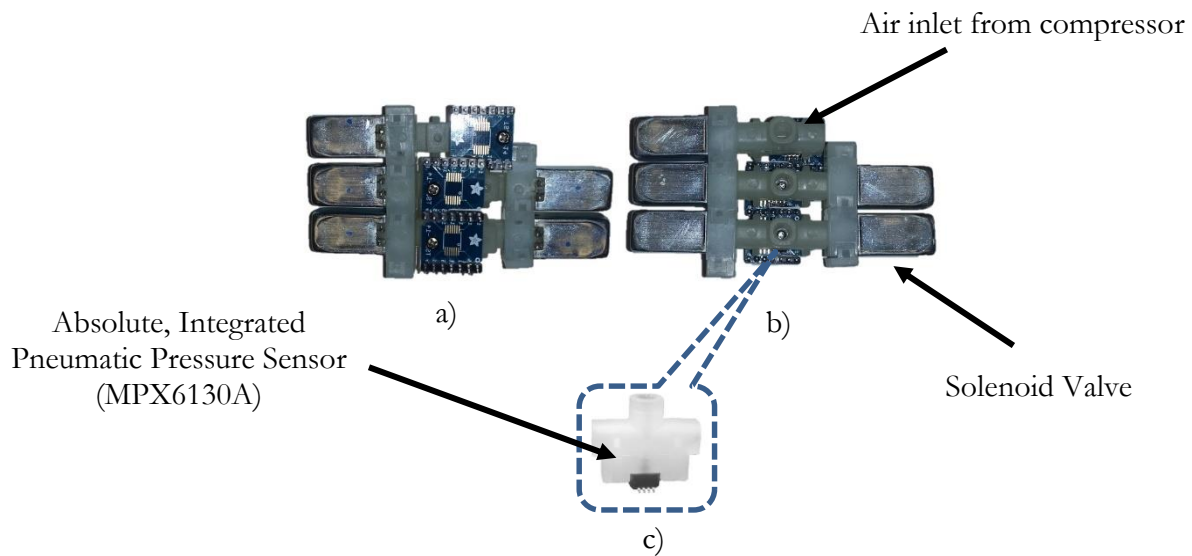


Figure 4-19: Air-Spring Valve System. a) Backside b) Top side, c) Pneumatic Sensor.

CHAPTER 5 Seat Control System

As discussed in §3.1, the control system must work with the discrete values at various locations of the backrest surfaces curvature and pressure distribution. The control system will compute (with respect to the ground state, measured pressure distribution and the pneumatic pressure) the foam deflection at each control point due to \tilde{P} . Air-spring pressure is required to create the curvature needed to decentralize the seat surface pressure and the corresponding control signal is a voltage output to the compressor.

The BRD% and the approximated contact area will be monitored. These two parameters will serve to verify the effectiveness of the air-spring deflection on the reduction of discomfort. Theoretically, lowering the value of the BPD% and increasing the contact area are indicators of decreasing discomfort. Thus, these two values are expected to improve as the seat's curvature approaches the ideal curvature given by the idea pressure distribution. Average and peak pressure will be taken into consideration if the surface pressure exceeds the allowed pressure values (20 kPa) as proposed in [20].

The control system is designed to run through a GUI (Figure 5-1) which serves to display the pressure distribution, pneumatic pressure, BPR%, contact area and PBR in real time. Through the GUI, the seat's hardware (MC1, MC2 and RoboteQ) communicate with Simulink and the MATLAB script. Manual inputs (via a slider button or text serial command line) can be enable on the GUI if automatic lumbar control is not desired.

Before proceeding to the control system design, the determination of the set-point input and plant must be clarified. This involves to experimentally evaluate the backrest's foam deflection under

certain load. The data obtained from the compressive tests will be used to obtain the stress-strain relation of the foam under compression. This can be generalized for any foam used in the backrest by using the constitutive model with experimental data. To compute the change in foam curvature when the load P is applied. The deflection of the air-spring (actuation) must be derived as well. The air-spring will be used to make the necessary changes in the curvature of the seat in the lumbar region.

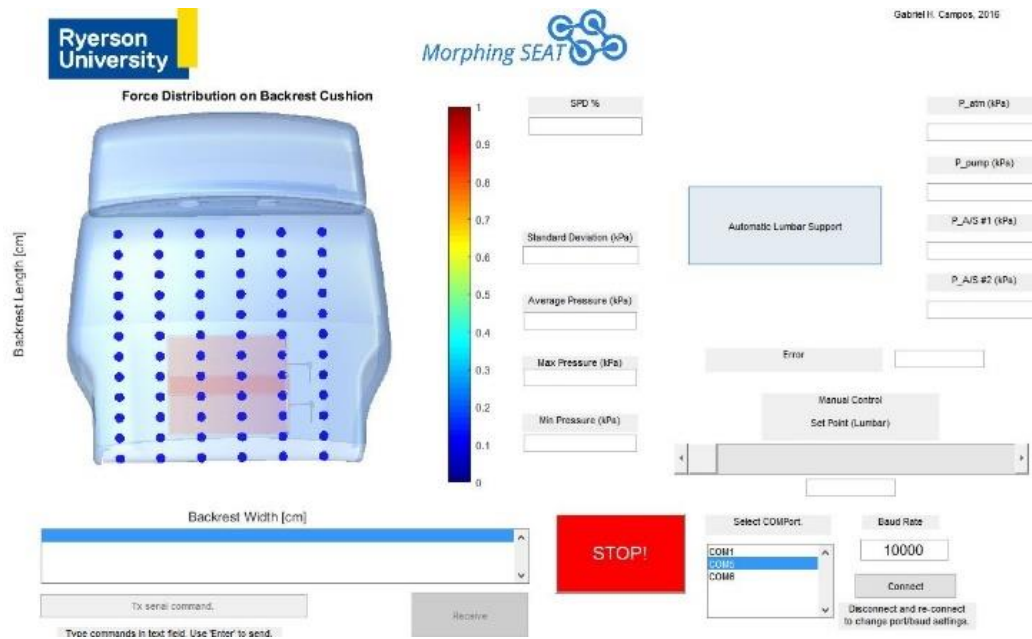


Figure 5-1: Graphic User Interface.

5.1 Plant

For the initial prototype and the early version of the second prototype of the ALAS system, the board and control system were designed to run with a controller as discussed in the previous chapter. However, to increase the performance, the hardware was slightly modified to include a RoboteQ[®] motor controller (FBL2300 Family). The RoboteQ[®] controller is used to provided the required variable voltage input signal to the air compressor, which translates into changing the air-spring pressure, p_s . However, the voltage commands to the compressor are generated in the control system in Simulink and relayed to the RoboteQ[®] by the MATLAB GUI/script via Serial COM Port.

In other words, the RoboteQ serves as the power converter to the air compressor. The plant includes the air-spring (with RoboteQ and compressor) and the foam core.

5.1.1 Actuator (Air-Spring) Deflection

When the air-spring is pressurized a deformation of its surface (membrane) is produced and has the characteristics of a non-linear spring. For a simple analysis, the geometry of the air-spring can be assumed to be a scalene ellipsoid with a volume given by:

$$V_s = \frac{4}{3}\pi abc \quad \text{Eq. 5-1}$$

where a, b and c are the semi-axes lengths of the ellipsoid. For the air-spring system used in this design $b = 2a$. Thus, the equation above can be simplified as:

$$V_s = \frac{4}{3}\pi a 2a c = \frac{8}{3}\pi a^2 c \quad \text{Eq. 5-2}$$

Furthermore, a and b are held fixed at the edges, only c is allowed to enlarge as volume changes. For the current analysis, it is assumed that the deflection of the membrane (Δz_s) is very large compared to the membrane thickness (t_s), bending and strain of the membrane are negligible while the dominant effect is due to surface forces caused by p_s and P over the area of the air-spring membrane surface area.

As seen in Figure 5-2, two air-springs are installed in the lumbar support area. The air-springs are partially overlapped to better fit the physiological shape of the lumbar area. The change in curvature due to the pressure at the overlapped section can be superimposed when both air-spring are actuated.

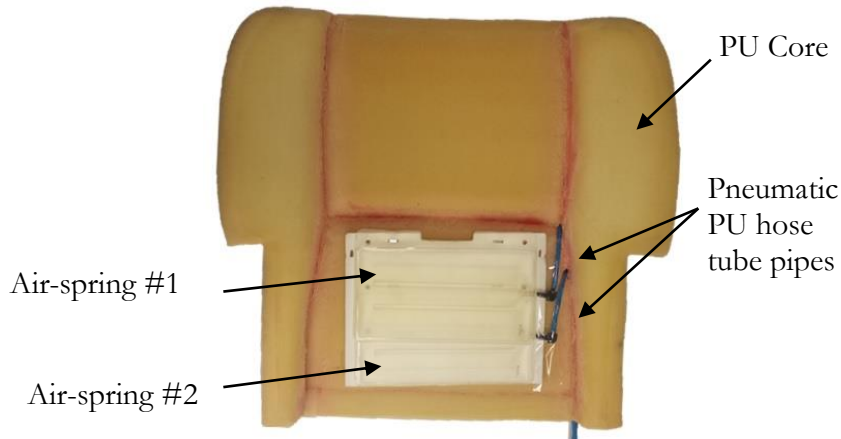


Figure 5-2: Location of the air-springs on the PU foam core.

5.2 Feedback

The feedback signals consist of the pressure mat output along with the air-spring pressure (for each air-spring and the inlet pressure p_v), and the cabin pressure (p_{atm}). Both the pressure mat signal (a 1 x 72 string) and air-spring pressure signal (1 x 4) are can be collected at a frequency between 4-112 Hz. The frequency (or sampling rate) is selected based on the type of operation. The pressure mat signal is collected and pre-processed on board by MC1, while the air-spring pressure signal is collected by MC1 and combined with the pressure mat signal in a single string format (1 x 76). The combined signal is then sent to the PC.

The inlets of each air-spring contains an absolute pressure sensor, which is zeroed at p_{atm} (which is technically the air pressure inside the cabin). The air-spring pressure is used instead of the absolute to avoid over pressurization since the cabin pressure is assumed to change throughout the flight. For this reason, the atmospheric (cabin) pressure must be closely monitored.

The feedback signal is then further processed in the GUI script where it gets normalized and calibrated. The GUI also computes the approximated contact area and BRD% and feeds these values along with the processed feedback signal to the ALAS system (Figure 5-3). The ALAS system is in charge of determining the adequate set-point value depending on the input signal that is related to the

anthropometry and sitting position. However, the ALAS block must contain the deflection contact model to determine the desired p_s set point value. The deflection model, as discussed in the next section, contains the hyperelastic model and data.

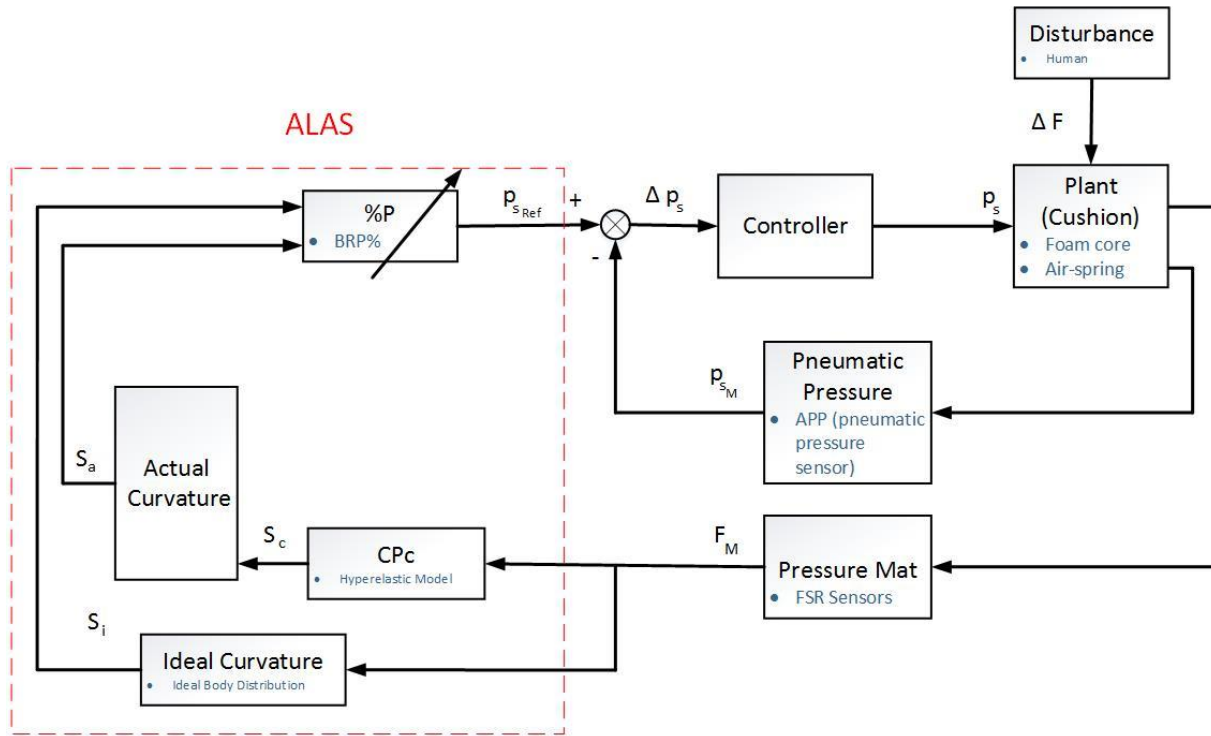


Figure 5-3: ALAS set-point algorithm.

5.2.1 Hyperelastic Curve Fitting

Unlike the Mooney-Rivlin model, Ogden's model requires nonlinear fitting. To facilitate the fitting process, the experimental data obtained in this work was fitted and plotted using the software HyperFit©. In the experiments, the data were fitted with Ogden's constitutive model.

The first experiment on the seat cushion was used to test the compression behaviour of the PU foam under a load on a solid surface. The compression stress-strain data was computed from this experiment and fitted using the HyperFit software. This test was performed seven times at different locations on the backrest foam. The number of experiments was chosen to coincide with the sensors

calibrated in §4.2.2.2 for two main reasons. First, the seven calibrated sensors have the most accurate response since the calibration was done individually for each of the seven sensor. Secondly, the calibration sensor is located at different locations on the backrest thus, evaluating the response of the foam at different areas. However, since the PU foam can be assumed to be isotropic, similar responses are to be expected. A sample compression experiment is shown in Figure 5-4.

The results from this experiment agree with the theoretical data for hyperfoam polyurethane seat-cushion like materials in [55]. However, as observed from Figure 5-4, some data points deviate from the model. As discussed in §3.3, the accuracy of the model can be increased by performing pure shear and tensile test. The discrepancy can be attributed to the fact that the real foam experiences compressibility and shear during a compression test – two factors that are not accounted for in this model. Therefore, it is best to use Ogden’s hyperfoam constitutive model (Eq. 3-52) for the case where load is applied directly to the foam from a rigid surface.

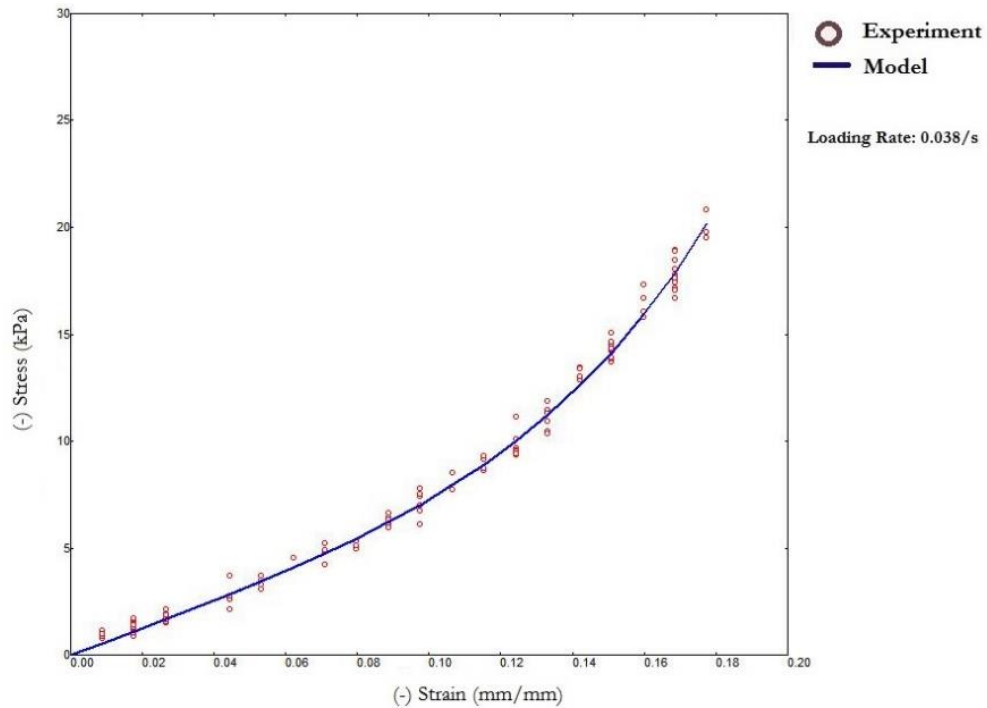


Figure 5-4: PU foam stress-strain compression test

In the second test, the PU foam and ballistic gel were tested under compression. The sample (ballistic gel on top of the foam) was tested for the pressure range of 0 – 112 kPa. However, only the stress range of 0 – 20 kPa was considered, as pressures higher than 20 kPa are assumed to be uncomfortable as discussed in CHAPTER 2.

This experiment was performed in order to better represent the specific loading profile encountered in the seat (human-seat contact model). Figure 5-5 shows the experimental results for one of the sample of this test. The experiment was performed as described in §4.2.2.2 with set-up shown in Figure 4-11 and repeated once for each of the seven calibrated sensors.

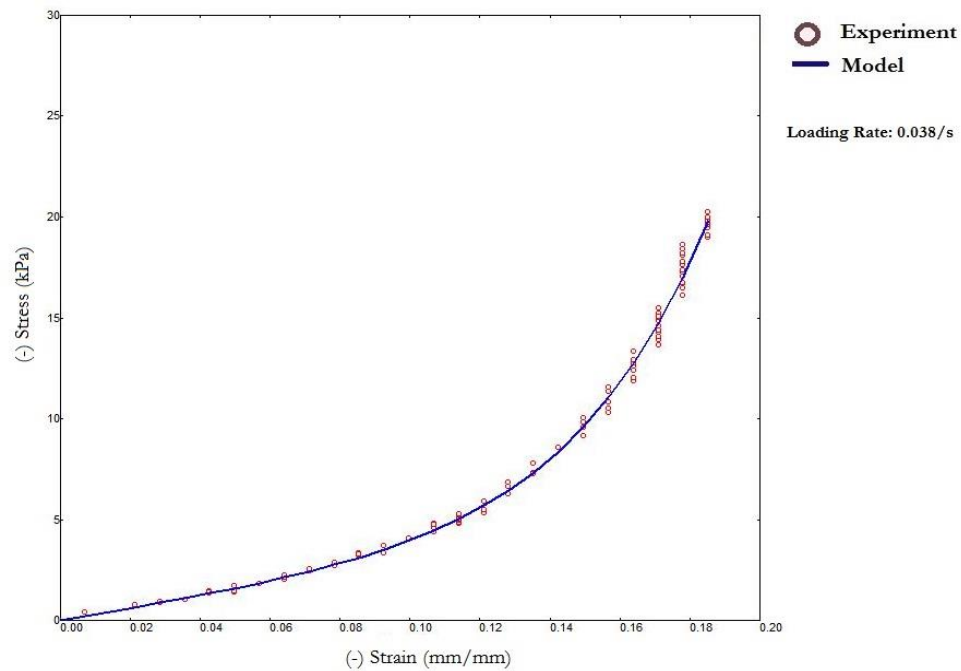


Figure 5-5: PU foam-ballistic gel stress-strain compression test

There is better correlation between the data and model in this experiment. This is mostly because the ballistic gel is incompressible and shear is negligible. For the control system, the data from the second experiment will be used in the deflection contact model. This is because it better represents the loading profile on the seat and the hyperelastic model has a better fit to the experimental data. The model parameters for both graphs are summarized in Table 5-1.

Table 5-1: Experimental Ogden Model Parameters

Parameter	PU Foam	PU foam and Ballistic Gel
μ_1	0.259	0.087
α_1	24.285	31.579
μ_2	10.892	10.987
α_2	3.355	1.851
μ_3	16.523	66.171
α_3	-0.093	-0.044

5.2.2 Set-Point

The problem addressed in this work is how to select a set-point that can create a comfortable pressure distribution for a wide range of anthropometry and sitting positions. This is done by the ALAS system. Figure 5-6 shows the overview of the real seat's control system.

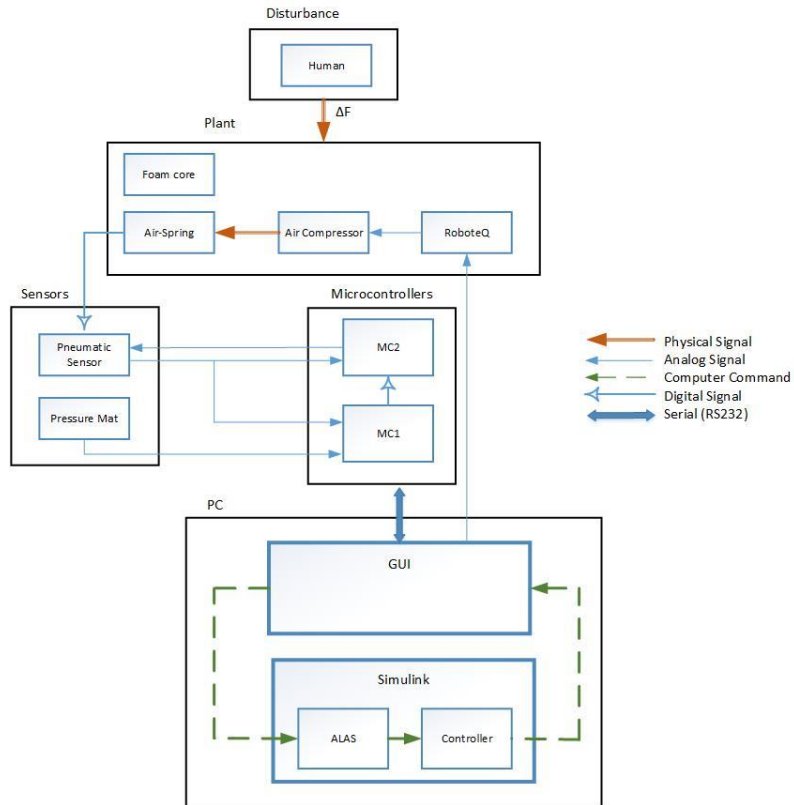


Figure 5-6: Seat system.

The seat control system consists of 4 main groups, the plant as discussed in §5.1, the microcontrollers which relay the commands and signals to and from the PC, the PC software which runs the control algorithm (including ALAS) and the sensors (as studied in CHAPTER 4) which provided the necessary feedback.

This is the control method used to develop ALAS’s variable set-point, as seen in Figure 5-3. The ALAS block works on the curvature s_j , which are interpolated from the points $z_{i,j}$ as explained previously Also, the BRD% is used to evaluate the discomfort as discussed in §3.1.3, in Eq. 3-37 when applied to the backrest of the seat.

5.2.3 Control Method

The simplified overview of the control system can be seen in Figure 5-7. The present control problem is how to use the variable set-point value, based on the feedback signal (F_M and p_{sM}), to adjust the curvature by changing the pressure inside the air-spring(s). The control variable is the pneumatic pressure of the air-spring, p_s . The task of the control system is to decrease the error (Δp_s). This is achieved by changing the gauge pressure inside the air-springs which results in a deflection. However, this is not a trivial task since the plant is highly non-linear.

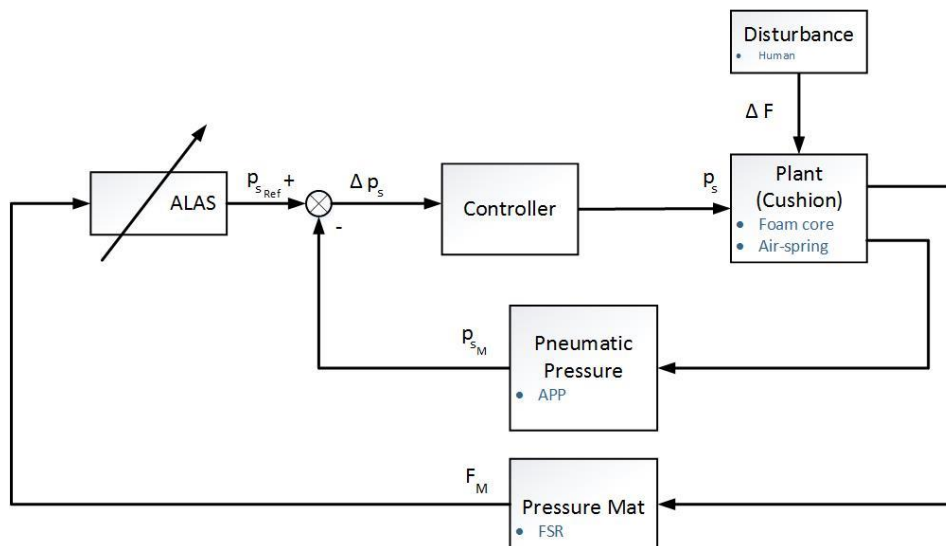
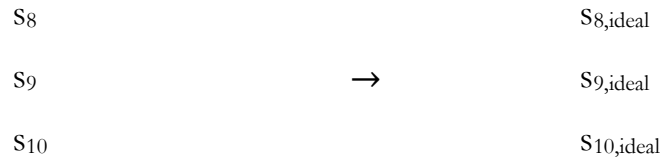


Figure 5-7: Simplified control system overview.

For this case, the actuated control point is assigned to cover the lumbar support region only. That is, the control points, 8 - 11 are actuated control points, while the rest are passive control points (Figure 4-18). Therefore, from the spline, the only internal ICPs that are affected directly by the p_s , that is the actuation variable are:



The rest of the ICPs are indirectly affected by the weight decentralization caused by Δp_s .

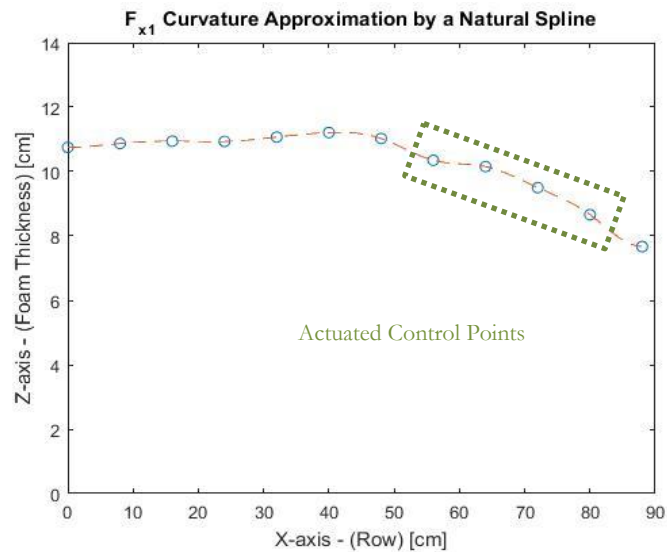


Figure 5-8: Control points on a spline section.

A simple P controller was used to test the ALAS system. The gain k_p was selected to be linearly proportional to the error and voltage input into the compressor. Recalling the maximum error in the system is given by the system limitation ($\Delta p_{max}=6$ kPa, differential pressure) and the operational voltage range ($V_{max}=15$ V). Thus the gain is calculated to be $k_p = 15/6$ and only for positive voltage, as negative p_s is archived not by the compressor by instead by opening the exit solenoid valve. It is important to note that a P or even a PID controller on their own are considered sub-optimal controllers and care must be a taken since the plant is non-linear.

The Simulink in Figure 5-9 shows the algorithm used to compute the set-point value in then real plant. This set-up was used in the next chapter to corroborate the experiment in §6.3. This experimental set-up uses only one of the 2 pneumatic pressure signals to simplify the test. The air-springs are used in parallel. However, this set-up can be without difficulty modified to account for multiple air-springs. This algorithm used the P-controller in this section. However, the controller's output is modified from p_s into voltage to run the compressor. This modification in the control signal is done by a gain and a round function since the RoboteQ controller can only take integers.

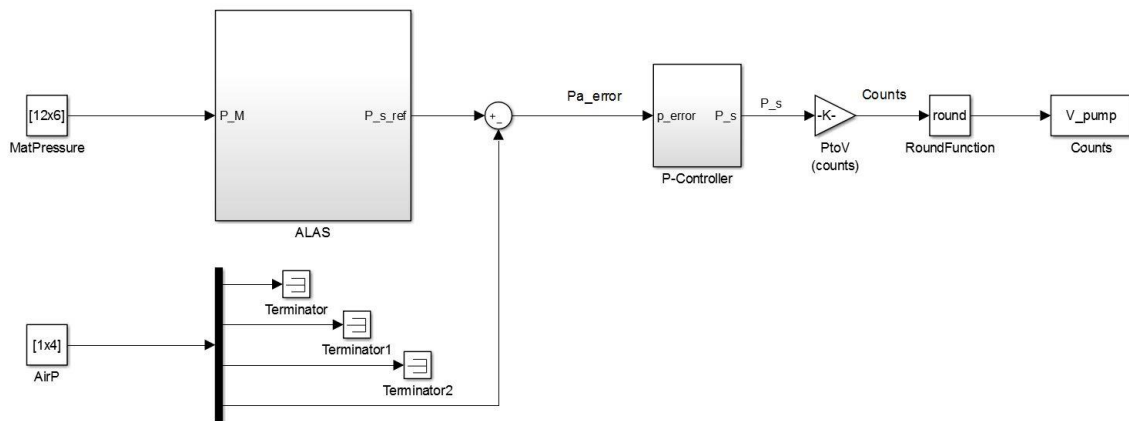


Figure 5-9: Simulink control system method (real plant).

CHAPTER 6 Testing and Results

For testing the theory of this thesis, two seat prototypes were used as seen in the experimental setup of Figure 6-1. The first seat prototype (black seat) was a modified automobile seat (Ford Taurus SHO® model 2012) and used to start the developing of the seat pressure mat, recline mechanism and pressure mapping. The second prototype (purple seat), a business aircraft seat from a Global 5000 aircraft. The seat was provided by Bombardier Aerospace and was modified to include the pressure mat, air-spring/valves system, and manual recline of the backrest for testing purposes only.



Figure 6-1: Experimental setup of seat prototypes.

Testing for each subsystem was performed individually before conducting the final testing for automatic lumbar support. In the last stage of the project, the performance of the ALAS system was evaluated. For this purpose, a 1:1 prototype was created and integrated into the Global 5000 business class seat. The pressure mat containing 72 FSR sensor elements was placed on the backrest of the seat. Below the pressure mat, the two air-springs were positioned on the lower part of the backrest which coincided with the lumbar area for the passenger (Figure 6-2).

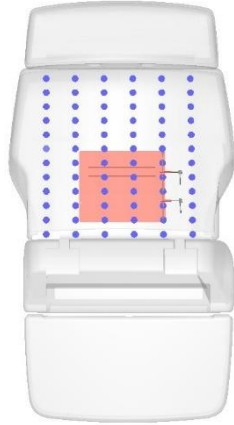


Figure 6-2: Front schematic of morphing seat.

The final test was conducted in the second prototype. The differences between the seats' geometry and recline mechanism can be seen in Table 6-1.

Table 6-1: Seat prototypes comparison.

Seat Model		G7000‡	Experimental	G5000 mock-up	
Degrees of Freedom		6	6	2	
Range of Motion	Rotation	N/A	360°	N/A	
	Lateral	N/A	± 11.5 cm	N/A	
	Forward/Back	N/A	14.0 cm	N/A	
	Recline (backrest)	N/A	34.1°-11.6°	N/A	
	Tilt (seat)	N/A	6.8°-11.6°	N/A	
	Seat Lift	N/A	~ 4.0 cm *	N/A	
Max Dimensions	Seat Pan	Length (cm)	47.54	53.5	46.4
		Width (cm)	53.34	47.0	48.9
		Thickness (cm)	13.29	11.4	14.0
	Backrest	Height (cm)	48.28	63.5	52.0
		Width (cm)	61.61	52.0	58.4
		Thickness (cm)	22.18	22.0	16.5
	Headrest	Height (cm)	18.26	22.9	24.0
		Width (cm)	51.94	22.9	45.0
		Thickness (cm)	15.85	12.7	13.0

* Approximated value from simulation

‡ Values obtained from CAD model

6.1 Pressure Mat

The pressure mat (as seen in Figure A-0-7, App. E) was initially designed to have low resolution (36 sensor elements in total), and it was intended to be used on the first seat prototype. The

first seat prototype was used as preliminary testing of the data gathering of the FSR mat, calibration methodology, graphical display of the pressure mapping and the concept of SPD% and BRD% (Figure 6-3).

Following the calibration, the pressure distribution was measured on a Synchrotilt mechanism on the first prototype (designed by Lin) using the pressure mat developed in this work. However, due to the original design of the first prototype, the backrest recline angle of the Synchrotilt range was limited from 90° (upright position) to 99.6° (0° to 4.8° for seat pan). Both the backrest and seat pan recline angles were measured using optical encoders. The effect on pressure was measured using the low resolution pressure mat and are shown in Figure 6-4. Two readings (front and back side of the seat pan) were taken using the 36 sensor mat for a total of 72 pressure reading on the seat pan. The effect of the Synchrotilt reclining on the pressure distribution for both the backrest and seat pan, each with the low resolution pressure mat, can be clearly observed. Also, it was observed that at higher recline angle the pressure distribution is highest in the mid-back area. This centralized pressure distribution can be improved with an active lumbar support. Which is the main topic of this thesis.

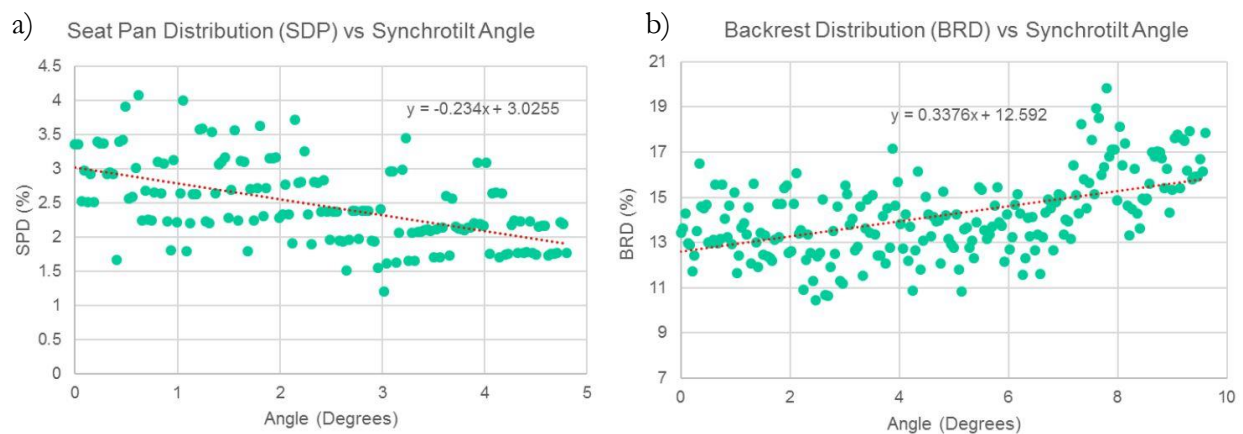


Figure 6-3: Pressure distribution from Synchrotilt a) Upright position b) Reclined position.

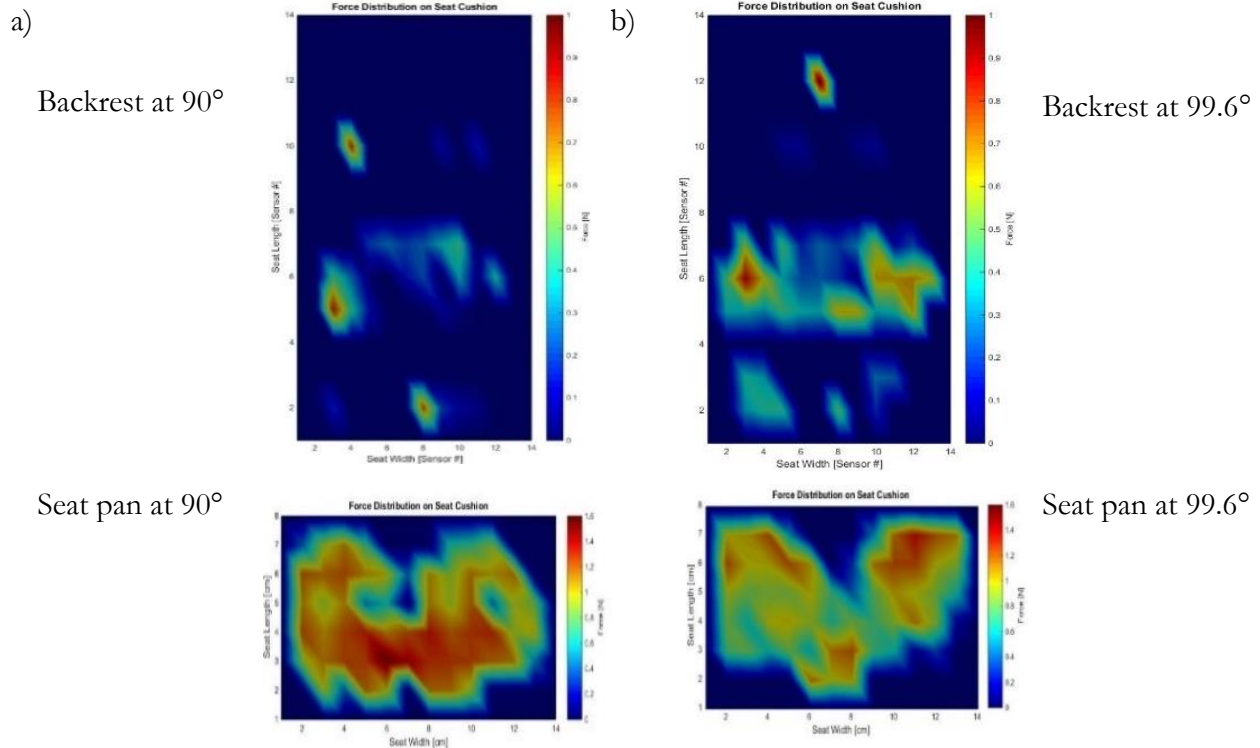


Figure 6-4: Pressure distribution from Synchrotilt a) upright position b) reclined position.

In a static seat, there is no feasible way to account and compensate for dimension mismatch between the user and the seat that leads to a pressure concentration. However, as it was discussed in CHAPTER 5, this very issue can significantly be improved by increasing the curvature of the seat at the lumbar support. As the contact area in the lumbar support increases, the contact pressure decreases the upper or middle back. In turn, this adjustment at the lumbar area leads to a better distribution of pressure in the back. This is based on the conditions stated in the control problem

- 1) Match the ideal pressure distribution.
- 2) Decrease the BRD%.
- 3) Lower peak and average pressure distribution.
- 4) Increase the contact area.

After testing the calibration accuracy and the pressure map, the number of sensor elements in the pressure mat was increased to 72 to meet the control feedback requirements of the ALAS system.

The real sample response of the pressure mat during operation is illustrated in Figure 6-5 (animation included for visualisation purposes only). The data is collected via MC1 and processed in MATLAB to compute the pressure distribution.

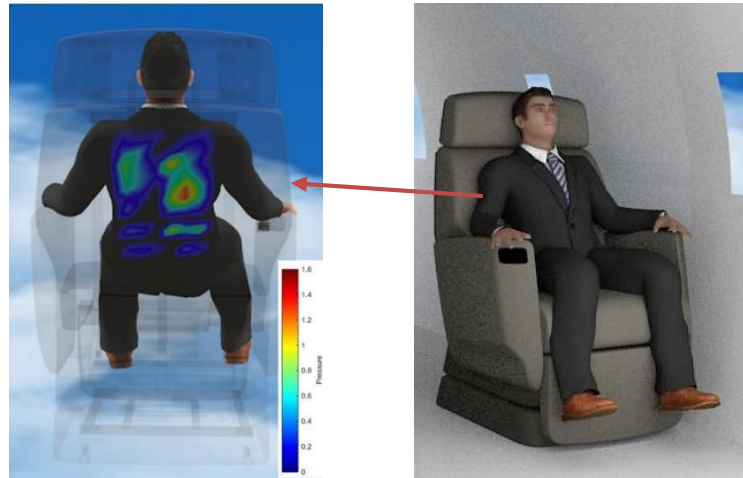


Figure 6-5: Visualisation of the actual pressure distribution superposed on a passenger animation.

6.2 Pneumatic Actuator

The change in internal pressure of the air-bag results in a change in stiffness and contact area at the lumbar area. By doing so, the passenger's weight is decentralized and the pressure distribution can be improved. The pressure inside the air-spring can be controlled individually for each bag. Figure 6-6 demonstrates the inflation test for a single air-spring for a step input. For this test, the target pressure was arbitrarily set to 102 kPa. The test in the figure also shows the depressurization of the airbag. Both the pressurization and depressurization are controlled by the inlet/outlet solenoid valves. The concept of decentralizing the weight of the person via air-springs as done in this work, can be expanded to have more than two air-springs. The entire seat can in fact be actuated by increasing the number of air-springs. This would result in a potentially more efficient system. However, this comes with the disadvantage of an increase in complexity of the system.

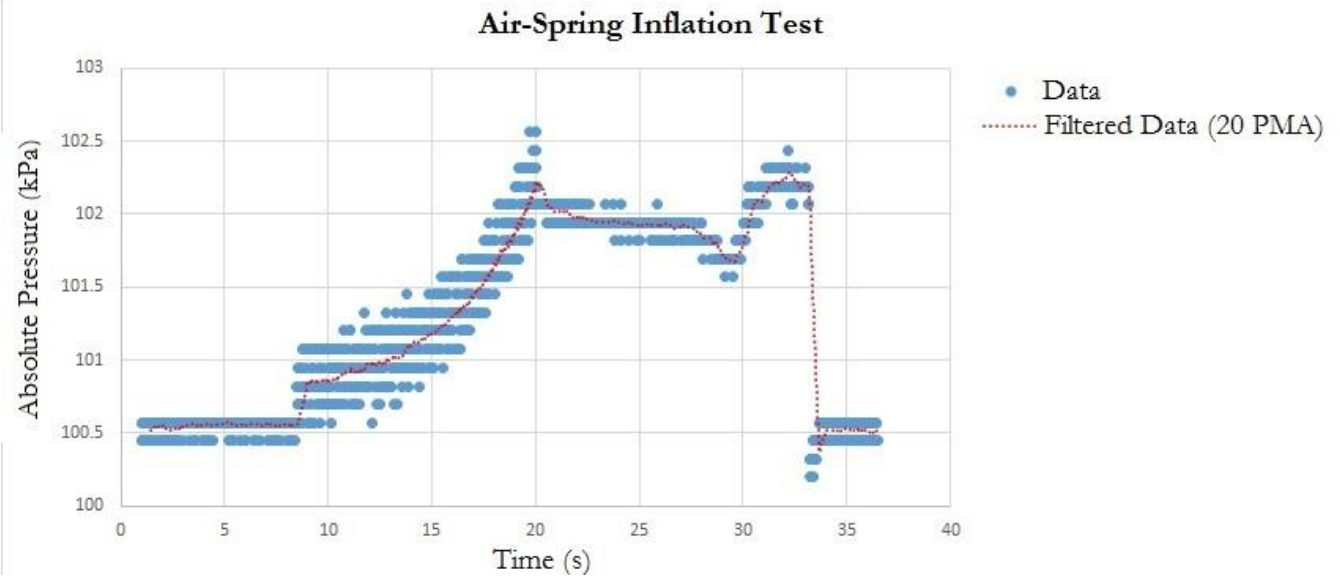


Figure 6-6: Response of air-spring during pressurization.

6.3 Performance

The final testing was conducted on the G5000 seat prototype (Figure 6-7). The seat was equipped with the 72-sensor element pressure mat on the backrest. The sensors in the pressure mat were arranged so that they cover all four different areas (A1 to A5, A4 and A5 are considered to be symmetric). This configuration resulted in a rectangular formation of the sensor with a separation between adjacent sensors of $h_e = 4$ cm and $l_e = 8$ cm. Two air-spring actuator were placed at the lumbar section of the seat, just below the sensor layer.

A GUI was designed for the purpose of the final test. In the GUI, the surface pressure distribution, the air-spring pressures, the atmospheric (cabin) pressure, and the external voltages for the valve system and compressor are constantly monitored and sent to the PC. The GUI provides the display of the pressure distribution in real time and relays the processed feedback signal to the Simulink control system and reads the command out of the Simulink.



Figure 6-7: Bombardier's Global 5000 seat.

When the user selects to use of ALAS system in the GUI, the script calculates (from the hyperelastic data and the feedback from the sensors) the required pressure change of the air-spring which results in the surface deflection. The inflation process was controlled using a simple P-controller for evaluation purposes only. The change in surface deflection in the sagittal plane are constantly iterated. A sample of the control points can be seen in Figure 6-8.

Moreover, if the splines (from the control points) are multidimensionally interpolated, the overall backrest curvature can be approximated as seen in Figure 6-8b. In this figure, the control points (and thus the FSR sensor element locations) and the approximated curvature of the backrest is superimposed on an actual image of the backrest. This is done to graphically show the location of all the control points, both passive and actuated, relative to the actuated backrest.

For the MC1 microcontroller the baud rate used for graphical display was 2710. This BaudRate was matched to the main computer for optimal graphical processing speed. For automatic lumbar morphing support, the Baud Rate used was 1000, with a respective frequency of 25 Hz. As suggested in [56], from their study of a fast FFT analysis for the FSR's voltage response it was determined that frequencies higher than 40 Hz should be filtered out.

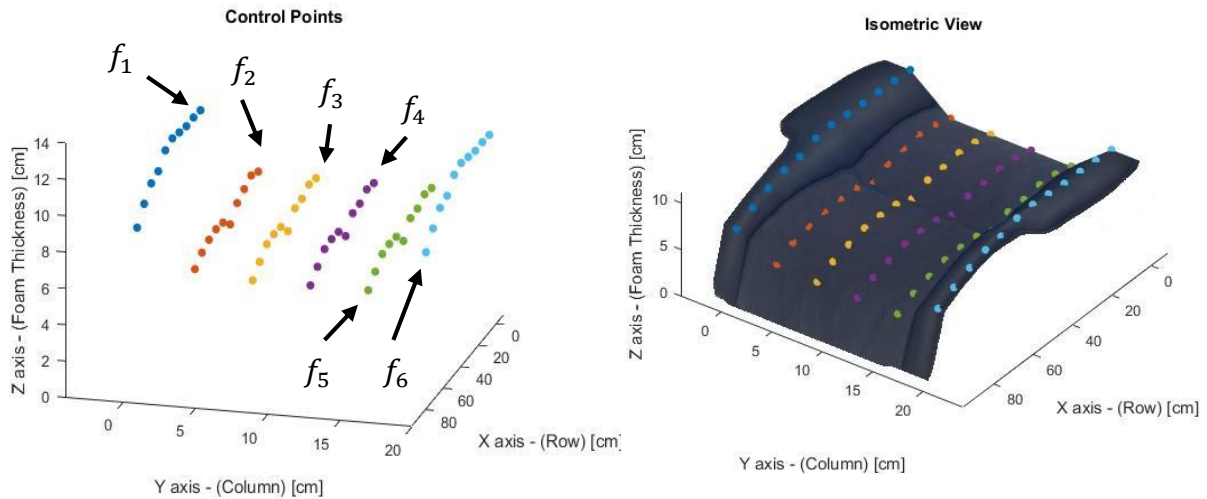


Figure 6-8: Load control points on the seat.

The MATLAB script contains all the necessary functions, reference values and dimensions for the algorithm to collect, process and display the data from ALAS system. The script also contains the signal filters for the pneumatic pressure sensor (a simple moving average filter), the normalization gains and calibration curves. The feedback from the pressure mat and pneumatic sensors are processed in the MATLAB/GUI script and sent to Simulink. The Simulink contains the ALAS block that uses the inputs (P , p_s , $BRD\%$) along with hyperelastic deformation model as a lookup table, the curvature of the backrest at its ground state, the experimental curvature of the air-spring and the reference $\%BRP$ (Eq. 3-14) from the ideal pressure distribution. The ALAS block in turn produces the desired internal pressure of the air-spring (the set-point) and inputs it into the controller. The controller's output is then sent to the MATLAB/GUI script where it gets processed into the required data format before it is sent to the RoboteQ.

The ALAS system was tested and the results can be seen in Figure 6-9. A sample load was used to test the functionality of the ALAS system. From the performance test it can be concluded that the actuator indeed changes the pressure distribution on the backrest. This pressure distribution can be seen to have a lower $BRP\%$ (Table 6-2) as well as an increase in the overall surface contact area.

This suggests that the ALAS system can produce an increase in comfort (decrease in discomfort). Most of the centralized pressure was shifted to the middle and lower backrest as a result from the air-spring deflection. Note, because only a P-controller was used (which is not recommended for this application), oscillations were observed.

From this experiment it can be concluded that the sensor mat can be rearranged to only cover areas A1, A4 and A5 since the side areas (A1 and A5) are not used. If the same number of FSR elements is kept, the mat sensor density can be increased and in turn, a better approximation for the contact area and pressure distribution can be obtained. Also, the seat curvature is mostly affected by the air-spring's inflation rather than just the load applied to the foam core. It is suggested that only the change in curvature of the air-spring is used.

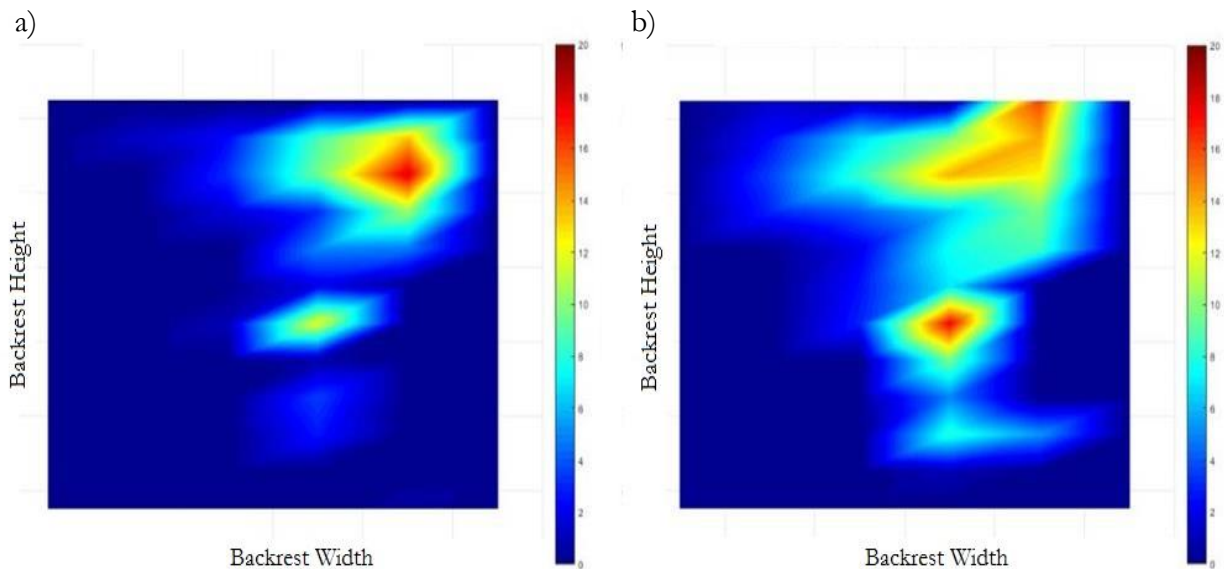


Figure 6-9: ALAS Experimental Results a) Before a) After Lumbar Support.

Table 6-2: Test Results

	Before	After	Difference
BRD%	20.49	17.25	15.8%
Standard Deviation (kPa)	5.09	4.94	3.0%
Peak Pressure (kPa)	17.99	17.54	2.5%

To improve the system, a better controller can be designed, as a P or even a PID controller alone would be a suboptimal controller. Also, a compressor with a higher mass flow rate can be selected to achieved a faster response. However, if the mass flow rate of the air going into the air-spring is too high, a sudden change in the air-spring deflection might result is discomfort. This system should be tested on other seats, recline angles, positions and as well with people with different body types to determine its true performance. Nonetheless, from this small experiment, the system does suggest a high potential for future automatic seat design adjustments to help increase passenger satisfaction.

6.3.1 Safety Features

To avoid over pressurization of the air springs the “cabin” pressure is constantly monitored and p_s is adjusted accordingly. In the case of a cabin depressurization ($P_{\text{cabin}} < P_{\text{dep}} = 55.2 \text{ kPa}$), the air compressor is halted and the air inside the air spring is vented out immediately. The system must then be reset manually.

The external power supply is monitored via voltage divider and limited via voltage regulators. If $V_{\text{ext}} > 23 \text{ V}$, the system is turned off to avoid over voltage. The system must then be reset manually.

Note: $V_{\text{max}} = 24 \text{ VDC}$.

The prototype is equipped with an emergency shutdown button which can easily be modified to be used on-board the aircraft by the crew. It could be used to restrict this function during take off/landing, excessive turbulence or in case of an emergency.

CHAPTER 7 Conclusion

7.1 Contributions

The work in this thesis brings together four separate concepts that were incorporated to develop a seat system used to improve passenger sitting comfort in an aircraft cabin. The seat system combines the knowledge from these concepts into a practical application to decrease sitting discomfort. The first contribution in this work was the introduction of the calibration method and real-time pressure mapping of the seat's surface in order to evaluate discomfort. Pressure mapping has been used to test seat designs before production but has never found a practical application in the seat design itself due to technical issues such as post-processing analyses of data and most importantly due to their high cost (\$17,000 to \$29,000 USD per pressure mat).

The second contribution in this work was the practical implementation of the ideal pressure distribution and the SPD% (BRD% for the back) on a seat design. The ideal pressure distribution and BRD% were until now only used for statistically testing of sitting discomfort. In this work, these parameters were used as references for the control method to achieve the reduction of discomfort in a morphing seat.

Lastly, the concept of automatic morphing seat during real-time operation was introduced along with the automatic control approach. Morphing surfaces in seats were up to now only manually controlled or in open loop control due to lack of a reference value (ideal pressure, etc.), and lack of a practical means of measuring discomfort reliably (via pressure distribution). Previous attempts for morphing seat surfaces only employed feedback from the pneumatic pressure of the air-springs actuator(s). Such feedback method of control is highly unsatisfactory due to wide diversity of human anthropometry, postures and activities often performed on the seat (reading, sleeping, etc.).

Secondary contributions included the development of a pressure sensing mat for a fraction of the cost of commercial pressure mats with similar accuracy. Implementing real time pressure distribution data, combined with the ideal pressure distribution as a reference for the automatic controller to morph the seat's surface with the aim to decrease discomfort. The demonstration that close loop control is possible. And the hyperelastic calibration of the FSR elements in the pressure mat.

7.2 Future Work

This work presented the fundamental theory on comfort/discomfort and the required systems needed to create an adaptable seat. More work is needed in order to improve the accuracy of the FSR elements for better results and faster development of seat designs. This can be achieved by creating a load normalization and calibration chamber. This chamber will also speed up the process for the normalization and calibration process compared to the method used in this work. Additionally, a subjective study (via subject evaluation) can be conducted on this seat design to evaluate the performance of the morphing system on comfort/discomfort.

The contact model can be improved by adding more detail of the material and its geometry. FEM can be performed to corroborate the models. The model can also be improved by adding posture detection (i.e. via image recognition or ultrasound proximity measurements) as a secondary objective parameter to compliment the pressure distribution parameters. Also, the algorithm should be tested in a pressurized environment to simulate the change in cabin pressure during the flight.

Improvements to the experimental set up can be done by reducing the interface of the pressure mat layer which lies between the user and the PU core. This vinyl-laminated sensor mat layer contains the FSR elements with their respective thin copper-film electrical connection. The effectiveness of the model can be increased by incorporating the sensor layer into the PU core by directly printing or

embedding the sensing area of the FSR into its surface. The electrical copper connections can be replaced with conductive, flexible thread that conforms to the shape of the seat design and has less impact on the contact area under study.

Future work on this study can be expanded by using better controllers or linearizing the plant. Also, future work can include a fully actuated seat design to cover all body regions. Each body region can be actuated independently to achieve the ideal pressure distribution discussed in the previous two sections. For a fully actuated design, the controller design is expected to exhibit high complexity. It would be interesting to see research done in this specific area.

Other areas that can be included in future work in order to improve the current design can include

- Software/Hardware optimization (to improve processing speed)
- Electrical design (commercial PCB design and increase power efficiency)
- Cost Analysis (Development, operation life cycle)

Lastly, future work on this topic can explore better material options for the foam cores of the seat. A possible material alternative to PU foam is polyester in the forms of suspension fabric for the backrest and 3D spacer fabric for cushioning in the seat pan. Polyester shows higher recovery in compression, better breathability (which provides improved thermal comfort), longer operational life and is recyclable unlike PU foam [57]. Moreover, suspension fabrics can be manufactured to have different stiffness and can potentially be actuated more efficiently than a foam core.

Appendices

A. Software

The following script is for the Master microcontroller (MC1). The script controls the pressure mat mux system and 2-way communication between the GUI and MCC2.

```
//March 11 2016
//Edited Oct 11 2016
//Gabriel Campos
//Use for GUI G5000 seat
//Contains pressure readings from air-springs
//4to1 MUX plus 9to1 MUX
//Conductance mapping
//Reads all 72 sensors in series with channel A0 & A1
//Can Receive data via Serial port (from Matlab)
char incoming[2] = {0, 0}; // for incoming serial data
//Mux control pins
int r0 = 0; //value of select pin at the 4051 (s0)
int r1 = 0; //value of select pin at the 4051 (s1)
int r2 = 0; //value of select pin at the 4051 (s2)
int count = 0;
int s0 = 5;
int s1 = 6;
int s2 = 7;
int s3 = 8;
int P0 = 0;
int P1 = 0;
int P2 = 0;
int fsrReading; // the analog reading from the FSR resistor divider
int fsrVoltage; // the analog reading converted to voltage
double fsrResistance; //voltage converted to resistance, make it "long"//unsigned
double fsrConductance; //unsigned
double fsrForce; // Finally, the resistance converted to force
long Time;
//Mux in "SIG" pin
int SIG_pin = 0;
static char output[6];
//double start, finished, elapsed, freq;
void setup() {
  pinMode(s0, OUTPUT);
  pinMode(s1, OUTPUT);
  pinMode(s2, OUTPUT);
  pinMode(s3, OUTPUT);
  pinMode(2, OUTPUT); // s0
  pinMode(3, OUTPUT); // s1
  pinMode(4, OUTPUT); // s2
  pinMode(11, OUTPUT);
  pinMode(12, OUTPUT);

  digitalWrite(12, LOW);
  digitalWrite(s0, LOW);
```

```

digitalWrite(s1, LOW);
digitalWrite(s2, LOW);
digitalWrite(s3, LOW);
//Serial.begin(2710); //USE this for GUI on PC with Graphics
Serial.begin(2400);
//Serial.begin(115200); //USE for actual operation
}
void loop() {
//Left Mat -----
SIG_pin = 0;
for (count = 0; count <= 3; count++) {
// select the bit
r0 = bitRead(count, 0);
r1 = bitRead(count, 1);
r2 = bitRead(count, 2);

digitalWrite(2, r0);
digitalWrite(3, r1);
digitalWrite(4, r2);

//End of 4to1 MUX

//Loop through and read all 16 values
//Reports back Value at channel 6 is: 346
for (int i = 0; i < 9; i++) {
fsrReading = readMux(i, SIG_pin);
fsrVoltage = map(fsrReading, 0, 1023, 0, 5000);
if (fsrVoltage == 0) {
Serial.print("00.00;");
}
else {
fsrResistance = 5000 - fsrVoltage; // fsrVoltage is in mV, 5.5V = 5000mV
fsrResistance *= 10000; // 10K resistor (to GND)
fsrResistance /= fsrVoltage;
fsrConductance = 1000000; // [micromhos]
fsrConductance /= fsrResistance;
Serial.print(fsrConductance);
Serial.print(";");
}
}
}

//Right Mat-----
SIG_pin = 1;
for (count = 0; count <= 3; count++) {
// select the bit
r0 = bitRead(count, 0);
r1 = bitRead(count, 1);
r2 = bitRead(count, 2);

digitalWrite(2, r0);
digitalWrite(3, r1);
digitalWrite(4, r2);

//End of 4to1 MUX
//Loop through and read all 16 values

```

```

//Reports back Value at channel 6 is: 346
for (int i = 0; i < 9; i++) {
  fsrReading = readMux(i, SIG_pin);
  fsrVoltage = map(fsrReading, 0, 1023, 0, 5000);
  if (fsrVoltage == 0) {
    Serial.print("00.00;");
  }
  else {
    fsrResistance = 5000 - fsrVoltage; // fsrVoltage is in mV, 5.5V = 5000mV
    fsrResistance *= 10000; // 10K resistor
    fsrResistance /= fsrVoltage;
    fsrConductance = 1000000; // we measure in micromhos so
    fsrConductance /= fsrResistance;
    Serial.print(fsrConductance);
    Serial.print(";");
  }
}
}

//END Reading Mat Sensors -----
// Read pressures
P0 = analogRead(A2);
P1 = analogRead(A3);
P2 = analogRead(A4);
Serial.print(P0);
Serial.print(';');
Serial.print(P1);
Serial.print(';');
Serial.print(P2);
Serial.print(';');
Serial.println("LF");
if (Serial.available() > 0) {
  // read the incoming byte:
  incoming[0] = Serial.read();
  incoming[1] = Serial.read();
  if (incoming[0] == '0' && incoming[1] == '0') {
    digitalWrite(11, LOW);
    digitalWrite(12, LOW);
  }
  else if ((incoming[0] == '0' && incoming[1] == '1') | (incoming[0] == '1' && incoming[1] == '0')) {
    digitalWrite(11, HIGH);
    digitalWrite(12, LOW);
  }
  else if (incoming[0] == '1' && incoming[1] == '1') {
    digitalWrite(11, HIGH);
    digitalWrite(12, HIGH);
  }
}
}

// Function => Loop the 16 to 1 MUX
int readMux(int channel, int SIG_pin) {
  int controlPin[] = {s0, s1, s2, s3};
  int muxChannel[9][4] = {
    {0, 0, 0, 0}, //channel 0
    {1, 0, 0, 0}, //channel 1

```

```

{0, 1, 0, 0}, //channel 2
{1, 1, 0, 0}, //channel 3
{0, 0, 1, 0}, //channel 4
{1, 0, 1, 0}, //channel 5
{0, 1, 1, 0}, //channel 6
{1, 1, 1, 0}, //channel 7
{0, 0, 0, 1}, //channel 8
};

//loop through the 4 sig
for (int i = 0; i < 4; i++) {
    digitalWrite(controlPin[i], muxChannel[channel][i]);
}
//read the value at the SIG pin
int val = analogRead(SIG_pin);
//return the value
return val;
}

```

MATLAB script to compute pref in control method.

```

%Gabriel Campos
%Dec 2 2016
%This program computes the p_ref used for the set-point in the control
%system. The p_ref is related as shown in Ch 5.
p_atm=101325 %Pa
R_air=286.706 %J/(Kg*K)
p_min=0; %Pa
p_max=6000; %Pa
a=11/100; %m
b=2*a; %m
c_max=3/100;%m
V_min=0.0; %min volume
V_max=(4/3)*pi()*a*b*c_max %
M_air=29 %g/mol
T=273.15+25; %K

p_range=linspace((p_min+p_atm),(p_max+p_atm),600) %100 points between kpa
V_range=linspace(V_min,V_max,600) %600 points for consistency
m_range=p_range.*V_range*(M_air/R_air*T)
C=R_air*T/M_air;

plot3(p_range,V_range/C,(m_range./p_range))
xlabel('p_ref (Pa)')
ylabel('Volume/((R_air T)/ M_air) Ratio')
zlabel('m/p Ratio')
title('P_ref Set-Point Computation');

```

B. Calibration, Normalization and Sensor Response

1. FSR sensor

Normalization readings were taken from all sensors under similar conditions such as the same material interface, temperature and timing. The normalization produced was repeated 24 hours later to confirm the reliability of the values obtained. After the normalization was performed with three different loads at 4.45 Hz (BaudRate 19200), 5 readings (after settling transient) were averages for each sensor and the resultant value was used to compute the gain. The gains, N_i , are stored in the MATLAB script for processing. Table 2-1 shows the N gain values for all sensors for F1.

Table A-0-1: Normalization Gains for F1=1.57 [N]

F1=1.57 [N]															
Mat 1		Mat 2		Mat 3		Mat 4		Mat 5		Mat 6		Mat 7		Mat 8	
ID	N	ID	N	ID	N	S ID	N	ID	N	ID	N	ID	N	ID	N
1	0.31	10	0.98	19	0.51	28	0.81	37	1.40	46	1.56	55	1.19	64	0.91
2	0.53	11	1.18	20	0.42	29	0.81	38	1.22	47	1.52	56	1.40	65	1.13
3	0.50	12	1.13	21	0.53	30	0.89	39	1.28	48	1.25	57	1.75	66	1.51
4	0.25	13	1.00	22	0.44	31	0.66	40	0.98	49	1.30	58	1.21	67	1.39
5	0.60	14	1.04	23	0.54	32	0.79	41	1.55	50	1.46	59	1.47	68	0.99
6	0.66	15	0.89	24	0.43	33	0.86	42	1.14	51	1.27	60	1.40	69	0.79
7	0.42	16	0.89	25	0.43	34	0.91	43	1.35	52	1.64	61	1.16	70	1.52
8	0.49	17	0.89	26	0.58	35	1.13	44	1.38	53	1.39	62	1.27	71	1.28
9	0.38	18	0.54	27	0.50	36	0.81	45	1.09	54	1.37	63	1.61	72	1.14

The reference sensor used for the hyperelastic calibration (ID 0R) was statically calibrated and as seen in Fig Figure A-0-1 with zero y-intercept. The linear calibration equation is given by:

$$F_{s,0R} = 0.0183G \quad \text{Eq. 0-1}$$

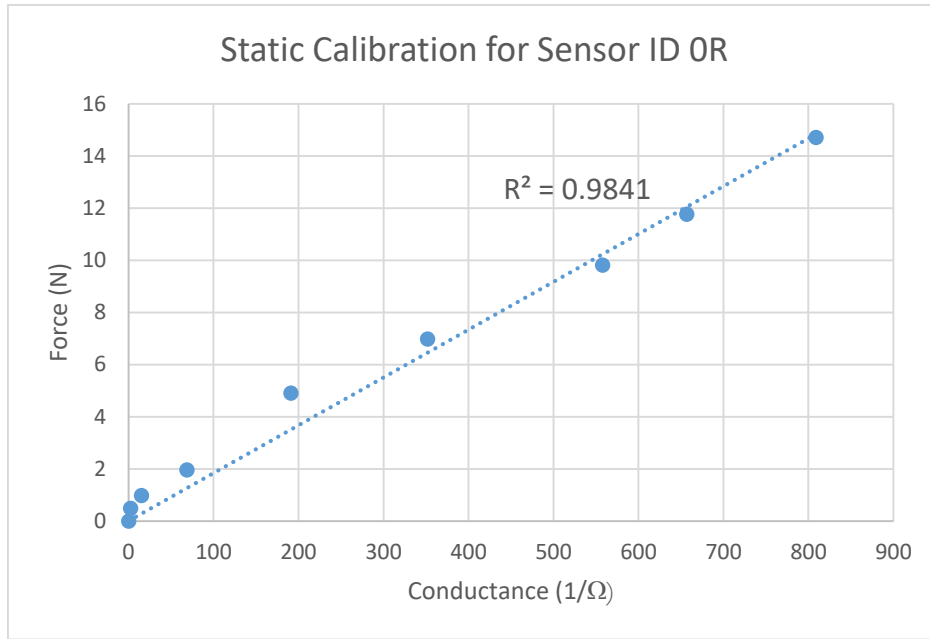


Figure A-0-1: Static calibration for sensor ID 0R.

2. Absolute, Integrated Pressure Sensor (MPXZ6130A)

The AAP sensor is a piezoresistive pressure transducer used to measure the atmospheric and air-springs internal gauge pressure. It is integrated with bipolar op-amp circuitry and a thin resistor electrical network that provides a temperature and humidity compensated analog signal proportional to the port pressure (Figure A-0-2). The circuitry used for the air-spring valve system used the AAP sensor with decoupling capacitors to suppress high-frequency noise in the power supply signal (Figure A-0-3).

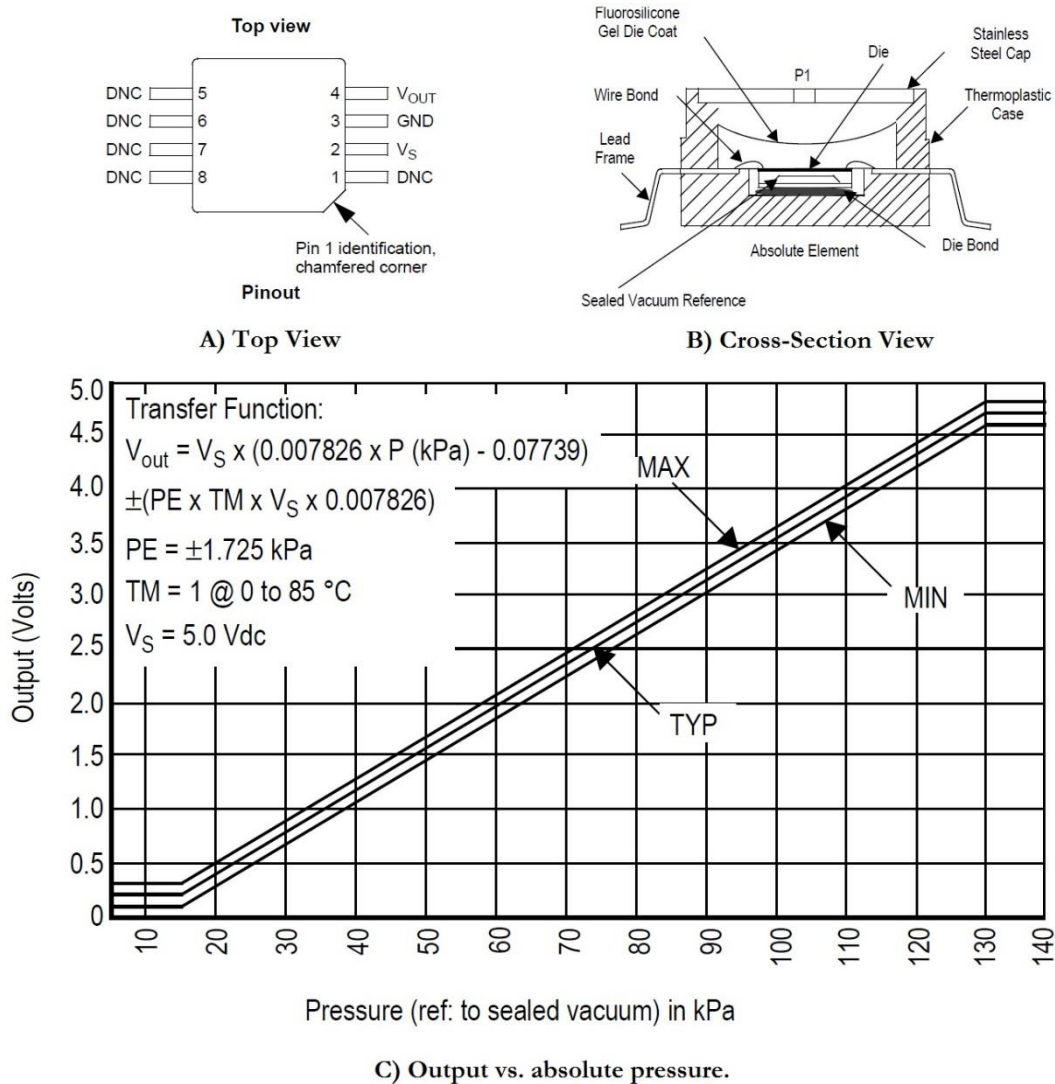


Figure A-0-2: MPXHZ6130A sensor A)Top view, B)Cross-section view C) Signal output [60].

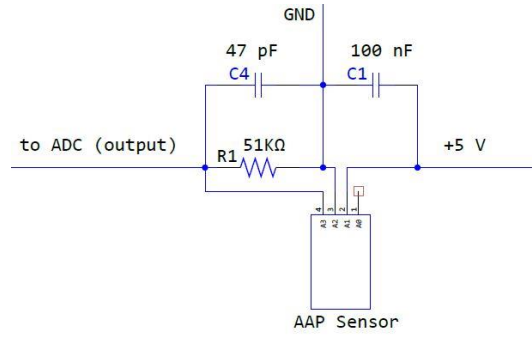


Figure A-0-3: AAP sensor decoupling circuitry.

C. Mooney-Rivlin Hyperelastic Model

The strain-energy function of the Mooney-Rivlin (1940), a model proposed prior to the Ogden model that can be used to describe hyperelastic mechanical properties of materials in terms of the strain-energy function, namely

$$\Psi = C_{10}(I_1 - 3) + C_{01}(I_2 - 3) \quad \text{Eq. A-0-2}$$

where μ is the shear modulus in the ground state, C_{10} and C_{01} are constants and which is linear in the invariants I_1 and I_2 , defined as

$$I_1 = \lambda_1^2 + \lambda_2^2 + \lambda_3^2 \text{ and } I_2 = \lambda_1^{-2} + \lambda_2^{-2} + \lambda_3^{-2} \quad \text{Eq. 0-3}$$

The Mooney-Rivlin is the most general form of strain-energy form function, which highlights the linearity between stress and strain in term of shear [37].

D. Figures of Interest

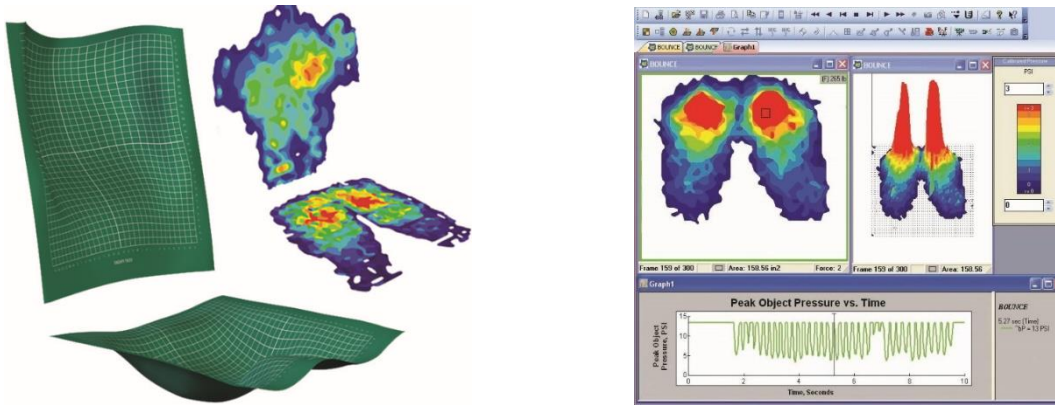


Figure A-0-4: Tekscan® (BPMS) Body Pressure Measurement System [61].

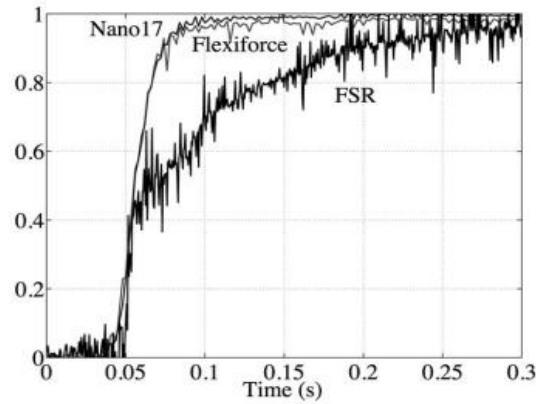


Figure A-0-5: Step responses of the Nano17, FSR, and FlexiForce sensors. [36].

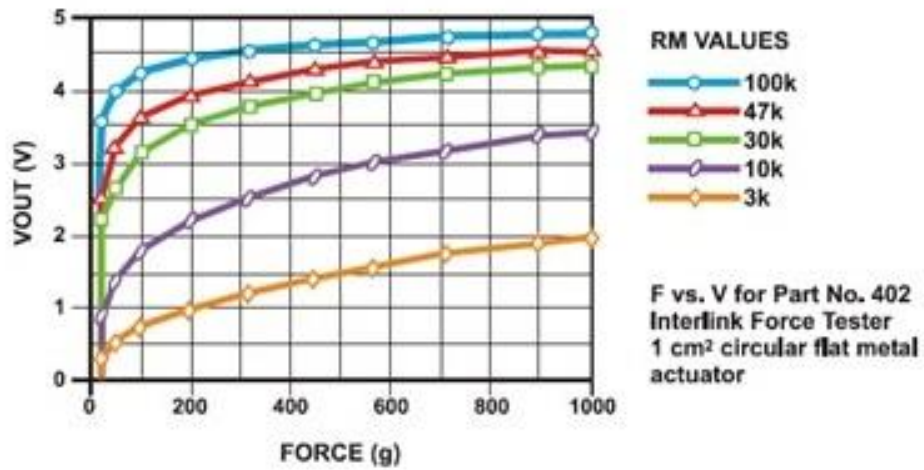


Figure A-0-6: FSR sensor output response for different R_M values [26].

Table A-0-2: Static Properties of the FlexiForce and FSR Sensors [36].

	Error of Linearity	Hysteresis	Repeatability	Time Drift
FlexiForce	5 %	10 %	3.6 %	6 %
FSR	7 %	8 %	2.1 %	4 %

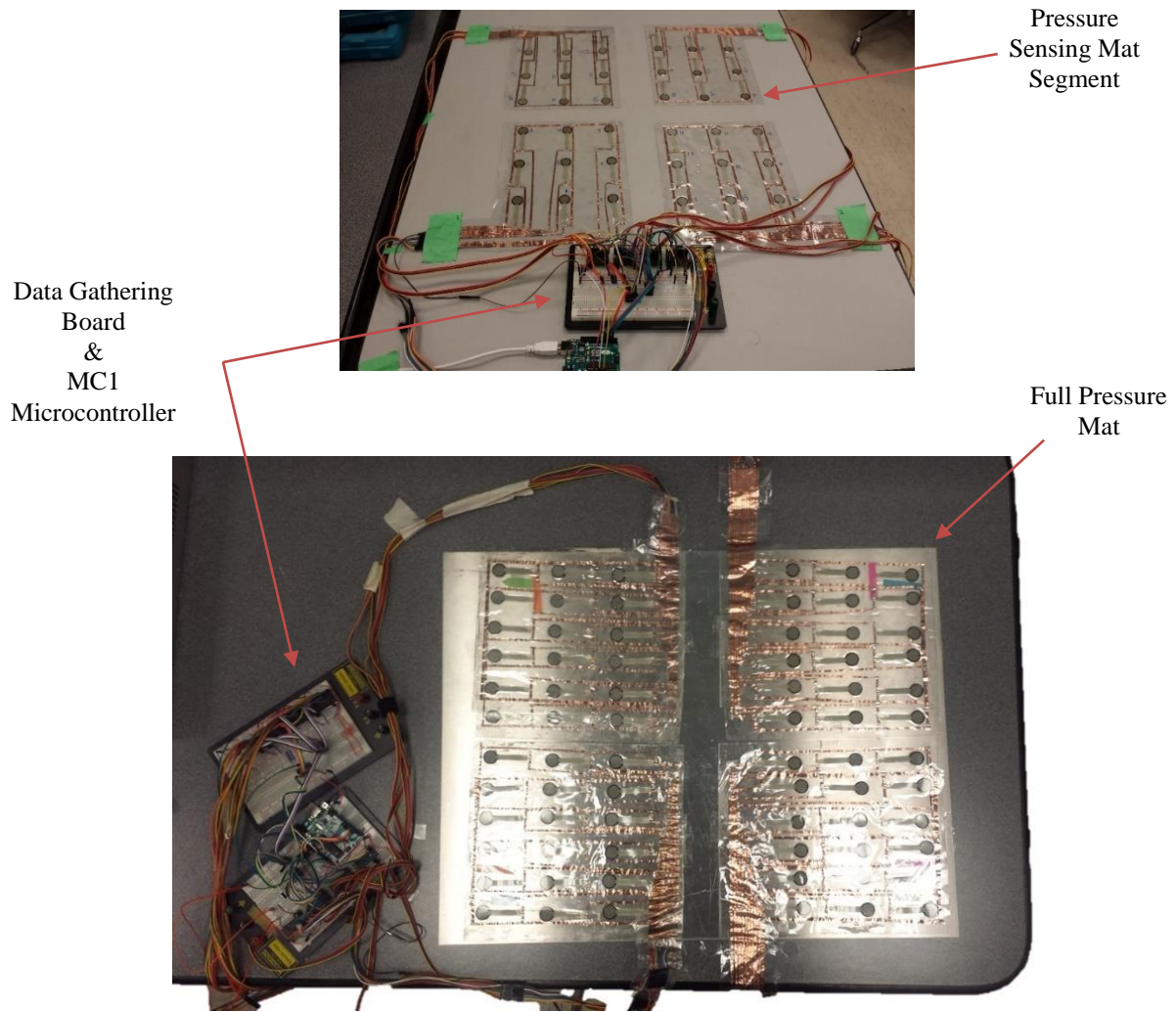


Figure A-0-7: Pressure mat and hardware

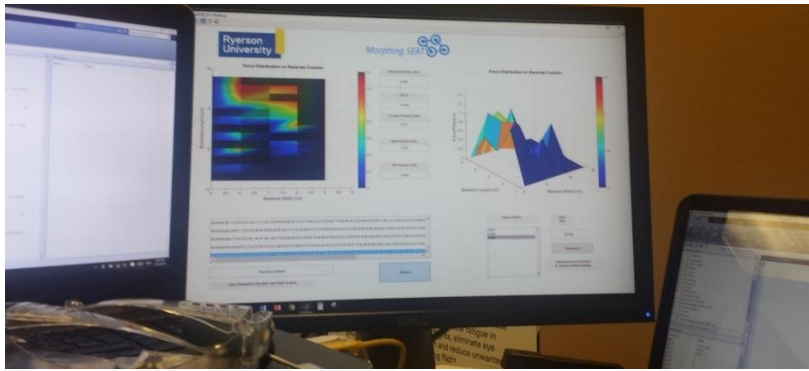


Figure A-0-8: Early version of the GUI

E. Overview of Surface Force/Pressure Sensing Theory

1. Capacitive Pressure Imaging Sensors:

The fundamentals of the capacitive pressure sensor found in the XSENSOR system consist of two parallel grids bonded to each other by an elastomer layer. The conductive strip layers are positioned at 45 degrees of each other, and each intersection between them creates what is known as a capacitance node element (Figure A-0-9). The capacitance of each node is proportional to the surface area and the thickness of the elastomer that separates the strips. The sensor's active layers are protected by insulating cover, which itself makes the final thickness of the pad 1 mm thick. As pressure is applied to the surface of the sensor, the elastomer is compressed, changing its surface area and thickness resulting in an increase in capacitance. Data from each node is collected via multiplexing circuitry. The detected analogue signal from the elements is then pre-processed, and sampled by a 16 bit analogue to digital converter. The digital data can be further processed and digitally filtered in order to reduce noise and calculate the capacitance values. The capacitance can be sampled at different rates to adjust accuracy (but increasing time for data acquisition) [23]. The complete setup for the XSENSOR is shown below in figure 19:

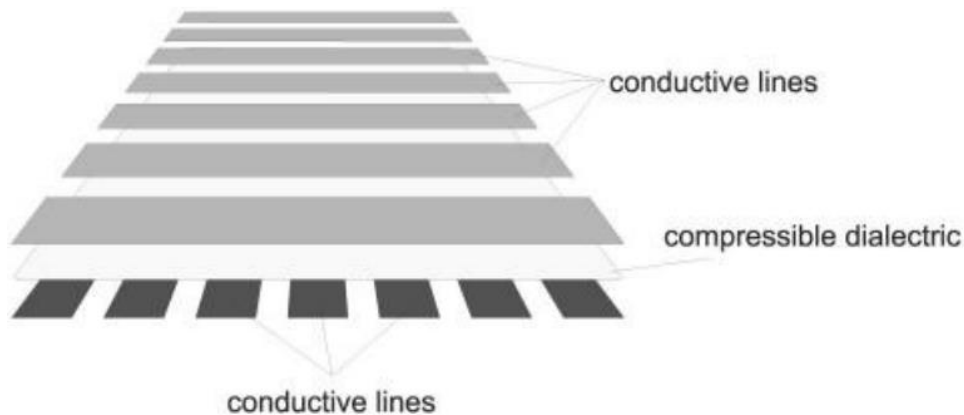


Figure A-0-9: Schematic of capacitive sensor [23].

2. Piezoresistive Force/Pressure Sensors:

The principle of piezoresistive sensing is the response of a material, often doped silicon or single-crystal silicon, to mechanical strain. Such response can be engineered to alter the electrical response in resistors. This effect provides a convenient and direct transduction mechanism to measure mechanical strain and deformation of thin foil sensors in the electrical domain (often via analogue signal) [50]. Generally, FSR's consist of two substrate layers of film which are laminated together with a spacer adhesive layer. One of the substrate layers is coated with conductive electrodes, while the opposite layer contains the invaded semiconductors as shown in Figure A-0-10 The thickness of the spacer layer is a key factor to determine the range of operational load of the sensor. At zero load, the spacer layer maintains an open circuit until a force is applied which forces the substrate layer together. As the applied force increases, there is an increased shunting of the conductive layer and as result the overall resistance of the FSR declines [34]. However, as Figure A-0-11 shows, there FSR sensors demonstrate saturation point where an increase in force results in non to just a small decrease in resistance. This saturation point is more a function of pressure (> 689 kPa) on the polymer more than a function of force (>10 kg) [26].

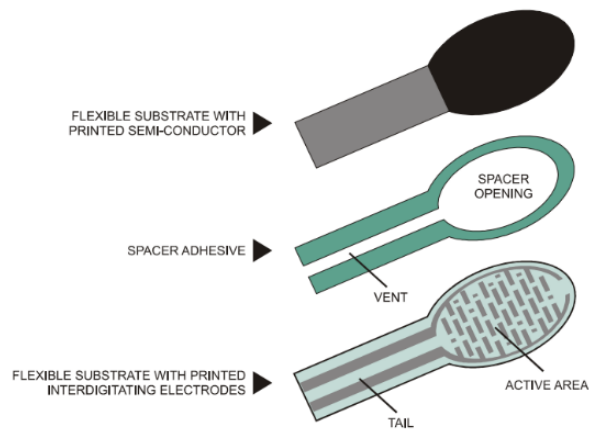


Figure A-0-10: FSR® Construction by Interlink Electronics [26].

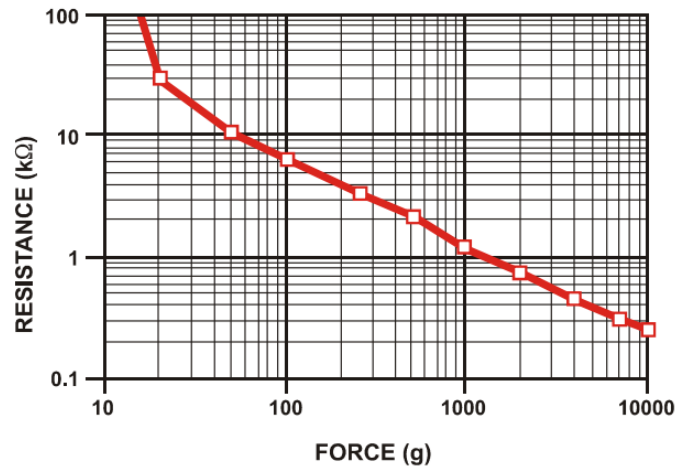


Figure A-0-11: Response characteristic of FSR® [26].

F. Raw Data and Calculations

Calculation in excel for area percentage of the backrest

Table A-0-3: Total Backrest Area

Total	Lt1 (cm)	Lw1 (cm)	A (cm ²)
	29	59	1711
	Lt2 (cm)	Lw2 (cm)	A (cm ²)
	24	49	1176
Total backrest area			2887

Table A-0-4: Percentage are per region in the backrest

Region	l (cm)	w (cm)	A (cm ²)	A%
1	9	41	369	12.78
2	42	6	252	8.73
3	42	6	252	8.73
4	21	34	714	24.73
5	21	34	714	24.73
Area without sensors				20.30

Calculations in excel of the mass and weight per body segment

Table A-0-5: Mass of Body Segments for the American Male [45].

Seg #	Segment	5th Percentile (gm)	50th Percentile (gm)	95th Percentile (gm)
1	Head	4260	440	4550
2	Neck	930	1100	1270
3	Thorax	20420	26110	31760
4	Abdomen	2030	2500	2960
5	Pelvis	9420	12300	15150
6	Upper arm	1600	2500	2500
7	Forearm	1180	1450	1720
8	Hand	460	530	610
9	Hip flap	2890	3640	4380
10	Thigh minus flap	5480	6700	7920
11	Calf	3320	4040	4760
12	Foot	840	1010	1180
Total		52830	62320	78760
5+4+3	Torso	31870	40910	49870
9+10	Thigh	8360	10340	12300
7+8	Forearm plus hand	1640	1980	2320
Total		41870	53230	64490

Table A-0-6: Weight force per body segment

Body part	Segments #	Mass of segment (gm)	Weight (N)	% body weight
Upper back	3+6+6+2+1	42580	417.71	41.81%
Lumbar	4+5+7+7+8+8	22770	223.37	22.36%
Tight	10+10+9+9	24600	241.33	24.16%
Leg	11+11+12+12	11880	116.54	11.67%
Total		101830	998.95	1

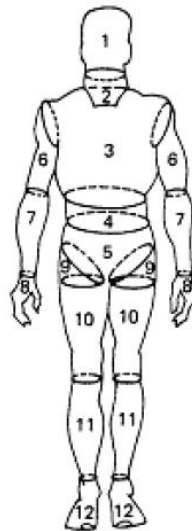


Figure A-0-12: Body segments [45].

Table A-0-7: Compression Test Results.

Compression Test Results for Foam-Ballistic Gel				
Force [N]	l (mm)	l0 (mm)	Strain (mm/mm)	Stress (kPa)
0	0	140.32	0	0
0.148779	1	140.32	0.007126568	0.377611675
0.280173	3	140.32	0.021379704	0.711098985
0.297009	3	140.32	0.021379704	0.753829949
0.343857	4	140.32	0.028506271	0.872733503
0.362157	4	140.32	0.028506271	0.919180203
0.395646	5	140.32	0.035632839	1.004177665
0.401136	5	140.32	0.035632839	1.018111675
0.411567	5	140.32	0.035632839	1.044586294
0.53619	6	140.32	0.042759407	1.360888325

0.563457	6	140.32	0.042759407	1.430093909
0.548451	6	140.32	0.042759407	1.392007614
0.557784	7	140.32	0.049885975	1.415695431
0.569679	7	140.32	0.049885975	1.445885787
0.67893	7	140.32	0.049885975	1.723172589
0.716628	8	140.32	0.057012543	1.818852792
0.799344	9	140.32	0.064139111	2.028791878
0.843813	9	140.32	0.064139111	2.14165736
0.882792	9	140.32	0.064139111	2.240588832
0.968253	10	140.32	0.071265678	2.457494924
1.001925	10	140.32	0.071265678	2.542956853
1.058289	11	140.32	0.078392246	2.68601269
1.117764	11	140.32	0.078392246	2.836964467
1.268556	12	140.32	0.085518814	3.219685279
1.310097	12	140.32	0.085518814	3.325119289
1.295091	12	140.32	0.085518814	3.287032995
1.284294	12	140.32	0.085518814	3.259629442
1.320894	13	140.32	0.092645382	3.352522843
1.448445	13	140.32	0.092645382	3.676256345
1.604727	14	140.32	0.09977195	4.072911168
1.728984	15	140.32	0.106898518	4.388284264
1.811151	15	140.32	0.106898518	4.596829949
1.86843	15	140.32	0.106898518	4.742208122
1.898625	15	140.32	0.106898518	4.818845178
1.860927	15	140.32	0.106898518	4.723164975
1.898625	16	140.32	0.114025086	4.818845178
1.913814	16	140.32	0.114025086	4.857395939
1.927722	16	140.32	0.114025086	4.892695431
1.890939	16	140.32	0.114025086	4.799337563
1.906128	16	140.32	0.114025086	4.837888325
1.943277	16	140.32	0.114025086	4.932175127
1.950963	16	140.32	0.114025086	4.951682741
1.97457	16	140.32	0.114025086	5.011598985
2.004948	16	140.32	0.114025086	5.088700508
2.045391	16	140.32	0.114025086	5.191347716
2.068632	16	140.32	0.114025086	5.250335025
2.110539	17	140.32	0.121151653	5.35669797
2.151714	17	140.32	0.121151653	5.461203046
2.110539	17	140.32	0.121151653	5.35669797
2.085285	17	140.32	0.121151653	5.292601523
2.160315	17	140.32	0.121151653	5.483032995
2.319708	17	140.32	0.121151653	5.887583756
2.471781	18	140.32	0.128278221	6.273555838
2.615985	18	140.32	0.128278221	6.639555838
2.701995	18	140.32	0.128278221	6.85785533
2.872002	19	140.32	0.135404789	7.289345178
2.847846	19	140.32	0.135404789	7.228035533
3.057747	19	140.32	0.135404789	7.760779188
3.368847	20	140.32	0.142531357	8.550373096
3.610041	21	140.32	0.149657925	9.162540609
3.773094	21	140.32	0.149657925	9.576380711
3.874476	21	140.32	0.149657925	9.833695431
3.946578	21	140.32	0.149657925	10.01669543
4.054182	22	140.32	0.156784493	10.28980203
4.130859	22	140.32	0.156784493	10.48441371
4.265913	22	140.32	0.156784493	10.82719036

4.471605	22	140.32	0.156784493	11.34925127
4.555236	22	140.32	0.156784493	11.56151269
4.668513	23	140.32	0.16391106	11.84901777
4.738602	23	140.32	0.16391106	12.02690863
4.878231	23	140.32	0.16391106	12.38129695
4.952712	23	140.32	0.16391106	12.57033503
5.023899	23	140.32	0.16391106	12.75101269
5.075688	23	140.32	0.16391106	12.88245685
5.25759	23	140.32	0.16391106	13.34413706
5.369037	24	140.32	0.171037628	13.62699746
5.478288	24	140.32	0.171037628	13.90428426
5.537214	24	140.32	0.171037628	14.05384264
5.62725	24	140.32	0.171037628	14.28236041
5.657811	24	140.32	0.171037628	14.3599264
5.744553	24	140.32	0.171037628	14.58008376
5.904495	24	140.32	0.171037628	14.98602792
5.839713	24	140.32	0.171037628	14.8216066
5.997276	24	140.32	0.171037628	15.22151269
5.904495	24	140.32	0.171037628	14.98602792
5.937435	24	140.32	0.171037628	15.06963198
6.099024	24	140.32	0.171037628	15.47975635
6.339669	25	140.32	0.178164196	16.09053046
6.488265	25	140.32	0.178164196	16.46767766
6.564576	25	140.32	0.178164196	16.66136041
6.564576	25	140.32	0.178164196	16.66136041
6.595503	25	140.32	0.178164196	16.73985533
6.713355	25	140.32	0.178164196	17.03897208
6.793875	25	140.32	0.178164196	17.24333756
6.834684	25	140.32	0.178164196	17.34691371
6.951255	25	140.32	0.178164196	17.64277919
6.993528	25	140.32	0.178164196	17.75007107
7.123092	25	140.32	0.178164196	18.07891371
7.167012	25	140.32	0.178164196	18.19038579
7.256316	25	140.32	0.178164196	18.41704569
7.256316	25	140.32	0.178164196	18.41704569
7.3383	25	140.32	0.178164196	18.6251269
7.478295	26	140.32	0.185290764	18.98044416
7.478295	26	140.32	0.185290764	18.98044416
7.525875	26	140.32	0.185290764	19.10120558
7.671543	26	140.32	0.185290764	19.47092132
7.721136	26	140.32	0.185290764	19.59679188
7.761213	26	140.32	0.185290764	19.69851015
7.761213	26	140.32	0.185290764	19.69851015
7.811721	26	140.32	0.185290764	19.82670305
7.862778	26	140.32	0.185290764	19.95628934
7.862778	26	140.32	0.185290764	19.95628934
7.966539	26	140.32	0.185290764	20.21964213

Bibliography

- [1] P. Vink, I. Kamp, M. Blok, and P. Vink, "Aircraft interior comfort experience," Delft, 2007.
- [2] P. Vink and K. Brauder, *Aircraft Interior Comfort and Design*. Boca Raton: CRC Press, 2011.
- [3] M. Helander and L. Zhang, "Field studies of comfort and discomfort in sitting," *Ergonomics*, vol. 40, no. 9, pp. 895–915, Sep. 1997.
- [4] N. Ahmadpour, "Aircraft Passenger Comfort Experience - Subjective Variables and Links To Emotional Responses," ÉCOLE POLYTECHNIQUE DE MONTRÉAL, 2014.
- [5] U. Kilincsoy, A. Wagner, P. Vink, and H. Bubb, "Application of ideal pressure distribution in development process of automobile seats," *Work*, vol. 54, no. 4, pp. 895–904, 2016.
- [6] H. N. Kale and C. L. Dhamejani, "Design parameters of driver seat in an automobile," *Int. J. Res. Eng. Technol.*, vol. 4, no. 6, pp. 448–452, 2015.
- [7] J. Happian-Smith, *An introduction to modern vehicle design*. Jordan Hill: Butterworth-Heinemann, 2000.
- [8] J. Hu and M. Reed, "Development of a Methodology for Simulating Seat Back Interaction Using Realistic Body Contours," *SAE Int.*, vol. 6, no. 2, pp. 623–628, 2013.
- [9] R. Zenk, M. Franz, H. Bubb, and P. Vink, "Technical note: Spine loading in automotive seating," *Appl. Ergon.*, vol. 43, no. 2, pp. 290–295, 2012.
- [10] J. Hartung, "Objektivierung des statischen Sitzkomforts auf Fahrzeugsitzen durch die Kontaktkräfte zwischen Mensch und Sitz [Objectification of Static Seating Comfort on Vehicle Seats by Contact Forces Between Man and Seat]," Technischen Universität München [Technical University of Munich], 2006.
- [11] S. Adler, "The relation between long-term seating comfort and driver movement," University of Jena, 2007.
- [12] R. Zenk, "Objektivierung des Sitzkomforts und seine automatische Anpassung [Objectification of Seating Comfort and its Automatic Adjustment]," Technischen Universität München [Technical University of Munich], 2008.
- [13] C. Mergl, "Entwicklung eines Verfahrens zur Optimierung des Sitzkomforts auf Automobilsitzen [Development of a Method for Optimizing the Seating Comfort of Automotive Seats]," Technical University of Munich, 2006.
- [14] L. Zhang, M. G. Helander, and C. G. Drury, "Identifying Factors of Comfort and Discomfort in Sitting," *Hum. Factors J. Hum. Factors Ergon. Soc.*, vol. 38, no. 3, pp. 377–389, Sep. 1996.

- [15] R. Zenk, M. Franz, A. Durt, and R. Lein, "Method and Device For Adjusting A Seat," US 2010/0276973 A1, 2010.
- [16] V. Laurent, C. Then, and G. Silber, "Human Modeling and CAE Based Subjective Seat Comfort Score Correlation," *SAE Int. J. Commer. Veh.*, vol. 7, no. 1, pp. 295–304, 2014.
- [17] I. Mircheski, T. Kandikjan, and S. Sidorenko, "COMFORT ANALYSIS OF VEHICLE DRIVER ' S SEAT THROUGH SIMULATION OF THE SITTING PROCESS," *Teh. Vjesn.*, vol. 21, no. 2, pp. 291–298, 2014.
- [18] H. Chen, H. Y. Song, J. G. Zhang, and F. Wang, "Study on Influence of Back Angle on Human Body Pressure Distribution," *Adv. Mater. Res.*, vol. 655–657, pp. 2088–2092, 2013.
- [19] P. D. Wettenschwiler, R. Stämpfli, S. Lorenzetti, S. J. Ferguson, R. M. Rossi, and S. Annaheim, "How reliable are pressure measurements with Tekscan sensors on the body surface of human subjects wearing load carriage systems?," *Int. J. Ind. Ergon.*, vol. 49, pp. 60–67, Sep. 2015.
- [20] T. Bryant, R. Pelot, J. Pinter, J. Stevenson, C. Hall, and J. Day, "Research and development of an advanced personal load carriage system phases II and III. Section E: Parametric analysis of advanced personal load carriage systems," Kingston, ON, 1997.
- [21] P. Le, J. Rose, G. Knapik, and W. S. Marras, "Objective classification of vehicle seat discomfort," *Ergonomics*, vol. 57, no. 4, pp. 536–44, 2014.
- [22] M. F. I. of T. Z. Fassler, "Studies on Mechatronics Force Sensing Technologies," University in Zürich, Switzerland, 2010.
- [23] R. Cork, "XSENSOR technology: a pressure imaging overview," *Sens. Rev.*, vol. 27, no. 1, pp. 24–28, 2007.
- [24] Tekscan Inc., "Pressure Mapping, Force Measurement & Tactile Sensors," 2015. [Online]. Available: <https://www.tekscan.com/>. [Accessed: 25-Nov-2016].
- [25] "How do I calibrate my FlexiForce Sensor? | Tekscan." [Online]. Available: <https://www.tekscan.com/support/faqs/how-do-i-calibrate-my-flexiforce-sensor>. [Accessed: 25-Nov-2016].
- [26] InterlinkElectronics, "FSR® Integration Guide & Evaluation Parts Catalog with Suggested Electrical Interfaces," Camarillo, CA, 2010.
- [27] D. Cheng, S. Sun, Z. Yang, and M. Shao, "Seat surface design due to the analysis of body pressure test data," *2010 IEEE 11th Int. Conf. Comput. Ind. Des. Concept. Des. 1*, vol. 1, pp. 659–661, 2010.
- [28] M. Ahmadian, T. M. Seigler, D. Clapper, and A. Sprouse, "Alternative Test Methods for Long Term Dynamic Effects of Vehicle Seats," 2002, p. 11.
- [29] D. Looze, L. F. . Kuijt-Evers, and V. Dieen, "Sitting comfort and discomfort and the relationships

- with objective measures,” *Ergonomics*, vol. 46, pp. 985–997, 2003.
- [30] H. Kirkland-Walsh, O. Teleten, M. Wilson, and B. Raingruber, “Pressure Mapping Comparison of Four OR Surfaces,” *AORN J.*, vol. 102, no. 1, p. 61.e1-61.e9, 2015.
- [31] D. C. Ferencz, H. J. Chizeck, I. A. Orthosis, D. C. Ferenczl, Z. Jin, H. J. Chizeckf, and E. Boulevard, “Estimation of Center-of-Pressure During Gait Using an Instrumented Ankle-Foor Orthosis,” in *Proceedings of the 15th Annual International Conference of the IEEE Engineering in Medicine and Biology Societ*, 1993, pp. 981–982.
- [32] J. a. Flórez, a. Velásquez, J. A. Florez, and A. Velasquez, “Calibration of force sensing resistors (fsr) for static and dynamic applications,” *2010 IEEE ANDESCON Conf. Proceedings, ANDESCON 2010*, pp. 2–7, Sep. 2010.
- [33] T. R. Jensen, R. G. Radwin, and J. G. Webster, “A conductive polymer sensor for measuring external finger forces,” *J. Biomech.*, vol. 24, no. 9, pp. 851–858, Jan. 1991.
- [34] E. P. Zehr, R. B. Stein, T. Komiyama, and Z. Kenwell, “Linearization of force sensing resistors (FSR’s) for force measurement during gait,” in *Proceedings of 17th International Conference of the Engineering in Medicine and Biology Society*, 1995, vol. 2, pp. 1571–1572.
- [35] D. Krklješ, L. Nagy, and K. Babković, “Force-dependent contact area excitation of FSR force sensor utilizing dome-shaped rubber element,” *2012 28th Int. Conf. Microelectron. - Proceedings, MIEL 2012*, no. Miel, pp. 181–184, 2012.
- [36] C. Lebosse, P. Renaud, B. Bayle, and M. de Mathelin, “Modeling and Evaluation of Low-Cost Force Sensors,” *IEEE Trans. Robot.*, vol. 27, no. 4, pp. 815–822, Aug. 2011.
- [37] R. W. Ogden, “Large Deformation Isotropic Elasticity—On the Correlation of Theory and Experiment for Incompressible Rubberlike Solids,” *Rubber Chem. Technol.*, vol. 46, no. 2, pp. 398–416, 1973.
- [38] L. L. Gras, D. Mitton, P. Viot, and S. Laporte, “Modelling of human muscle behaviour with a hyper-elastic constitutive law,” *Comput. Methods Biomech. Biomed. Engin.*, vol. 13, no. s1, pp. 63–64, 2010.
- [39] S. Ishihara, K. Ishihara, and M. Nagamachi, “The Finate Element Analysis Of Pressure Inside The Body White Lying Down On Mattress,” in *RESNA Annual Conference*, 2013, pp. 1–4.
- [40] K. Venkatesh Raja and R. Malayalamurthi, “Assessment on assorted hyper-elastic material models applied for large deformation soft finger contact problems,” *Int. J. Mech. Mater. Des.*, vol. 7, no. 4, pp. 299–305, 2011.
- [41] M. L. Ju, S. Mezghani, H. Jmal, and R. Dupuis, “Parameter Estimation of a Hyperelastic Constitutive

- Model for the Description of Polyurethane Foam in Large Deformation,” *Cell. Polym.*, vol. 32, no. 1, 2013.
- [42] J. Smardzewski, I. Grbac, and S. Prekrat, “Nonlinear mechanics of hyper elastic polyurethane furniture foams,” *Drv. Ind.*, vol. 59, no. 1, pp. 23–28, 2008.
- [43] N. Kumar and A. Dasgupta, “On the contact problem of an inflated spherical hyperelastic membrane,” *Int. J. Non. Linear. Mech.*, vol. 57, pp. 130–139, 2013.
- [44] F. Pingqing and S. Xinping, “Design of automotive seat surface based on ergonomics,” *2009 Int. Conf. Meas. Technol. Mechatronics Autom. ICMTMA 2009*, vol. 3, pp. 51–54, 2009.
- [45] “Man-Systems Integration Standards. Vol 1. Sec 3,” 1995.
- [46] R. H. M. Goossens and C. J. Snijders, “Design criteria for the reduction of shear forces in beds and seats,” University of Jena, 1997.
- [47] Tony Leyland, “Composition and Mechanical Properties of Connective Tissue.” Simon Fraser University, Burnaby, British Columbia, p. 92, 2009.
- [48] C. Jackson, A. J. Emck, M. J. Hunston, and P. C. Jarvis, “Pressure measurements and comfort of foam safety cushions for confined seating,” *Aviat. Sp. Environ. Med.*, vol. 80, no. 6, pp. 565–569, 2009.
- [49] S. C. Chapra, *Applied numerical methods with MATLAB for engineers and scientists*. McGraw-Hill, 2012.
- [50] K. Praveen and H. Guhilot, “FPGA Implementation of contactless position sensor using FSR (Force sensing Resistor),” in *2013 International Conference on Communication and Signal Processing*, 2013, pp. 1027–1031.
- [51] J. M. Brimacombe, D. R. Wilson, A. J. Hodgson, K. C. T. Ho, and C. Anglin, “Effect of Calibration Method on Tekscan Sensor Accuracy,” *J. Biomech. Eng.*, vol. 131, no. 3, p. 34503, 2009.
- [52] N. C. Nicholas and J. R. Welsch, “Ballistic Gelatin Report,” Pennsylvania, 2004.
- [53] J. Breeze, N. Hunt, I. Gibb, G. James, A. Hepper, and J. Clasper, “Experimental penetration of fragment simulating projectiles into porcine tissues compared with simulants,” *J. Forensic Leg. Med.*, vol. 20, no. 4, pp. 296–299, 2013.
- [54] H. Tanaka and E. Kobayashi, “Education and research using experimental pigs in a medical school.,” *J. Artif. Organs*, vol. 9, no. 3, pp. 136–43, 2006.
- [55] M. Grujicic, B. Pandurangan, G. Arakere, W. C. Bell, T. He, and X. Xie, “Seat-cushion and soft-tissue material modeling and a finite element investigation of the seating comfort for passenger-vehicle occupants,” *Mater. Des.*, vol. 30, no. 10, pp. 4273–4285, 2009.

- [56] M. Saadeh, "Identification of a force-sensing resistor for tactile applications," *J. Intell. Mater. Syst. Struct.*, vol. 24, no. 7, pp. 813–827, 2013.
- [57] A. Kokorikou, P. Vink, I. C. de Pauw, and A. Braca, "Exploring the design of a lightweight, sustainable and comfortable aircraft seat," *Work*, vol. 54, no. 4, pp. 941–954, Sep. 2016.
- [58] Stable Micro Systems, "Texture: Measurements and Analyse Properties," *Measure Gel Strength*, 2016. [Online]. Available: <http://www.stablemicrosystems.com/frameset.htm?http://www.stablemicrosystems.com/MeasureGelStrength.htm>. [Accessed: 25-Nov-2016].
- [59] Tekscan Inc., "FlexiForce Standard Model HT201." Tekscan.com, South Boston, MA, pp. 1–2.
- [60] I. FreescaleSemiconductors, "MPXHZ6130A, 15 to 130 kPa, Absolute , Integrated Pressure Sensor," 2015.
- [61] "Body Pressure Measurement System," 2015. [Online]. Available: <https://www.tekscan.com/products-solutions/systems/body-pressure-measurement-system-bpms-research?tab=software>. [Accessed: 25-Nov-2016].

Glossary

Term	Definition
Active Area	The physical part of a sensor that responds to an external input that results in an electrical output (signal).
Adipose Tissue	Fat tissue in animals.
Air-Spring	Pneumatic lifting elements
Anaerobic	A process occurred in the absence of oxygen.
Anthropometry	The science of measurement and proportion of the human body.
Array	A group or matrix of sensor elements which can be activated individually.
Bloom	Is a test to measure the strength of gel. It is the force (in grams), necessary to depress by 4 mm the surface of gelatin gel with a standard 0.5” diameter cylinder probe. The Bloom values ranges from 30-300 Bloom [58].
Break Force	The minimum limit of required force, for a specific actuator size, to cause the onset of the sensor.
Control point	The point where two polynomial splines meet. Also called a knot.
Coronal Plane	The imaginary plane that dives the body between front and back (YZ plane).
Dynamic Range	The ratio of largest to smallest detectable mechanical input (force/pressure) that the sensor can detect.
Dynamic Seat Design Elements	A seat that incorporates active morphing characteristics to accommodate different loads.
Ground State	The quantity of simple sensing elements contained in an array that can be activated individually.
Hypoxia	Initial geometry of the hyperelastic material. Such state is taken as the unloaded frame.
Hysteresis	Deficiency of oxygen in the tissue.
Ill-conditioned	In a dynamic measurement, the difference between instantaneous force measurements at a given force for an increasing load compared to the decreasing load.
In vitro	The condition number of a function is the measurement of how sensitive it is to round off error. Instability or erroneous solutions are encountered when the condition-number of the function is too large. Such functions with large condition number lead to numerical errors and are said to be ill-conditioned. Higher-order polynomials tend to be very ill-conditioned.
In vivo	Performed outside a living organism.
	Performed on a living organism.

Ischemia	Ischemia is the result of inadequate blood flow to the tissue when the pressure inside the tissue exceeds the opening pressure of the capillaries in that region. Closure of the capillaries causes pain due to accumulation of metabolites, mainly lactic acid which is a byproduct of anaerobic metabolism
Linearity Error	The maximum error of the true response of the best fit straight line (BFSL).
Nearest Neighbour Interpolation	A simple mathematical algorithm used to approximate unknown values in a function to closest adjacent point.
Over Force	The maximum force which is safe to apply to the sensor and still remain functional.
Range	The range of mechanical input (force/pressure) which the sensor is dimensioned for.
Repeatability	The tendency of a sensor to repeat (within a defined tolerance) a previous response characteristic.
Resolution	The distance between the sensing elements in an array sensor.
Response Characteristic	The relationship between the force/pressure vs. resistance of a sensor.
Sagittal Plane	In anatomy, the sagittal plane is the plane that divided the human body symmetrically into left and right. Since this plane transverses the human body through its centre, the forward and backward equations of motions of the human body can easily be represented graphically in a 2D free-body diagram.
Saturation Pressure	The maximum load at which beyond such level, the response characteristic deviates from its physical law describing the sensor's behaviour. At such point, an increase in input does not result (or small) in an electrical output.
Sensitivity	The ratio of output (signal) change to input (force) change (over force = span/operational force range).
Span	The mathematical difference between outputs (signal) measured at the upper and lower limits of the operational (force) range.
Static Seat Design	A rigid design of a seat, where geometry changes of the seat's surfaces are not possible.
Substrate	The base material on which the film sensors' semi-conductor or metallic polymer are adhered.

